ΠΑΝΕΠΙΣΤΗΜΙΟ ΚΡΗΤΗΣ
ΣΧΟΛΗ ΘΕΤΙΚΩΝ ΚΑΙ ΤΕΧΝΟΛΟΓΙΚΩΝ ΕΠΙΣΤΗΜΩΝ
ΤΜΗΜΑ ΕΠΙΣΤΗΜΗΣ ΚΑΙ ΤΕΧΝΟΛΟΓΙΑΣ ΥΛΙΚΩΝ

ΔΙΔΑΚΤΟΡΙΚΗ ΔΙΑΤΡΙΒΗ

# ΜΕΛΕΤΗ ΠΛΕΓΜΑΤΩΝ ΑΜΟΡΦΟΥ ΚΑΙ ΝΑΝΟΔΟΜΙΚΟΥ ΑΝΘΡΑΚΑ ΜΕ ΤΗ ΜΕΘΟΔΟ ΤΗΣ ΙΣΧΥΡΑΣ ΔΕΣΜΕΥΣΗΣ

ΜΑΘΙΟΥΔΑΚΗΣ ΧΡΗΣΤΟΣ

ΗΡΑΚΛΕΙΟ
2008

Christos Mathioudakis

# Tight - Binding Molecular Dynamics Studies Of Amorphous and Nanostructured Carbon Networks

A Doctoral Dissertation


Department of Materials Science and Technology,
University of Crete,
Heraklion, Greece
2008

*Christos Mathioudakis*

# *Tight - Binding Molecular Dynamics Studies of Amorphous and Nanostructured Carbon Networks*

*A Dissertation submitted to the Department of Materials Science and Technology, University of Crete in partial fulfillment of the requirements for the Degree of Doctor of Philosophy in Materials Science*

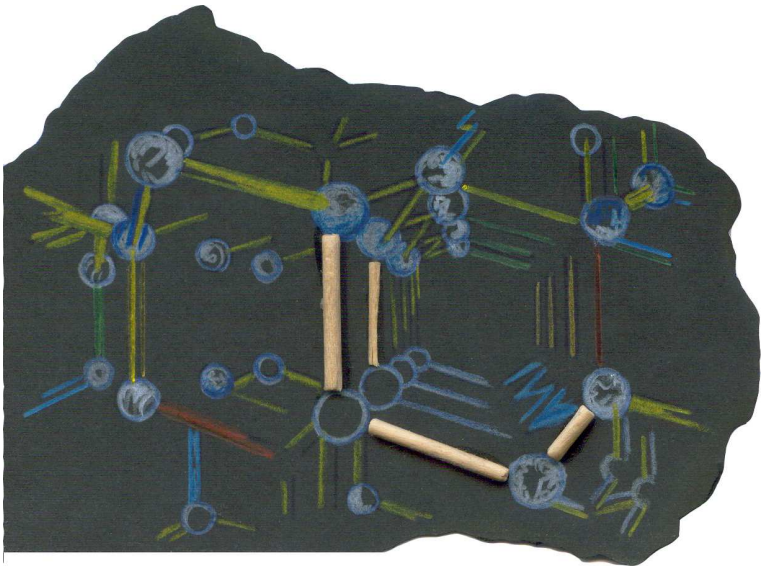

Heraklion, Greece, 2008

# Tight - Binding Molecular Dynamics Studies of Amorphous and Nanostructured Carbon Networks


| | |
|---|---|
| Thesis author | Christos Mathioudakis |
| Thesis supervisors | Assist. Prof. George Kopidakis<br>Prof. Pantelis C. Kelires |
| Thesis committee | G. Kopidakis<br>P. C. Kelires<br>C. M. Soukoulis<br>G. Fytas<br>N. T. Pelekanos<br>P. G. Savvidis<br>N. Flytzanis |

Department of Materials Science and Technology,
University of Crete,
Heraklion, Greece


2008

# Thesis Abstract

The purpose of this dissertation is to study and understand the structural, mechanical and optoelectronic properties of amorphous and nanostructured carbon. To achieve this goal, we carry out molecular dynamics simulations within the tight-binding (or linear combination of atomic orbitals) approximation. Highlights of the work done are the detailed study and analysis of the microstructure, the finding of general physical trends in the variation of basic characteristics, and the development of a methodology for the calculation and analysis of the optical properties.

As an introduction to the subject, we first present the elemental properties of carbon, its electronic structure and hybridizations, and the various forms that can be attained by carbon either in the solid state or in nanostructured configurations. Next, we present the theory of the tight-binding method and the two specific models used in this work. We also present the methodology for the computer generation of our networks, as well as the tools used for their analysis.

Initially, we study the microstructure of amorphous carbon. We extract the structural parameters of our networks and calculate the distribution functions of bond lengths and bond angles, and perform a statistical analysis of rings. We find that the basic characteristics of the microstructure are in excellent agreement with results from first-principle calculations.

After establishing the reliability of our methodology, we study the structural and elastic properties of our amorphous carbon networks. The main finding about the material density is that it has a linear dependence on the $sp^3$ tetrahedral fraction, in good agreement with experimental work and other theoretical calculations. Also, we extract for the first time accurate relations between the bulk modulus and the mean coordination (or equivalently the density) and the mean bond length in the amorphous network. These relations, in a power-law form, are in excellent agreement with mean-field theories for the elastic properties.

We continue by investigating the electronic and optical properties of amorphous carbon. Our major contribution here is the development of a methodology to calculate the optical constants from the tight-binding wavefunctions. Initially, we calculate the electronic density of states and the dielectric function, and we then extract the optical gaps and the Urbach energy, associating them with the degree of disorder in our networks. We compare to the literature where it is feasible.

Finally, the dissertation is concluded by applying the above well-tested methods to the case of nanostructured carbon.

# **Thesis Abstract** (in greek)

Ο σκοπός της παρούσας διατριβής είναι η μελέτη και κατανόηση των δομικών, μηχανικών και οπτοηλεκτρονικών ιδιοτήτων του αμόρφου και νανοδομικού άνθρακα. Για το σκοπό αυτό χρησιμοποιούμε προσομοιώσεις μοριακής δυναμικής βασισμένες στη μέθοδο της ισχυράς δέσμευσης (ή γραμμικού συνδυασμού ατομικών τροχιακών). Κεντρικά σημεία της διατριβής είναι η λεπτομερής μελέτη της μικροδομής και η εύρεση γενικών τάσεων/σχέσεων για τις μεταβολές των χαρακτηριστικών ιδιοτήτων, καθώς και η ανάπτυξη μιας μεθοδολογίας για τον υπολογισμό των οπτικών ιδιοτήτων.

Κατ' αρχάς, παρουσιάζουμε εισαγωγικά τη φυσική δομή του άνθρακα, τις ιδιότητές του, την ηλεκτρονική διάταξη και τους υβριδισμούς των τροχιακών του, και τις διάφορες μορφές που μπορεί να πάρει ο άνθρακας είτε στη στερεά κατάσταση, ή σε νανοδομικές διαμορφώσεις, πράγμα που είναι απόρροια των παραπάνω. Στη συνέχεια εισάγουμε τη θεωρία της μεθόδου της ισχυράς δέσμευσης και παρουσιάζουμε τα δυο διαφορετικά μοντέλα που θα χρησιμοποιήσουμε. Επίσης συζητάμε τη μεθοδολογία που θα ακολουθήσουμε στην κατασκευή των πλεγμάτων μας, καθώς και τα "εργαλεία" που θα χρειαστούμε για την ανάλυση των ιδιοτήτων του υλικού μας.

Αρχικά μελετάμε τη μικροδομή του άμορφου άνθρακα. Εξάγουμε τις δομικές παραμέτρους των πλεγμάτων μας και υπολογίζουμε τις συναρτήσεις κατανομής των μηκών και των γωνιών μεταξύ των δεσμών των ατόμων. Εν συνεχεία κάνουμε μια στατιστική στους δακτυλίους που συναντάμε στο υλικό μας. Βρίσκουμε πως τα βασικά χαρακτηριστικά της μικροδομής είναι σε άριστη συμφωνία με αποτελέσματα από υπολογισμούς πρώτων αρχών.

Αφού διαπιστώσουμε την πλήρη αξιοπιστία της μεθοδολογίας, μελετάμε στην επόμενη φάση τις δομικές και τις ελαστικές ιδιότητες των πλεγμάτων μας. Το βασικό συμπέρασμα που προκύπτει για την πυκνότητα των δειγμάτων μας, είναι πως η τελευταία έχει γραμμική εξάρτηση με το ποσοστό των $sp^3$ ατόμων και το αποτέλεσμα αυτό συγκρίνεται με πειραματικά και άλλα θεωρητικά δεδομένα και αποκαλύπτεται συμφωνία μεταξύ τους. Επίσης, εξάγουμε για πρώτη φορά ακριβείς σχέσεις μεταξύ του μέτρου ελαστικότητας όγκου και του μέσου αριθμού συντάξεως (ή της πυκνότητας), και του μέσου μήκους δεσμού στο άμορφο πλέγμα. Οι σχέσεις αυτές, σε μορφή νόμου δυνάμεως, είναι σε εξαιρετική συμφωνία με θεωρίες μέσου πεδίου για τις ελαστικές ιδιότητες.

Στη συνέχεια μελετάμε τις ηλεκτρονικές και τις οπτικές ιδιότητες του υλικού μας. Η κύρια συνεισφορά μας εδώ είναι η ανάπτυξη μιας μεθοδολογίας για τον υπολογισμό των οπτικών σταθερών από τις κυματοσυναρτήσεις ισχυράς δέσμευσης. Κατ'αρχάς υπολογίζουμε την ηλεκτρονική πυκνότητα καταστάσεων και τη διηλεκτρική συνάρτηση, και καταλήγουμε στο οπτικό χάσμα και την ενέργεια Urbach και πως αυτά συνδέονται με την αταξία μέσα στα πλέγματα μας. Όλα τα αποτελέσματά μας συγκρίνονται με αντίστοιχα που συναντάμε στη βιβλιογραφία.

Τέλος η διατριβή ολοκληρώνεται με την εφαρμογή όλων των παραπάνω στην περίπτωση του νανοδομικού άνθρακα. Αφού πρώτα εδραιώσαμε μια ολοκληρωμένη μεθοδολογία υπολογισμού των ιδιοτήτων του άμορφου άνθρακα, αποφασίσαμε να την ελέγξουμε και στη νανοδομική μορφή του υλικού και εδώ παρουσιάζουμε τα συμπεράσματά μας.

# Acknowledgments

*First of all, I'd like to express my greatest debt to my supervisor Prof. P. C. Kelires who graciously accepted me as a post-graduate student. The breadth and depth of his expertise, along with his support, made this thesis come true.*

*I would also like to express my gratitude to my second supervisor Prof. G. Kopidakis whose assistance and advice were more than valuable for the completion of this task.*

*I feel I should also refer to my lovely wife Dora. Her love and support she provided me through these years, that we are together, was of immeasurable value to me.*

*I would also like to thank my colleagues and good friends Dr. G. C. Hadjisavvas and Dr. M. G. Fyta whose long discussions and support kept me going.*

*I must express my deep and sincere thanks to my colleague and best man too Dr. I. N. Remediakis, who believed in me and his advice as well as his suggestions were catalytic to this thesis.*

*Furthermore I want to offer special thanks to my friends who really stood by me throughout these years.*

*Finally I am especially indebted to my family who supported me at every step I've taken since the beginning of my life.*

# Contents

# Chapter 1

# Introduction

Despite the intense investigations over the last fifteen years, the properties of amorphous [1] carbon [2] (a-C) are not fully understood. Some of them are strongly debated. A lot of interest has been put to tetrahedral a-C (ta-C), containing a high fraction of $sp^3$ hybrids, because of its diamondlike properties [3, 4]. These include high hardness making it suitable for mechanical purposes, such as protective coatings, a wide band gap for optical applications, and biocompatibility for biomedical coatings. Ta-C has also promising applications in micro-electromechanical devices (MEMS). Ta-C has not been used so far as an electronic material because electron states in the $\pi$ orbitals, lying within the broader $\sigma - \sigma^*$ gap, are sufficiently localized to yield low conductivity.

Recently, nanostructured amorphous carbon (na-C) has attracted attention because it offers the unique possibility to intermingle the properties of carbon nanostructures with those of pure a-C [5, 6, 7]. It is a hybrid form of carbon in which carbon nanocrystallites are embedded in the a-C matrix [8]. These carbon nanostructures range, from diamond crystallites [9] to porous, open graphene structures with negative curvature (schwarzites) [10, 11, 12]. Cluster-assembled carbon films with amorphous $sp^2$ character and a sizeable carbyne ($sp^1$ chains) component have also been reported [13, 14]. Na-C is expected to tailor the mechanical and electronic properties of a-C.

Another very interesting carbon material widely studied is nanocrystalline diamond [15]. It is composed of randomly oriented nanodiamond grains, with grain boundaries, few Angstroms wide, serving as the interfacial geometries. It is believed that many atoms in the grain boundaries, how many yet unclear, are $sp^2$-bonded. Doping these interfaces with nitrogen seems to increase the conductivity of the material. These nanodiamond films are reported to be extremely hard, probably harder than ta-C, approaching the hardness of crystalline diamond.

Therefore, the range of promising new forms of carbon is extremely wide. The fundamental macroscopic quantity, used in order to distinguish among them is the *density*. This ranges from very low values, such as $\sim$ 0.5 - 1 gcm$^{-3}$ for carbon foams and schwarzites, to near diamond values $\simeq$ 2.8-3.2 gcm$^{-3}$ for ta-C. There might even exist huge gradients of density within the same material, as in na-C and nanodiamonds. A unified approach to the study of a-C can link all other characteristic quantities of the material to its density, over the whole range of possible configurations. Such quantities include the $sp^3$ fraction, the elastic moduli, the intrinsic stress, the structural correlations, the electronic density of states and the energy gap. The primary goal of this association is to unravel the fundamental trends behind the properties as the density varies, to predict new behaviors from existing data and to clarify certain issues which are debated, i.e., interpreted in a different way by different experimental and theoretical methods.

In view of the fast emerging field of carbon-based composite nanomaterials, characterized by inhomogeneous density profiles, where both high- and low-density regions co-exist, a global theoretical study covering the whole density region is highly desirable. The aim of such a theory is to establish simple relations describing the trends in the single-phase systems, which can be used in the more complex composite cases. For example, the structural and mechanical properties of numerous carbon based materials have been extensively modelled by Kelires [16, 17, 18, 19, 20, 21] employing the empirical Tersoff potential. However, it is desirable to move a step further in the study of these properties by employing more accurate energy functionals.

Another interesting research subject in the field of a-C is the study of its electronic structure and optical properties, which are related to the hybridization state. Thus, the optical properties are particularly interesting as they can provide accurate, although indirect determination of the chemical state of a-C ($sp^3/sp^2$ ratio), and they are essential for many applications where optical transparency is required, such as in protective coatings for lenses and optical systems [22]. The optical properties of a-C are dominated by the $\pi$ - $\pi^*$ and $\sigma$ - $\sigma^*$ electronic transitions, which show up as distinct features in the dielectric function spectra [23, 24, 25]. The $\pi$ - $\pi^*$ contribution originates exclusively from $sp^2$ carbon atoms and particularly from the transition of $\pi$-bonded electrons to $\pi^*$ antibonding states. On the other hand, the $\sigma$ - $\sigma^*$ transition comes from the $\sigma$-bonded electrons participating in the covalent bonds of both $sp^3$ and $sp^2$ carbon atoms [23, 24].

Despite the intensive investigations, the optoelectronic properties of a-C are not fully understood, and many issues, such as the variation of the optical gap and of other quantities as a function of the $sp^3$ fraction and the role of defects and disorder, remain unclear.

Finally, our interest on na-C is steadily growing for its properties, both mechanical and electronic, that will supplement those of the traditional, single phase a-C. Na-C can be described as a composite material in which carbon nanocrystallites, of various sizes and phases, are embedded in the a-C matrix. This interesting hybrid form of carbon offers the unique possibility to intermingle the properties of carbon nanostructures [26] with those of pure a-C [3, 4]. For example, since some of these nanostructures are proposed to be insulating, while others to be metallic, the possibility is opened for tailoring the electronic properties of a-C by controlling the type and size of the embedded structures.

To achieve the goal of a global description, we therefore need an accurate computational method able to address the fundamental issues at all densities and yield statistical precision. The method also has to be transferable and not too costly for the description of properties at the nanoscale. The use of *ab initio* methods is prohibitive for this purpose and we need more accuracy than that provided by empirical potentials. A very good candidate to tackle this problem would be the tight-binding approach. Such a computational method may be coupled to empirical potentials in problems where the latter can be safely used, to address large-scale problems in a multiscale approach.

Here, we present a detailed theoretical study of various fundamental properties of a-C through the whole range of possible densities, in the spirit described above.

# Chapter 2

# Carbon

*Carbon is encountered in various forms. As a crystal it can have either the structure of diamond or that of graphite. There are many modifications even at its amorphous phase. In the last years, other new forms of carbon have been discovered and attracted great attention. These include nanostructured and nanocomposite carbon, fullerenes, and nanotubes. The plethora of the various forms of carbon makes it an exciting field to study.*

## 2.1 General

Carbon is an exceptional element in its ability to form strong chemical bonds with a great variety of coordination numbers from two, to three and four. It is able to form one of the hardest materials or one of the softest. It could have a bandgap as great as 5.5 eV, being thus insulator, or it could have conductive configuration.

The element carbon has an atomic number of six. Its electron configuration, that is the arrangement of the electron in each orbital, is described as: $1s^2 2s^2 2p^2$. This means that it has two electrons in the $K$ shell ($1s^2$). The $K$ shell is filled, completely stable and its electrons do not take part in any bonding. The $K$-shell electrons have opposite spin. It also has four electrons in the $L$ shell ($2s^2 2p^2$). The $L$-shell electrons belong to different subshells, the $s$ and the $p$, in different energy levels. The two $2s$ electrons have opposite spin, in contrast to the two $2p$ electrons, which have parallel spin. The whole view of carbon's electronic structure is represented schematically in Fig. 2.1a.

In order to have an electron configuration, that would account for the tetrahedral symmetry found in structures such as diamond, the structure of carbon atom must be altered to a state with four valence electrons instead of two, each in a separate orbital

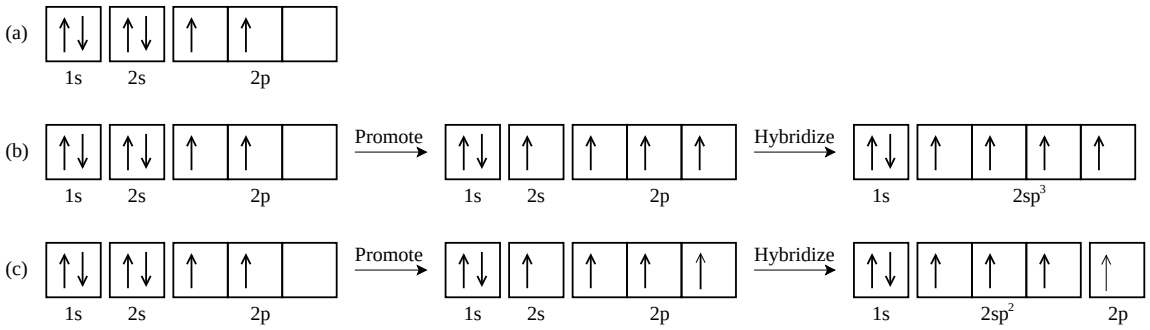


**Fig. 2.1**: Electronic configurations: (a) The electronic structure of the carbon in the ground state. (b) The $sp^3$ hybridization of carbon orbitals. (c) The $sp^2$ hybridization of carbon orbitals.

and each with its spin uncoupled from the other electrons. This alteration occurs as a result of the formation of hybrid atomic orbitals, in which the arrangement of the electrons of the $L$ shell of the atom in the ground state is modified as one of the $2s$ electrons is promoted to the higher orbital $2p$ as shown in Fig. 2.1b. These new orbitals are called hybrids since they combine the $2s$ and the $2p$ orbitals. They are labeled $sp^3$ since they are formed from one $s$ and three $p$ orbitals. Now, the carbon atom has four $2sp^3$ orbitals and the valence state is raised from two to four. A graphic visualization of the formation of the $sp^3$ hybridization is shown in Fig. 2.2a. The four hybrid $sp^3$ orbitals are tetrahedrally oriented around the atom (so the $sp^3$ orbital is known as the tetragonal orbital), have identical shape but different spatial orientation. They form a regular tetrahedron with equal angles to each other of $109°28'$. This configuration forms strong covalent $\sigma$ bonds.

In addition to the $sp^3$-tetragonal hybrid orbital above, two other orbitals complete the series of electronic building blocks of all carbon different species: the $sp^2$ and the $sp^1$ orbitals. The mechanism of the $sp^2$ hybridization is somewhat different from the $sp^3$ hybridization. The arrengement of the electrons of the $L$ shell of the atom in the ground state is modified as one of the $2s$ electrons is promoted and combined with two of the $2p$ orbitals, to form three $sp^2$ orbitals and an unhybridized free $p$ orbital electron as shown in Fig. 2.1c. The valence state has now four electrons. The three identical $sp^2$ orbitals are in the same plane and their orientation forms a $120°$ angle as shown in Fig. 2.2b. The $sp^2$ orbital (or trigonal orbital) is the key of all graphitic structures and aromatic compounds. This configuration results in in-plane strong covalent $\sigma$ bonds and weak $\pi$ bonds out of plane.

The $sp^1$ orbital (known as digonal orbital) is a compination of an $s$ and a $p$ orbital. An $sp^1$ bond consists of two $sp^1$ orbitals, which form an angle of $180°$ and

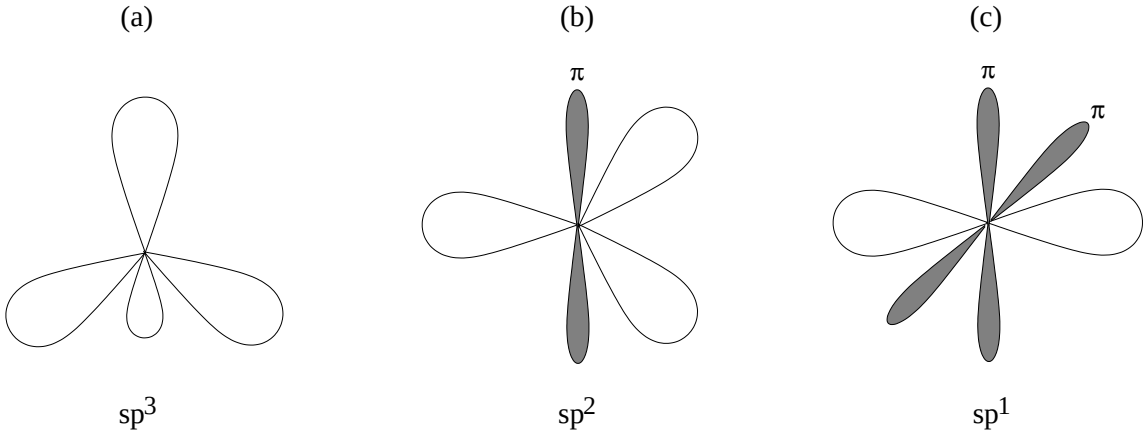


**Fig. 2.2**: Carbon's three hybridizations, $sp^3$, $sp^2$ and $sp^1$.

consequently the $sp^1$ molecule is linear. The $sp^1$ configuration forms linear $\sigma$ bonds and two $\pi$ bonds in vertical directions (Fig. 2.2c). An example of a molecule having $sp^1$ bonds is acetylene.

Many unique properties of condensed carbon phases come from the combination of strong bonds with light mass and high melting point. These properties make the material technologically important, as well as scientifically fascinating. Despite all the extensive studies over the past few decades, many intersting problems remain unresolved.

## 2.2 Allotropes of Carbon

The capability of an element to combine its atoms to form such allotropes is not unique to carbon. Other materials in the fourth column of the periodic table (silicon, germanium and tin) also have that characteristic. However carbon is unique in the number and the variety of its allotropes. The properties of the various carbon allotropes can vary widely. Yet these materials are made of the same carbon atoms; the disparity is the result of different arrangements of their atomic structure.

So our great interest in the several crystalline forms of carbon is based on their bond hybridization. In addition, each of these forms has a unique structure, that can produce properties similar to the ones that we can find at its amorphous counterparts. First of all, we have to refer to diamond with a coordination number (i.e. the average number of an atom's nearest neighbors, to which we'll refer later) of four and graphite with a coordination number which equals to three. Then there was

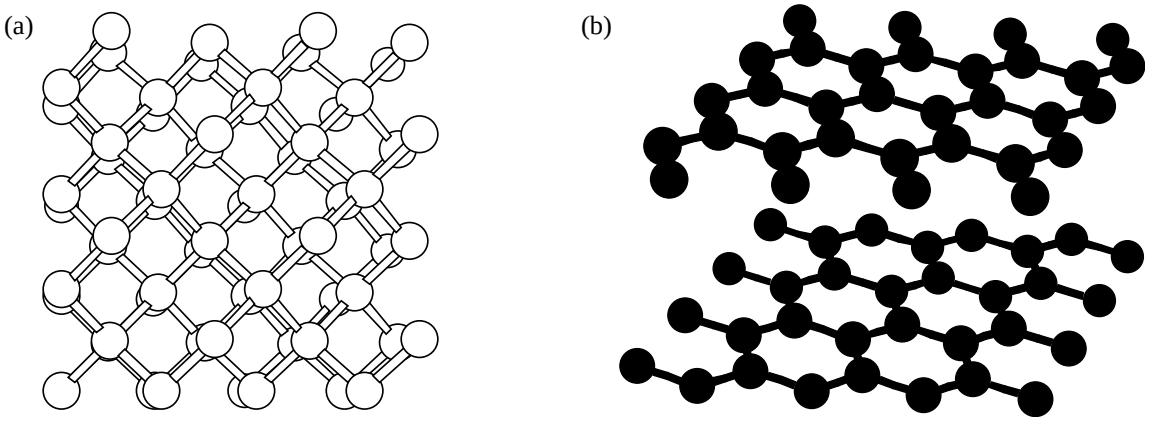


**Fig. 2.3**: Crystalline forms of carbon: (a) Diamond and (b) Graphite. Open and dark spheres denote $sp^3$ and $sp^2$ sites, respectively.

a attempt to introduce a third allotropic form of carbon called carbyne[1] [27, 28], which had a coordination number which equals to two. Furthermore buckminsterfullerene[2] [29, 30] or $C_{60}$ appears and its bond hybridization can be regarded as an $sp^{2.5}$ hybridization [31].

### 2.2.1 Diamond

Diamond (Fig. 2.3a) is the hardest substance known to man. It has the highest atom density, one of the largest known bulk moduli, extremely high strength and rigidity. It has the largest room temperature thermal conductivity of any solid and the smallest thermal expansion coefficient. It has a wide bandgap of 5.5 eV, five times common semiconductors' average hole mobility and a dielectric constant that is half of that of silicon. It has an unusually high index of refraction and it is transparent to the visible spectrum.

The structure of diamond is fully constructed by $sp^3$ hybrids. It requires a loss of energy but this effect is compensated by a very profitable covalent bonding. Quantum-mechanical calculations indicate that greater overlap between orbitals results in a stronger covalent bond, which is called $\sigma$ bond. This bond is the source of all these extreme physical properties of diamond. The diamond structure represents a three-dimensional network of strong covalent bonds (Fig. 2.3), which explains why diamond is so hard.

[1] Carbynes have a fully crystalline $sp^1$ bonded chainlike structure.

[2] Its unique structure consists of 60 carbon atoms formed into a large molecule which has a shape similar to that of a football ball.

The diamond structure is cubic with a cube edge length of $a_0$=3.567Å and can be viewed as two interpenetrating FCC structures, displaced by (1/4,1/4,1/4)$a_0$. The C-C distance of the single bond length is 1.54 Å. The diamond crystal is highly symmetric with a cubic space group $F4_1/d\ \bar{3}\ 2/m = Fd3m = O_h^7$.

Since all the valence electrons contribute to the covalent bond, they are not free to migrate through the crystal and thus, diamond is a poor conductor and has a wide bandgap.

### 2.2.2 Graphite

The origin of the word "graphite" is the greek word "$\gamma\rho\alpha\phi\epsilon\iota\nu$" (graphin), which means "to write", because of the use of graphite in pencils. Graphite (Fig. 2.3b) is a fully trigonal network of bonds that forms planar six-member aromatic rings of single and double bonded carbon. It is quite soft and opaque.

In the graphite structure, overlap occurs between the $2sp^2$ orbitals of neighboring atoms in the same plane, making $\sigma$-bonds. For such neighbors a side-to-side overlap also occurs between their unhybridized $p$ orbitals. A side-to-side bonding known as $\pi$-bonding results between these neighbors. The electrons participating in this $\pi$-bonding seem able to move across these $\pi$-bonds from one atom to the next.

This feature explains graphite's ability to conduct electricity along the sheets of carbon atom parallel to the (0001) direction. An in-plane nearest-neighbor distance is 1.42 Å. The adjacent sheets of carbon atoms are held together by the weak Van der Waals bonds and separated by a distance 3.54 Å. This gives softness to the structure.

A single graphite plane is a zero bandgap semiconductor and behaves as a metallic conductor in three dimensions.

The crystal structure is described by hexagonal lattice with $D_{6h}^4$ ($P6_3/mmc$) space group.

### 2.2.3 Amorphous Carbon

#### 2.2.3.1 General

Amorphous carbon (a-C) (Fig. 2.4) is the generic term used to describe most of disordered carbon films. Although there is no long range order present, both short and medium range order is preserved. This makes a-C to have physical properties similar to its crystalline counterpart. The examination of the nearest neighbor distance and the next nearest neighbor one shows that the short and medium range order is very close to clystalline material. In contrast to the previous, the bond angle

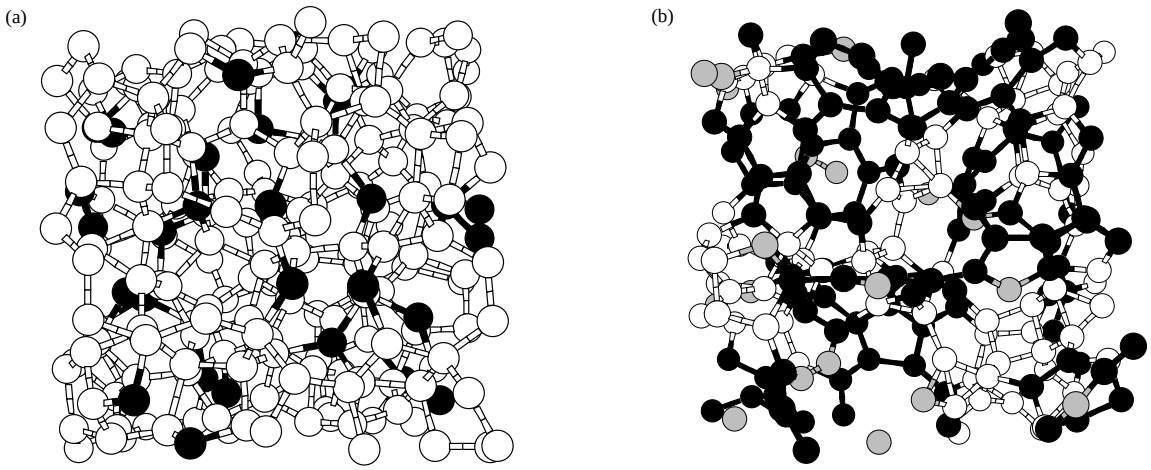


**Fig. 2.4**: Amorphous carbon networks: (a) ta-C, with a high percentage of $sp^3$ hybrids and (b) a-C, wih a balanced fraction of $sp^3$ and $sp^2$ hybrids. Open, dark and shaded spheres denote $sp^3$, $sp^2$ and $sp^1$ sites, respectively.

distribution is different from that of the crystalline case and doesn't give a-C long range order. But this angular variation can also give rise to the narrowing of the bandgap and the creation of highly localized states within the bandgap.

Figure 2.5 presents, schematically and in a nutshell, the salient characteristics of the atomic arrangements in glasses as opposed to crystals. Also included, as an additional and useful reference point, is a sketch of the arrangement in a gas. Of necessity, two-dimensional crystals, glasses, and gases are represented, but the essential points to be noted correspond to their actual, three-dimensional, physical counterparts. For the two sketches representing ideal crystal (a) and glass (b) lattices, the solid dots denote the equilibrium positions about which the atoms oscillate; for the gas (c), the dots denote a snapshot of one configuration of instantaneous atomic positions.

For an amorphous solid, the essential aspect from which its structure differs, with respect to that of a crystalline solid, is the absence of long-range order. There is no translational periodicity. This fundamental difference is evident at a glance in Figs. 2.5a and 2.5b.

On the other hand, the atomic positions in the glass are not randomly distributed in space. Randomness is a trait more properly associated with Fig. 2.5c, at least in the low-density limit, in which the atoms comprising the gas may be viewed as point particles. For such a dilute gas (the ideal gas of the kinetic theory), the particle positions are totally uncorrelated. Each atom may be located anywhere, independent

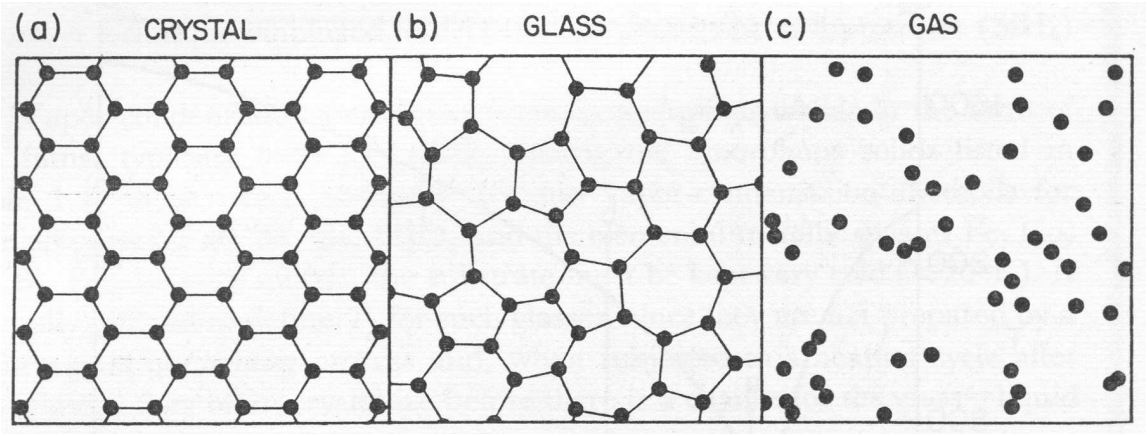


**Fig. 2.5**: Schematic sketches of the atomic arrangements in (a) a crystalline solid, (b) an amorphous solid, and (c) a gas. (Figure from [1])

of the positions of all other atoms. But in Fig. 2.5b, a high degree of local correlation can be easily observed. Each atom has (in the example used here for illustration) three nearest neighbors at nearly the same distance from it. Nearest-neighbor atoms are connected by lines in the figure and the bond angles formed where these lines meet at an atomic position are also nearly equal.

In the crystalline case of Fig. 2.5a, the nearest-neighbor separations and bond lengths are exactly equal (remember that we are dealing with the equilibrium positions), rather than nearly equal as in the glass. The degree of local correlation in amorphous solids is quantitatively described in the following chapters; it suffices here to say that this local order is quite high. Thus glasses have, in common with crystals, a high degree of short-range order. As in crystals, this is a consequence of the chemical bonding responsible for holding the solid together.

Thus, while the lack of long-range order in glasses implies randomness at large separations (knowing the positions of a few atoms does not help to locate, as it does in a crystal, the positions of distant atoms), the atomic-scale structure is highly nonrandom for a few interatomic distances about any given atom. A simple thought experiment serves as one way of demonstrating (other than by just looking) the presence of local order in Figs. 2.5a and 2.5b and its absence in Fig. 2.5c. Suppose a single atom is plucked out of each panel of the figure by a man with a bad memory. If he later wished to reinsert each atom in its original position, he would have no difficulty doing so for Figs. 2.5a and 2.5b. Not so, however, for Fig. 2.5c; since it is completely random, the remaining atomic positions provide no clue about the missing one.

In technical terms, amorphous carbon has localized $\pi$ electrons (as opposed to the aromatic $\pi$ bonds in graphite), and their bonds are formed in lengths and distances that are inconsistent with any other allotrope of carbon. It also contains a high concentration of dangling bonds, which cause deviations in interatomic spacing, and noticeable variation in bond angle.

As in the crystalline case, each of the bond hybridizations is available to a-C counterparts. This enables the large variation in the physical properties of a-C films. Due to bond variations, there is also a significant amount of confusion as to the terminology used to refer to a particular type of a-C thin film.

During the irradiation of diamond by atoms, many bonds are broken, leading to point defects and eventually to clusters of defects. At a high enough irradiation dose, amorphization of the crystal structure may occur and two specific amorphous forms of carbon may appear: the tetrahedrally bonded Diamond-like Amorphous Carbon which will be denoted by ta-C and the $sp^2$ bonded Graphite-like Amorphous Carbon named a-C. These two structures can be clearly distinguished by their macroscopic and microscopic properties. The former material has higher density, is transparent, electrically insulating and much harder than the latter. From the microscopic point of view, the ratio of fourfold, diamond-like bonds to threefold, graphite-like bonds ($sp^3/sp^2$) determines the kind of structure obtained.

Generally we can characterize the amorphous structures by the high degree of short range order and the absence of long range order. On one hand, in amorphous structures, the bond length, the number of nearest neighbor atoms and the angle between two bonds are close to those in crystalline structure, which gives rise to short range order.

On the other hand, there is no periodicity in the amorphous structure, i.e. one cannot built the entire lattice from a unit cell by means of appropriate translations. This lack of long range order breaks symmetries and gives isotropic characteristics to the structure.

From the energetic point of view, atoms in an amorphous crystal are not bonded ideally, they are subject to significant stresses and distortions. The energy of an amorphous solid is thus higher than that of a pure crystal.

While entirely amorphous carbon can be made, most of the material described as "amorphous" actually contains crystallites of graphite or diamond with various amounts of amorphous carbon holding them together, making them technically polycrystalline or nanocrystalline materials. Commercial carbon also usually contains significant quantities of other elements, which may form crystalline impurities.

#### 2.2.3.2 Diamond-like amorphous carbon

Ta-C is a hard and dense material, mostly made of distorted $sp^3$ bonds. A considerable amount of strain exists, due to localized melting and rapid quenching during its formation, that leaves the lattice in a stressed state. Part of the internal strain energy is relieved by the presence of $sp^2$ bonded atoms. These threefold atoms tend to form small clusters, owing to the delocalization of the $\pi$ states, and perhaps $\pi$-bonded pairs, and are thought to control the band gap. Moreover, an annealing process at high temperature may relieve stresses and bring the sample to a still dense but $sp^2$-rich phase. This is explained by the fact that threefold sites are the energetically favorable geometry. Temperature will supply the necessary energy to remove weakly bonded $sp^3$ atoms from their sites. The bonds are then transformed to $sp^2$ bonds, relieving the local strain and lowering the energy.

For instance, in the ta-C structure, the mean number of nearest neighbor atoms (the coordination number) is $z$=3.5-3.8, the mean bond length is 1.50-1.53 Å, and the mean bond angle 110-115°. The way the amorphous diamond is prepared strongly affects the properties of the structure, therefore the data that characterize these properties cannot be specified exactly. They lie in a range that will define the structure in consideration.

#### 2.2.3.3 Graphite-like amorphous carbon

The a-C lattice has a less dense structure and is mainly $sp^2$ bonded. In an a-C sample threefold coordinated atoms tend to form large clusters embedded in a matrix of fourfold atoms. These $sp^2$ bonds are distorted and non planar, and the threefold atoms form thick layers, which are spaced more closely than the sheets of graphite.

### 2.2.4 Fullerenes

The fullerenes [32] are a recently-discovered family of carbon allotropes. They are molecules composed entirely of carbon, in the form of a hollow sphere, ellipsoid, or tube. Spherical fullerenes are sometimes called buckyballs (Fig. 2.6a), and cylindrical fullerenes are called buckytubes. Fullerenes are similar in structure to graphite, which is composed of a sheet of linked hexagonal rings, but they contain pentagonal (or sometimes heptagonal) rings that prevent the sheet from being planar.

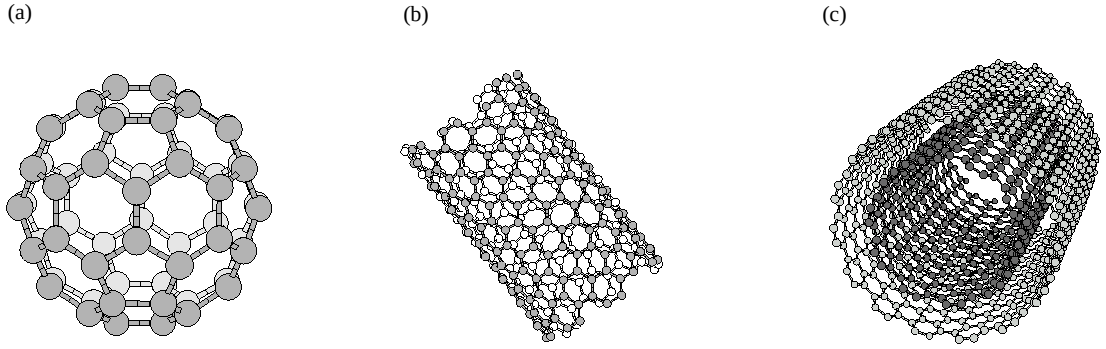


**Fig. 2.6**: Fullerenes: (a) a $C_{60}$ buckyball, (b) a single-wall nantube, and (c) a multi-wall nanotube.

#### 2.2.4.1 Nanotubes

Carbon nanotubes [33] are cylindrical carbon molecules with novel properties that make them potentially useful in a wide variety of applications (e.g., nanoelectronics, optics, materials applications, etc.). They exhibit extraordinary strength and unique electrical properties, they can be either metallic or semiconducting depending on their chirality, and are efficient conductors of heat. Inorganic nanotubes have also been synthesized.

A nanotube (also known as a buckytube) is a member of the fullerene structural family, which also includes buckyballs. Whereas buckyballs are spherical in shape, a nanotube is cylindrical, with at least one end typically capped with a hemisphere of the buckyball structure. Their name is derived from their size, since the diameter of a nanotube is on the order of a few nanometers (approximately 50,000 times smaller than the width of a human hair), while they can be up to several micrometers in length. There are two main types of nanotubes: single-walled nanotubes (SWNTs) (Fig. 2.6b) and multi-walled nanotubes (MWNTs) (Fig. 2.6c).

Nanotubes are composed entirely of $sp^2$ bonds, similar to those of graphite. This bonding structure, stronger than the $sp^3$ bonds found in diamond, provides the molecules with their unique strength. Nanotubes naturally align themselves into "ropes" held together by Van der Waals forces. Under high pressure, nanotubes can merge together, trading some $sp^2$ bonds for $sp^3$ bonds, giving great possibility for producing strong, unlimited-length wires through high-pressure nanotube linking.

# Chapter 3

# Tight - Binding Molecular Dynamics

*In this dissertation, we use tight-binding molecular dynamics simulations in order to study carbon. We use two different models in order to make sure that our results are independent of the hamiltonian used. Our simulations are done by using the canonical ensemble, which means that simulations are carried out at constant volume and temperature.*

## 3.1 General

The tight-binding (TB) method bridges the gap between classical and first-principles calculations. It is more accurate and transferable than empirical schemes because it provides a quantum-mechanical description of the interactions. On the other hand, while less accurate than *ab initio* approaches, it yields greater statistical precision and allows the use of larger cells, which compensate in part the sacrifice in accuracy.

In bibliography TB method is known with an additional name; it is called linear combination of atomic orbitals (LCAO). As its name shows, the major idea of LCAO method is the attempt to represent the unknown wave function, $\psi(\mathbf{r})$, on the basis of atomic orbitals considered to be known.

The TB approximation deals with the case in which the overlap of atomic wave functions is enough to require corrections to the picture of isolated atoms, but not so much as to render the atomic description completely irrelevant. The approximation is most useful for describing the energy bands that arise from partially filled $d$-shells of transition metal atoms and the electronic structure of insulators. Quite apart from

its practical usefulness, the TB approximation provides an instructive way of viewing Bloch levels complementary to that of the nearly free electron picture, permitting a reconnciliation between the apparently contradictory features of localized atomic levels on the one hand, and free electron-like plane-wave levels on the other.

A great disadvantage of TB method is the presence of parameters, which may be some dozens in a realistic problem. One way to determine these parameters is by *ab initio* calculations, which sometimes are very difficult to do. So, there are only two solutions to follow; either you can get the values of parameters from hand books [34], or you can represent them through atomic quantities and bond lenghts [35].

As we mentioned, the wave function, $\psi$, is written as a linear combination of atomic-like orbitals, $\phi$, which are the basis functions

$$|\psi >= \sum_{i\alpha}^{N_b} c_{i\alpha}|\phi_\alpha > \tag{3.1}$$

where $N_b$ is the dimension of the basis set and equals the product of the number of atoms in the system, $N_\alpha$, times the number of orbitals per atom, $N_o$, as $N_b = N_\alpha N_o$. The index in the sum runs over all atoms ($i$) and orbitals ($\alpha$). The coefficients $c_{i\alpha}$ are actually the weights of each orbital at a given atomic site and are complex numbers. The orbitals are centered around atoms and decay rapidly. Therefore, the matrix elements of different orbitals are actually non-zero only for on-site terms and between pairs of neighboring atoms (with a relative distance less than a certain cutoff).

The starting point of the method is Schrödinger's equation

$$H|\psi >= \epsilon|\psi > \tag{3.2}$$

where $H$ is the hamiltonian of the system and $\epsilon$ is the energy.

We replace in eq. (3.2) the wave function, $\psi$, from eq. (3.1). Additional, we assume that the basis is not orthonormal in general, i.e. $< \phi_\alpha|\phi_\beta >= S_{\alpha\beta} \neq \delta_{\alpha\beta}$ where $S_{\alpha\beta}$ are the overlap parameters. After that we get a generalized eigenvalue problem

$$\sum_{j\beta}(H_{i\alpha j\beta} - \epsilon_i S_{\alpha\beta})c_{j\beta} = 0 \tag{3.3}$$

or in a matrix form

$$\mathbf{Hc} = \epsilon\mathbf{Sc} \tag{3.4}$$

where $\mathbf{c}$ is the vector of the coefficients $c_\alpha$, $\mathbf{H}$ and $\mathbf{S}$ is the hamiltonian and overlap matrix, respectively.

The Hamiltonian matrix elements are given by the relation

$$H_{i\alpha j\beta} =< \psi|H|\psi >= c^*_{i\alpha}c_{j\beta} < \phi_\alpha|H|\phi_\beta > \tag{3.5}$$

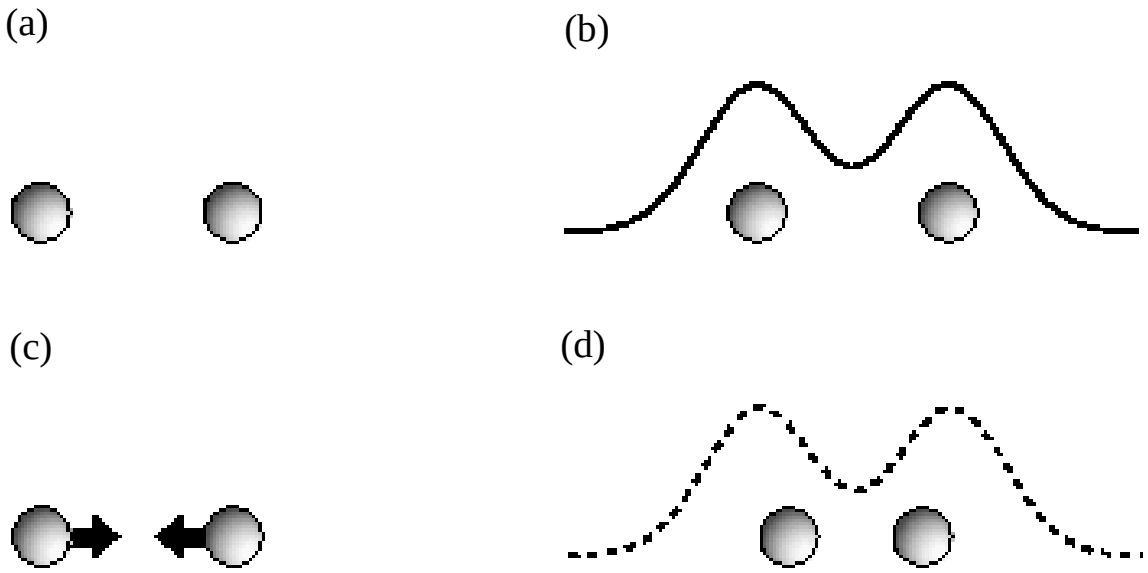


**Fig. 3.1**: The four steps, followed during an MD simulation is proceeded.

and the TB problem is reduced to the diagonalization of the Hamiltonian and the extraction of the eigenvectors $c_{i\alpha}$ that are related to the wavefunctions, as well as the eigenvalues $\epsilon_i$ that give the energy levels.

In the TB method, the total energy of the system is written as

$$E_{tot} = E_{bs} + E_{rep} \tag{3.6}$$

The first term represents the electronic band-structure energy, i.e., the sum of the eigenvalues over all occupied electronic states and the second term includes all the repulsive energies.

When the TB method is coupled with the dynamics and motion of particles in a system, the resulting simulational method is called tight-binding molecular dynamics (TBMD). The molecular dynamics (MD) method is simply a method for integrating the classical equations of motion of the atoms, which are given by

$$M_I \ddot{\mathbf{R}}_I = \mathbf{F}_I \tag{3.7}$$

The MD simulations proceed in four steps (Fig. 3.1):
(a) The positions of the atoms are given as input and are used to calculate the Hamiltonian of the system.
(b) The electronic ground state of the system is calculated by finding the eigenvalues and eigenvectors of the Hamiltonian.

(c) The eigenvectors are used to derive the forces on the atoms.
(d) Knowing the forces on the atoms we can integrate the equations of motion for the ions and find the new atomic positions.

## 3.2 Ames model

We first treat the interatomic interactions in a-C networks using the enviroment-dependent tight-binding (EDTB) model of Tang, Wang, Chan and Ho [36]. This tight-binding model goes beyond the traditional two-center approximation and allows the hopping parameters and the repulsive energy to be dependent on the binding enviroment.

While the two-center approximation greatly simplifies the TB parametrization, neglecting multicenter interactions are justified only when the electrons are well localized in strong covalent bonds. For systems, where metallic effects are significant, the two-center approximation is inadequate. In order to generate a tight-binding model that has good transferability over a wide range of coordination numbers, one can include multicenter interactions by allowing the interatomic interactions to depend on the binding environment.

So this model, which has been tested for the case of carbon, describes properly the higher-coordinated metallic structures in addition to the diamond, graphite and linear chain structures. Compared to the previous two-center model of Xu, Wang, Chan and Ho [37], the EDTB model improves remarkably the accuracy and transferability. The model has been used with success in specific problems related to carbon systems, such as the study of carbon $1s$ core-level shifts in a-C [38] and the surface reconstructions of "bucky diamonds" [39].

In this approach, the environment dependence of the hopping parameters is modeled through incorporating two new scaling functions into the traditional two-center integrals. A minimal basis set of one $s$ and three $p$ atomic orbitals is used to construct the tight-binding Hamiltonian for carbon with the hopping parameters and the pairwise repulsive potential expressed as

$$h(r_{ij}) = \alpha_1 R_{ij}^{-\alpha_2} e^{-\alpha_3 R_{ij}^{\alpha_4}} (1 - S_{ij}) \tag{3.8}$$

The first one is a screening function, $S_{ij}$, which mimics the electronic screening effects in solids, such that the interaction strength between two atoms in the solid becomes weaker if there are intervening atoms located between them. This approach allows us to distinguish between first- and farther neighbor interactions within the same interaction potential without having to specify separate interactions for first

and second neighbors. The screening function is modeled as

$$S_{ij} = \frac{e^{\xi_{ij}} - e^{-\xi_{ij}}}{e^{\xi_{ij}} + e^{-\xi_{ij}}} \tag{3.9}$$

with

$$\xi_{ij} = \beta_1 \sum_j exp\Big[ - \beta_2 \Big( \frac{r_{il} + r_{jl}}{r_{ij}} \Big)^{\beta_3} \Big] \tag{3.10}$$

The screening function varies smoothly from 0 to near 1 as $\xi$ is increased. In general, we require that $S_{ij}$ is near 0 if $i$ and $j$ are nearest-neighbor atoms, and close to 1 otherwise so that nearest-neighbor interactions dominate.

The second function, $R_{ij}$, scales the distance between two atoms according to their effective coordination numbers. Longer effective bond lengths are assumed for higher-coordinated atoms. The scaling function, between the real $r_{ij}$ and the effective $R_{ij}$ interatomic distance, is defined by

$$R_{ij} = r_{ij} \Big\{ 1 + \frac{\delta}{2} \Big[ \Big( \frac{g_i - g_0}{g_0} \Big) + \Big( \frac{g_j - g_0}{g_0} \Big) \Big] \Big\} \tag{3.11}$$

where $g_i$ and $g_j$ are the effective coordination numbers of atoms $i$ and $j$, and $g_0$ denotes the coordination number for a reference atom in a reference structure and they are given by

$$g_i = \sum_j (1 - S_{ij}) \tag{3.12}$$

Note that when $i$ and $j$ are nearest-neighbor atoms, $S_{ij}$ is close to 0 and $g_i$ counts almost one neighbor. On the other hand, $S_{ij}$ is close to 1 if $i$ and $j$ are not nearest-neighbor atoms, so that $g_i$ counts only a small fraction of a neighbor. So $g_i$ provides a continuous and smooth function for counting the neighbors.

The strength of the hopping parameters between atoms $i$ and $j$ is therefore dependent on the coordination number of the atoms: weaker interaction strength for larger-coordinated structures. This model preserves the two-center form of the tight-binding hopping integral. Note that expression (3.8) reduces to the traditional two-center formula if we set $R_{ij} = r_{ij}$ and $S_{ij} = 0$, while it is taking multicenter effects into account.

Besides the hopping parameters, the diagonal matrix elements in this model are also dependent on the bonding environments. The expression for the diagonal matrix elements is

$$e_{\lambda,i} = e_{\lambda,0} + \sum_j \Delta e_\lambda(r_{ij}) \tag{3.13}$$

where $\Delta e_\lambda(r_{ij})$ takes the same expression as (3.8) and $\lambda$ denotes the two types of orbitals.

Finally, the repulsive energy term is expressed by

$$E_{rep} = \sum_i f\Big(\sum_j \phi(r_{ij})\Big) \tag{3.14}$$

where $\phi(r_{ij})$ is a pairwise potential between atoms $i$ and $j$ and $f$ is a functional expressed as a fourth-order polynomial with argument $\sum_j \phi(r_{ij})$. So the eq. (3.14) can be coupled with the eq. (3.6) and give us the total energy of the system described by this model.

The parameters in the model ($\alpha$'s, $\beta$'s etc.) are determined by first fitting to the electronic band structures and then the cohesive energy versus volume curves for linear chain, graphite, diamond, simple cubic, bcc, and fcc structures, respectively obtained by the self-consistent first-principles density-functional theory calculations.

## 3.3 NRL model

During our study, we used another TB scheme to ensure that our results are independent of the hamiltonian. We applied to our methodology a TB method introduced by Mehl and Papaconstantopoulos [40, 41]. They present a general tight-binding total-energy (TBTE) method, which uses an analytic set of two-center, nonorthogonal tight-binding parameters, on-site terms that change with the local enviroment, and no pair potential.

One essential feature of TBTE methods that has not been emphasized is the choice of zero for the band structure term. In density-functional theory (DFT) [42] the total energy can be written in the form

$$E[n(\mathbf{r})] = \sum_i f(\mu - \epsilon_i)\epsilon_i + F[n(\mathbf{r})] \tag{3.15}$$

where the first term is the "band structure energy". Many TBTE models use a parametrized pair potential to represent $F[n(\mathbf{r})]$. However, there is a fundamental problem with this approach that appears not to have been widely recognized.

Mehl and Papaconstantopoulos have solved this problem by eliminating the pair potential from the tight-binding total energy. An alternative method of applying tight binding to eq. (3.15) has been developed, based on the fact that the Kohn-Sham formulation of DFT allows the eigenvalues to be shifted by an arbitrary constant $V_0$, often called the "muffin-tin zero". If this shift is defined to be

$$V_0 = \frac{F[n(\mathbf{r})]}{N_e} \tag{3.16}$$

where $N_e = \sum_i f(\mu - \epsilon_i)$ is the number of electrons in the system, then the eigenvalues $\epsilon_i$ are each shifted by an amount $V_0$, to the new values

$$\epsilon_i' = \epsilon_i + V_0 \tag{3.17}$$

Then the total energy (3.15) becomes

$$E[n(\mathbf{r})] = \sum_i f(\mu' - \epsilon_i')\epsilon_i' \tag{3.18}$$

where $\mu' = \mu + V_0$ is the shifted chemical potential.

The two-center Slater-Koster formulation of tight binding with a nonorthogonal basis breaks the problem into the calculation of three types of parameters: on-site parameters, which represent the energy required to place an electron in a specific orbital; Hamiltonian parameters, which represent the matrix elements for electrons hopping from one site to another; and overlap parameters, which describe the mixing between the nonorthogonal orbitals on neighbor sites. The eigenvalues $\epsilon_i'$ can be determined once the parameters are evaluated for a given structure.

In an orthogonal tight-binding calculation, applying the shift to each eigenvalue would be equivalent to shifting each diagonal element of the Hamiltonian matrix by an amount $V_0$. In the nonorthogonal case the effect is slightly more complicated. It is clear, however, that the Hamiltonian and overlap parameters should not directly depend on the shift $V_0$. Thus the shift effect can only be accounted by changing the on-site parameters.

On-site parameters must now be sensitive to the local environment around each atom. This is achieved by introducing a local "density", given by

$$\rho_i = \sum_j e^{-\lambda^2 \mathbf{R}_{ij}} F_c(\mathbf{R}_{ij}) \tag{3.19}$$

where $F_c$ is a smooth cutoff function. Then the on-site terms for each atom $i$ are fitted to a finite strain polynomial

$$h_{il} = a_l + b_l \rho_i^{2/3} + c_l \rho_i^{4/3} + d_l \rho_i^2 \tag{3.20}$$

where the index $l$ runs over all orbitals. In the case of carbon [43] only $s$ and $p$ orbitals are used and the cutoff function vanishes at 10.5 a.u.

On the other hand, the two-center Slater-Koster hopping terms for the Hamiltonian and overlap parameters are essumed to have the same functional form. They are simply polynomials multiplied by an exponential cutoff. Hamiltonian is defined as

$$H_{ll'\mu}(R) = (p_{ll'\mu} + q_{ll'\mu} R + r_{ll'\mu} R^2) e^{-s_{ll'\mu}^2 R} F_c(R) \tag{3.21}$$

The overlap parameters have a small difference in the Hamiltonian to exhibit the proper behavior as the atoms get close together and are written as

$$S_{ll'\mu}(R) = (\delta_{ll'} + t_{ll'\mu}R + u_{ll'\mu}R^2 + v_{ll'\mu}R^3)e^{-w^2_{ll'\mu}R}F_c(R) \tag{3.22}$$

where $\delta_{ll'}$ is the Kronecker delta function.

The parameters in the model $(\lambda,\ (a,b,c,d)_l,\ (p,q,r,s)_{ll'\mu}$ and $(t,u,v,w)_{ll'\mu})$, which are forty-one in the case of carbon [43], are simultaneously fitted to the band structures and total energies at different structures and volumes.

## 3.4 Canonical Ensemble - (N,V,T)

### 3.4.1 General

Statistical physics deals with the study of systems which are composed of a large number of particles, i.e. atoms, molecules, electrons, etc., and thus have many degrees of freedom. Its scope is to relate the microscopic level with the macroscopic one.

Let's say we have a classical system in equilibrium. This system is described by the Hamiltonian $H(\bar{r}^N, \bar{p}^N) = K + U$ which is the sum of the kinetic and potential energy of the particles. Here, $\bar{r}$ stands for the coordinates and $\bar{p}$ for the momenta of N particles. In this notation, the mean value of every observable quantity $A(\bar{r}^N, \bar{p}^N)$ is given by the sum over all states on the phase space, with respect to the stationary probability $P(\bar{r}^N, \bar{p}^N)$:

$$\langle A \rangle = \frac{1}{h^{3N}N!}\int A(\bar{r}^N, \bar{p}^N)P(\bar{r}^N, \bar{p}^N)d\bar{r}_N d\bar{p}_N \tag{3.23}$$

where the factor $h^{3N}$ is introduced because of the quantization of phase space while the factor N! because of the indistinguishability of identical particles.

In the case of the canonical ensemble, the quantities which are kept constant are the number of particles, the volume and the temperature of the system, (N,V,T). A schematic representation of this ensemble is shown in Fig. 3.2, in which the system is sketched inside a reservoir.

The proper thermodynamic potential, whose minimum determines thermal equilibrium is the Helmholtz free energy $F = E - TS = -k_B T \ln Z(N,V,T)$. On the other hand, the probability distribution is

$$P(\bar{r}^N, \bar{p}^N) = \frac{e^{-\beta H(\bar{r}^N, \bar{p}^N)}}{Z(N,V,T)} \tag{3.24}$$

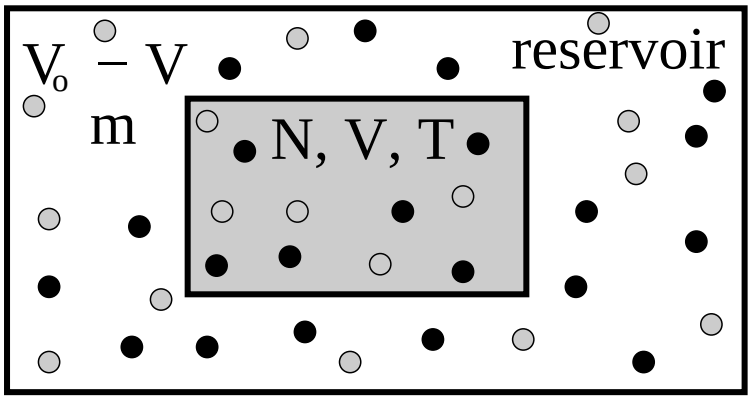


**Fig. 3.2**: Schematic representation of canonical ensemble. The number of particles, the volume and the temperature of the system are kept fixed, (N,V,T).

where

$$Z(N,V,T) = \frac{1}{h^{3N}N!}\int e^{-\beta H(\bar{r}^N,\bar{p}^N)}d\bar{r}^N d\bar{p}^N \tag{3.25}$$

is called the partition function of the system, $\beta = \frac{1}{K_B T}$ and $K_B$ is the Boltzmann factor.

Applying the above equations in Eq. 3.23 one gets:

$$\langle A\rangle = \frac{\int A(\bar{r}^N,\bar{p}^N)e^{-\beta H(\bar{r}^N,\bar{p}^N)}d\bar{r}^N d\bar{p}^N}{\int e^{-\beta H(\bar{r}^N,\bar{p}^N)}d\bar{r}^N d\bar{p}^N} \tag{3.26}$$

Note that the Hamiltonian is a quadratic function of momenta, meaning that the integrations with respect to the latter can be carried analytical. On the other hand, the integration of functions $A(\bar{r}^N)$, like the potential energy $U(\bar{r}^N)$, over the configuration part of the phase space is the difficult part. In this case the integration over momenta cancels out, and Eq. 3.26 is written:

$$\langle A\rangle = \frac{\int A(\bar{r}^N)e^{-\beta U(\bar{r}^N)}d\bar{r}^N}{\int e^{-\beta U(\bar{r}^N)}d\bar{r}^N} \tag{3.27}$$

### 3.4.2 Temperature Control

In the standard MD method, the newtonian equations of motion of the particles in a fixed MD cell of volume $V$ are solved numerically. The total energy $E$ is conserved and thus the ensemble generated by the simulation is the microcanonical

or (N,V,E) ensemble. With the MD method, not only the static quantities but also the dynamic quantities can be obtained. This is one advantage over the classical methods. However, a disadvantage of the MD method is that the conditions of the simulations are not the same as those normally encountered in experiments (constant temperature, constant pressure or (N,P,T) conditions).

To perform MD simulations at constant temperature((N,V,T) conditions), the simplest way is to keep the kinetic energy constant by scaling the velocities at each time step. However, there seems to be no rigorous proof that the latter approach produces configurations belonging to the canonical ensemble.

Another method for constant temperature MD simulations was proposed by Andersen [44]. This is effectively a hybrid of MD and MC methods since the velocities of the particles are changed stochastically to produce the Boltzmann distribution.

Hoover *et al.* [45] also introduced a constraint method in which an additional velocity dependent term is added to the forces to keep the total kinetic energy constant. Their method produces the canonical distribution for the potential energy term. The fluctuations of the kinetic energy are suppressed.

### 3.4.3 Nosé-Hoover thermostat

Another molecular dynamics method at constant temperature is proposed by Nosé [46, 47] and Hoover [48]. This method introduces an additional degree of freedom, so the total energy of the physical system is allowed to fluctuate. A special choice of the potential, for the extra degree of freedom, guarantees that the averages of static quantities in this method are equal to those in the canonical ensemble.

An additional term is used, $-\zeta \mathbf{p}_i$, to the force term and the equations of motion using the Nosé-Hoover thermostat, transform to

$$\frac{d\mathbf{q}_i}{dt} = \frac{\mathbf{p}_i}{m_i} \tag{3.28}$$

$$\frac{d\mathbf{p}_i}{dt} = -\frac{\partial \Phi}{\partial \mathbf{q}_i} - \zeta \mathbf{p}_i \tag{3.29}$$

where $\mathbf{q}_i$, $\mathbf{p}_i$ are the atomic coordinates and momenta, $m_i$ the particle mass and $\Phi$ the potential energy.

The parameter $\zeta$ is determined by the requirement that the total kinetic energy is constant

$$\sum_i \frac{\mathbf{p}_i^2}{2m_i} = \frac{gkT}{2} \qquad \text{or} \qquad \sum_i \mathbf{p}_i \frac{d\mathbf{p}_i}{dt}/m_i = 0 \tag{3.30}$$

Thus, we get

$$\zeta = -\frac{\sum_i \frac{\partial \Phi}{\partial \mathbf{q}_i} \mathbf{p}_i / m_i}{\sum_i \frac{\mathbf{p}_i^2}{m_i}} \tag{3.31}$$

# Chapter 4

# Methodology

*The procedure we follow to construct our amorphous carbon networks is the "quenching from the liquid" method, in some respects similar to the experimental practice. We also consider fully tetrahedral amorphous networks, simulating the hypothetical "amorphous diamond" phase, based on the well known WWW model. Such networks offer an upper bound to the properties of a-C. Our nanodiamond composites are generated from pure diamond by keeping the core frozen and melting the surrounding matrix. Moreover, the methoology used to analyse the computer generated networks is presented and discussed.*

## 4.1 Formation of a-C networks

What is a "solid"? In a familiar type of thought experiment, often invoked to conceptually analyze the energetics involved in the formulation of a solid, a large collection of initially isolated atoms is gradually brought together "from infinity" until the actual interatomic spacings of the solid are attained. The actual experiment, that most closely corresponds to this gedanken experiment, involves cooling the vapor of the material until it condenses into the liquid state, and then further gradual cooling of the liquid until it solidifies. Results of such an experiment, for a given quantity of the material, may be represented on a volume-versus-temperature $V(T)$ plot such as the one schematically shown in Fig. 4.1.

Figure 4.1 should be read from right to left, since time runs in that direction during the course of the quenching (temperature-lowering) experiment. A sharp break or bend in $V(T)$ marks a change of phase occurring with decreasing temperature. The first occurs when the gas (whose volume is limited only by the dimensions of the experimental enclosure) condenses to the liquid phase (of well-defined

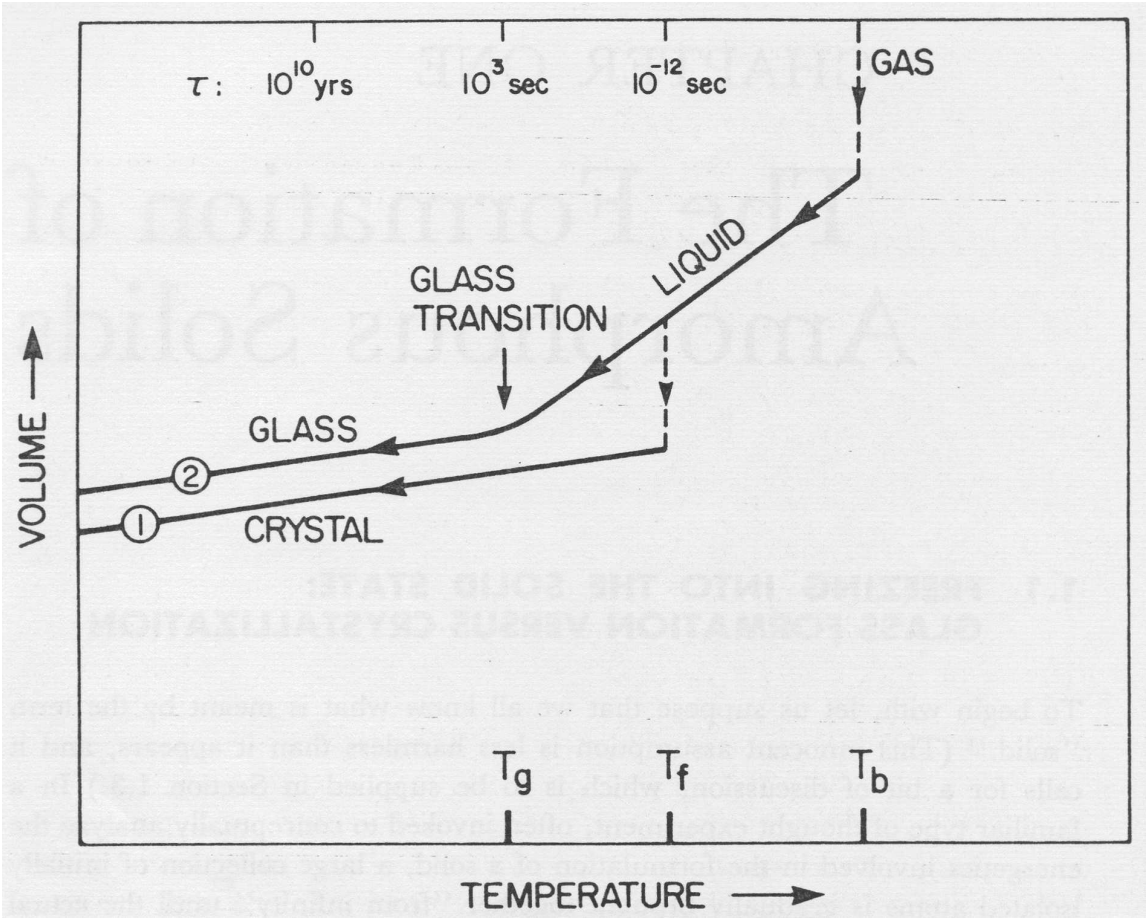


**Fig. 4.1**: The two general cooling paths by which an assembly of atoms can condense into the solid state. Route (1) is the path to the crystalline state; route (2) is the rapid-quench path to the amorphous solid state.(Figure from [1])

volume, but shape enclosure-determined) at the boiling temperature $T_b$. Continued cooling now decreases the liquid volume in a continuous fashion, the slope of the smooth $V(T)$ curve defining the liquid's volume coefficient of thermal expansion $\alpha = (1/V)(\partial V/\partial T)_P$. (The experiment is assumed to be taking place at low pressure, $P \approx 0$.) Eventually, when the temperature is brought low enough, a liquid-to-solid transition takes place (with the exception of liquid helium, which remains liquid as $T \to 0$ in the absence of pressure). The solid then persists to $T = 0$, its signature in terms of $V(T)$ being a small slope corresponding to the low value (relative to that of the liquid phase) of the expansion coefficient a which characterizes a solid.

A liquid may solidify in two ways; either discontinuously to a crystalline solid or continuously to an amorphous solid (glass). The two solids resulting from these

two quite different solidification scenarios are labeled, correspondingly, (1) and (2) in Fig. 4.1. Scenario (1) occurs at temperature $T_f$, the freezing (or melting) point. The liquid-to-crystal transition is marked by a discontinuity in $V(T)$, an abrupt contraction to the volume of the crystalline solid. In a quenching experiment carried out at a sufficiently low cooling rate, this is usually the route taken to reach the solid state. But at sufficiently high cooling rates, it is found that most materials alter their behavior and follow route (2) to the solid phase. $T_f$ is bypassed without incident, and the liquid phase persists until a lower temperature $T_g$ is reached. Here the second solidification scenario is realized. The liquid-to-glass transition occurs in a narrow temperature interval near $T_g$, the glass transition temperature. There is no volume discontinuity, instead $V(T)$ bends over to acquire the small slope (similar to that of the crystal) characteristic of the low thermal expansion of a solid.

Both crystals and glasses are bona fide solids and share the essential attributes of the solid state. Their fundamental difference is in the basic nature of their microscopic, atomic-scale structure. In crystals, the equilibrium positions of the atoms form a translationally periodic array. The atomic positions exhibit long-range order. In amorphous solids, long-range order is absent; the array of equilibrium atomic positions is strongly disordered. For crystals, the atomic-scale structure is securely known at the outset from the results of diffraction experiments, and it provides the basis for the analysis of such properties as electronic and vibrational excitations. For amorphous solids, the atomic-scale structure is itself one of the key mysteries.

A note on terminology is in order at this point. The term amorphous solid is the general one, applicable to any solid having a nonperiodic atomic array as outlined above. The term glass has conventionally been reserved for an amorphous solid actually prepared by quenching the melt, as in (2) of Fig. 4.1. Since there are other ways to prepare amorphous solids than by melt-quenching, glass (in the conventional usage) is the more restrictive term. In this thesis, both terms will be used synonymously. Not only does this lubricate the discussion because "glass" is one word while "amorphous solid" is two, it is also convenient to have "glass" to set in opposition to "crystal" (instead of "amorphous solid" versus "crystalline solid"). Other terms, sometimes used in the literature in place of amorphous solid, are noncrystalline solid and vitreous solid.

The a-C networks are generated by quenching from the melt, as described previously. Although not directly related to the kinetics of the growth process of a-C films, it produces generic structures associated with the equilibrium state of the films. (For a thorough discussion of this and other points dealt with in this subsection, see Ref. [18].)

We used cubic computational cells of about 200 - 500 atoms with periodic bound-

ary conditions. We first equilibrated well various carbon liquid structures at different densities, at 12000 K. Quenching of the liquid structures was then performed within temperature intervals of 500 K down to 0 K, each of them lasting for 2000 time steps. The size of the time step used was 1.05 $\times 10^{-15}$ s, i.e., the total quench time was 52.5 ps and the quench rate 226 K/ps. During quenching, the volume/density of the cells was kept constant. After quenching, the density (volume) was allowed to relax by changing homogeneously the dimensions of the cells within small increments and seeking energy minimization, still within the $(N, V, T)$ ensemble.

The relaxation of volume and density is important because it brings the system to its ground state and eliminates any external forces and constrains. In fact, we observed that in most cells the change in density between the initial, as quenched structure, and the final ground state structure was significant, of the order of 0.1 gcm$^{-3}$. This shows that the unrelaxed cells were under external stress [18].

## 4.2 The WWW model

Besides the cells formed by quenching, we also examined the properties of another generic structure. This is based on the Wooten-Winer-Waire (WWW) model [49, 50] of a-C, which is a hypothetical model of "amorphous diamond", completely tetrahedral, constructed by a computer algorithm that generates realistic random-network models of amorphous solids.

WWW models take in mind a critical aspect of the amorphous structure, which demands attention. This is the homogeneous structure, thought to be typical of the bulk material, and is generally believed to be a continuous random network. Continuous random-network structures, constructed by WWW algorithm, preserve local order, but bond angles and bond legths are somewhat distorted. Their topology also includes fivefold and sevenfold rings in addition to sixfold rings characteristic of the diamond structure. The models also obey to periodic boundary conditions to avoid the awkward problems posed by free surfaces. This method differs from earlier approaches in its conceptual simplicity and in the inclusion of a Maxwell-Boltzmann factor, which is essential for construction of models.

The methodology of constructing fully tetrahedral a-C follows. The starting structure is a perfect diamond crystal. Periodic boundary conditions are imposed so that the structure is completely tetrahedrally coordinated, i.e. there are no dangling bonds anywhere. The bond-bending and bond-stretching forces are described by a Keating potential [51, 52].

The first step after generating the initial crystal structure is to randomize the

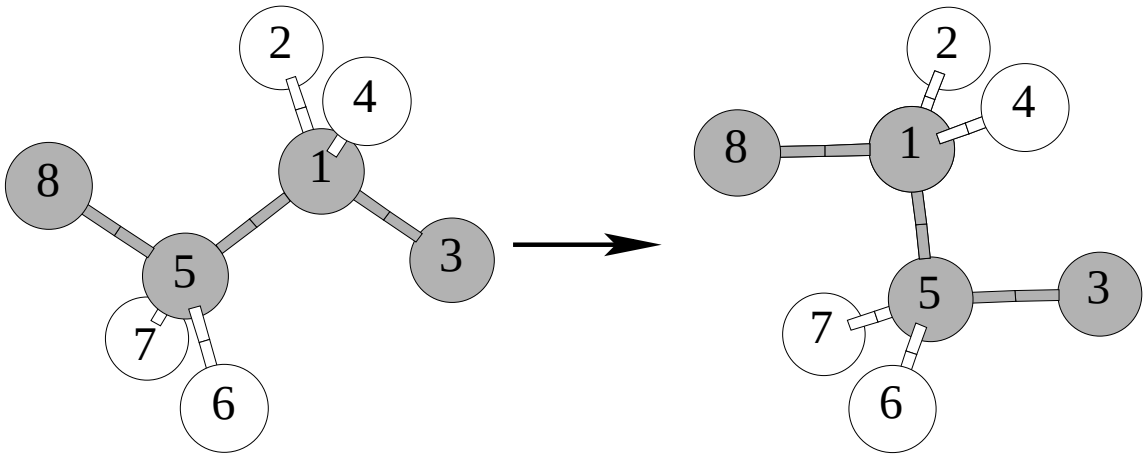


**Fig. 4.2**: Bond switch move. The elementary rearrangement applied by Wooten *at al.* [49].

network sufficiently, so that subsequent annealing will not lead the system back to the crystalline state. The randomization process is realized by the introduction of many bond switches (see Fig. 4.2) at a temperature just above the melting point for the model. The bond rearrangements maintain fourfold coordination at each atom, thus introducing large strain in the structure and constructing five- and sevenfold rings.

In the second stage of the procedure, the temperature is reduced in small steps, and at each new temperature, thermal equilibrium is established. The system is relaxed geometrically (the release of the strain energy allowing the stretching and bending of bonds, according to the Keating potential [52]) and topologically (creating more bond switches in the system). After that, a long annealing process takes place, and finally a random network of comparatively low energy is obtained.

We used the 216-atom cell constructed by Djordjević, Thorpe, and Wooten [53]. We relaxed its topology and density with the tight-binding models. The cell remains perfectly tetrahedral. The WWW model, although hypothetical, is very useful because it provides an upper bound to the density, $sp^3$ fraction, and bulk modulus of a-C, and can directly be compared to the crystalline counterpart, diamond.

## 4.3 Generation of nanodiamond structures

The embedded nanostructures are formed using Monte Carlo (MC) simulations by melting and subsequent quenching at constant volume the corresponding crystal

structures, while keeping a certain number of atoms in the central portion of the cells frozen in their ideal crystal positions. This method is not directly related to the kinetics of the growth process of these materials, and is a nonequilibrium process, where a metastable state is produced by freezing-in continuously the nonequilibrium local structures. The procedure of quenching from the melt, actually, produces generic structures that cannot be directly associated with the nonequilibrium as-deposited structures, but can be definitely associated with and can be used to study the equilibrium ground state of na-C films.

After quenching, which produces amorphization of the surrounding matrix, the cells are thoroughly relaxed with respect to atomic positions and density. Relaxations are particularly important at the interface region, where the crystallites mainly adjust to the host environment. Periodic boundary conditions are applied to the cells. The total number of atoms is 512, while the number of atoms in the nanocrystals ranges from $\sim$ 100 to 200.

Continuing, we anneal the structures up to 1000K with the tight-binding models. We do that in order to relax the networks with the TB hamiltonians. Afterwards, we lower again the temperature at 0K and we allow the volume of the cells to relax by changing homogeneously its dimensions and seeking energy minimization, still within the (N,V,T) ensemble, as we did in the case of the formation of a-C networks.

Cells with various coordination (density) of the amorphous matrix can be formed by changing the initial starting density (volume) of the crystal structures. The size (radius) of the nanocrystals is controlled by the choice of the number of the shells kept frozen during quenching.

## 4.4 Analysis Tools

In order to describe an amorphous structure, the following characteristic quantities, among others, can be used: coordination number, radial distribution function and angular distribution function.

### 4.4.1 Radial distribution function

The radial distribution function (RDF), $J(r)$, is a generalization of the coordination number. Instead of only looking at the first nearest neighbours, RDF is a way to count the number of atoms that lie at a distance $r$ from a specific atom, averaging over all atoms of the lattice.

From a random atom chosen as the origin, $J(r)dr$ gives the probability of finding

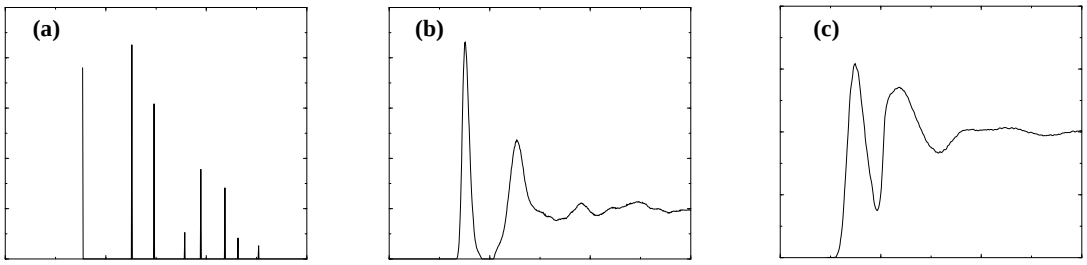


**Fig. 4.3**: Sketches of the pair distribution function for (a) diamond crystal, (b) a-C, and (c) liquid C.

a neighboring atom at a distance between $r$ and $r + dr$. For a crystal lattice with each atomic nucleus regarded as clamped to its equilibrium position (lattice site), the RDF is a sum of delta functions, with each corresponding to a coordination shell (Fig. 4.3a)

$$J_{cr}(r) = \sum_i z_i(r)\delta(r - r_i) \tag{4.1}$$

Except for that fact, the spikes in $J(r)$ for a crystal are broadened by thermal and zero-point motion. Despite this blurring, well-defined peaks can be seen in the experimentally determined RDFs for crystals out to about a dozen coordination shells.

Direct evidence of the existence of short-range order in glasses, in the form of well-defined nearest-neighbor and next-nearest-neighbor coordination shells, is provided by the presence of the clearly seen first and second peaks in the RDF (Fig. 4.3b). On the other hand, the absence of long-range order manifests itself in the fact that, for glasses, discernible peaks in the RDF rarely occur beyond third-nearest neighbor. Similar remarks apply to the RDF of liquids (Fig. 4.3c).

For point particles distributed randomly in space with an average number density (number of atom centers per unit volume), $\rho(r)$, at a distance $r$ from an average atom center, the RDF follows directly from the fact that the expected number of particles in a shell of volume $4\pi r^2 dr$ is just that volume element times $\rho$

$$J(r) = 4\pi r^2 \rho(r) \tag{4.2}$$

The RDF is obtained as a Fourier transformation of the observed momentum distribution

$$J(r) = 4\pi r^2 \rho_0 + rG(r) \tag{4.3}$$

where $\rho_0$ is the density of atom centers averaged over the sample and $G(r)$ is the reduced RDF defined by

$$G(r) = \frac{2}{\pi} \int_0^\infty dk[I(k) - 1]k \sin(kr) \tag{4.4}$$

where $I(k)$ is the normalized intensity distribution (structure factor) and $k$ is the scattering vector defined by

$$k = (4\pi/\lambda) \sin \phi \tag{4.5}$$

$\lambda$ being the wavelength of the probing radiation and $2\phi$ the scattering angle.
Compining eq. (4.2) and (4.3) we produce the following form for reduced RDF

$$G(r) = 4\pi r(\rho(r) - \rho_0) \tag{4.6}$$

Another expression for RDF, which is commonly used, is defined by

$$g(r) = \rho(r)/\rho_0 \tag{4.7}$$

### 4.4.2 Coordination number

The coordination number $z$ is the number of nearest neighbour atoms. For example, $z$ is 4 for the diamond structure, or 12 for the FCC structure. For perfect lattices, the coordination number has no real significance but for more complex structures, like amorphous lattices, it plays a crucial role in the determination of the amorphous structure type. It will be shown in the next section that $z$ for the amorphous material is very close to that of the corresponding crystal.

It can be noted that the coordination number may be measured by determining the integrated area under the first peak of radial distibution function. The number of particles located in the region between $r_1$ and $r_2$ are:

$$n = \int_{r_1}^{r_2} 4\pi r^2 \rho_0 g(r) dr \tag{4.8}$$

In the case where $r_1 = 0$ and $r_2$ is such that $g(r) = 0$, eq. 4.8 denotes calculation of the area under the first peak. This area is a direct expression of $z$.

### 4.4.3 Bond-angle distribution function

The bond angle distribution function $g(\theta)$ is defined for angles between nearest neighbors atoms. For a diamond crystal, $g(\theta)$ is a delta function centered at

$\theta = 109.47°$. For an amorphous crystal, $g(\theta)$ is centered at an angle close to the tetrahedral angle for the ta-C structure and to $\theta = 120°$ for the a-C structure. Large angle distortions occur in these structures, as indicated by the significant width of the bond angle distribution. Moreover, in the case of the a-C crystal, for example, $g(\theta)$ is not vanishing near the tetrahedral angle, thus part of the bonds, in that structure, may be defined as having a diamond-like angle nature. In experiment, the bond angle can be obtained by the ratio of the first and second neighbor distances ($r_0$ and $r_1$ respectively) as in

$$\theta = 2\arcsin(r/2r_0) \tag{4.9}$$

## 4.5 Bulk Modulus

A representative and important elastic quantity is the bulk modulus. It measures the response in pressure due to a change in relative volume. The equilibrium bulk modulus is defined as

$$B_{eq} = V(\frac{d^2E}{dV^2})_{V=V_{eq}} \tag{4.10}$$

and it is obtained by considering a uniform hydrostatic expansion or compression of the system and differentiating the curve of the energy as a function of volume. The minimum energy and volume and the corresponding bulk modulus of each cell were determined by fitting the energy-versus-volume data to Murnagham's equation of state [54].

## 4.6 Optical properties

### 4.6.1 Momentum matrix elements

For the discussion of the optical properties, one must calculate the momentum ($\mathbf{P}$) matrix elements from the TB wavefunction. We present here our contribution to this subject. By necessity, this calculation is an approximation, because we can not estimate them directly. These matrix elements are the basis for any subsequent evaluation of all optical quantities.

We begin with a rigorous relation between matrix elements of the momentum and the position operators between two eigenstates [35, 85]. These eigenstates are denoted by $|i\rangle$ and $|f\rangle$. The essential idea is contained in two evaluations of the "commutator"

$$C = \langle f|H\mathbf{r} - \mathbf{r}H|i\rangle \tag{4.11}$$

We first use the hamiltonian

$$H = -\frac{\hbar^2\nabla^2}{2m} + V(\mathbf{r}) \tag{4.12}$$

and we note that only the $\nabla^2$ gives extra terms, $\nabla^2\mathbf{r} - \mathbf{r}\nabla^2 = 2\nabla$, and $C$ becomes

$$C = \frac{\hbar}{im}\langle f|\mathbf{P}|i\rangle \tag{4.13}$$

For the second evaluation we use the definition of energy eigenstates

$$\langle f|H = E_f\langle f|, \tag{4.14a}$$

$$H|i\rangle = E_i|i\rangle \tag{4.14b}$$

where $E_i$, $E_f$ are the eigenvalues of $|i\rangle$, $|f\rangle$ eigenstates, respectively, and we obtain

$$C = (E_f - E_i)\langle f|\mathbf{r}|i\rangle \tag{4.15}$$

The whole combination gives

$$\hbar\langle f|\mathbf{P}|i\rangle = im(E_f - E_i)\langle f|\mathbf{r}|i\rangle \tag{4.16}$$

We now can use the principal idea of the LCAO method and write our eigenstates, $|i\rangle$ and $|f\rangle$, as a linear combination of the atomic states (orbitals), $|a\rangle$ and $|b\rangle$

$$|i\rangle = \sum_a c_a^{(i)}|a\rangle \tag{4.17a}$$

$$|f\rangle = \sum_b c_b^{(f)}|b\rangle \tag{4.17b}$$

where $c_k^{(n)}$ is the eigenvector for the $n$th eigenstate on $k$ atomic state. If we take in mind that $\langle k|\mathbf{r}|k\rangle \neq 0$ but $\langle k|\mathbf{r}|l\rangle = 0$, we can compute that

$$\langle f|\mathbf{r}|i\rangle = \sum_k c_k^{(f)*}c_k^{(i)}\langle k|\mathbf{r}|k\rangle = \sum_k c_k^{(f)*}c_k^{(i)}\vec{r}_k \tag{4.18}$$

Finally if we combine the previous expression with the eq. 4.16, we will obtain

$$\langle f|\mathbf{P}|i\rangle = \frac{im}{\hbar}(E_f - E_i)\sum_k c_k^{(f)*}c_k^{(i)}\vec{r}_k \tag{4.19}$$

Additional we can apply the rigorous result 4.16 to an approximate description of tight-binding states, taking the atomic state $|a\rangle$ at a nucleus a distance $\mathbf{d}$ from an atomic state $|b\rangle$. From these two states we construct a bonding eigenstate

$$|i\rangle = \sqrt{\frac{1-\alpha_p}{2}}|a\rangle + \sqrt{\frac{1+\alpha_p}{2}}|b\rangle \tag{4.20}$$

and an antibonding state

$$|f\rangle = \sqrt{\frac{1+\alpha_p}{2}}|a\rangle - \sqrt{\frac{1-\alpha_p}{2}}|b\rangle \tag{4.21}$$

where $\alpha_p$ is the polarity defined by

$$\alpha_p = \frac{V_3}{\sqrt{V_2^2 + V_3^2}} \tag{4.22}$$

and $V_3 = (E_a - E_b)/2$ and the coupling between them $V_2 = \langle a|H|b\rangle$.

Then we may substitute these into the rigorous relation given above, taking of course $\langle b|\mathbf{P}|a\rangle = -\langle a|\mathbf{P}|b\rangle$ and $\langle a|\mathbf{P}|a\rangle = \langle b|\mathbf{P}|b\rangle = 0$ and $\langle a|\mathbf{r}|b\rangle = \langle b|\mathbf{r}|a\rangle = 0$. We obtain

$$\hbar\langle a|\mathbf{P}|b\rangle = \frac{im}{2}\alpha_c(E_a - E_b)\mathbf{d} \tag{4.23}$$

and with

$$\alpha_c = \sqrt{1-\alpha_p^2} = \frac{2\langle a|H|b\rangle}{(E_a - E_b)} \tag{4.24}$$

gives a direct relation between the matrix elements

$$\hbar\langle a|\mathbf{P}|b\rangle = im\langle a|H|b\rangle\mathbf{d} \tag{4.25}$$

### 4.6.2 Dielectric function

A major part of this thesis regards the calculation of the optical properties of amorphous carbon. The central quantitiy, on which these properties are based on, is the complex dielectric function thus all the others ones are based on the latter, which is defined

$$\epsilon = \epsilon_1 + i\epsilon_2 \tag{4.26}$$

is defined in terms of its real

$$\epsilon_1 = n^2 - k^2 \tag{4.27}$$

and imaginary parts

$$\epsilon_2 = 2nk \tag{4.28}$$

where $n$ and $k$ are the refractive index and the extinction coefficient of the material, respectively [84].

The imaginary part of the dielectric function in the one-electron approximation takes the form [4]

$$\epsilon_2(\omega) = \frac{2}{V}\Big(\frac{2\pi e}{\omega m}\Big)\sum_{i,f}|\langle f|\mathbf{P}|i\rangle|^2\delta(E_f - E_i - \hbar\omega) \tag{4.29}$$

Now our problem is that the wave function for tight-binding models are not known and the momentum matrix elements $\langle f|\mathbf{P}|i\rangle$ can not be calculated directly. In this case, we use the approximation we derived above, as expressed by the relation (4.19). If we put it in the above relation and transform our variable from frequency $\omega$ to energy $E$ via $E = \hbar\omega$, we will obtain

$$\epsilon_2(E) = \frac{8\pi^2 e^2}{V}\frac{1}{E}\sum_{i,f}(E_f - E_i)^2(\sum_k c_k^{(f)*} c_k^{(i)} \vec{r}_k)^2 \delta(E_f - E_i - E) \tag{4.30}$$

where $V$ is the sample volume and the summations are over all the initial $|i\rangle$ and final $|f\rangle$ eigenstates, which have eigenvalues $E_i$ and $E_f$, respectively.

The real and imaginary parts of the optical function are related to each other through the general Kramers – Kronig dispersion relations

$$\epsilon_1(E) = 1 + \frac{2}{\pi}\int_0^\infty \frac{\xi}{\xi^2 - E^2}\epsilon_2(\xi)d\xi \tag{4.31}$$

### 4.6.3 Refractive index

We mentioned that the complex dielectric function of an amorphous semiconductor is defined in terms of its real and imaginary parts, $\epsilon_1$ and $\epsilon_2$, respectively, which are related to the refractive index $n$ and the extinction coefficient of the material $k$.

We can solve the eq. 4.28 to $k = \epsilon 2/2n$ and replace it into eq. 4.27. Then we get the following equation

$$4n^4 - 4\epsilon_1 n^2 - \epsilon_2^2 = 0 \tag{4.32}$$

The solution of eq. 4.32 has two forms

$$n^2 = \frac{\epsilon_1 + \sqrt{\epsilon_1^2 + \epsilon_2^2}}{2} \tag{4.33a}$$

$$n^2 = \frac{\epsilon_1 - \sqrt{\epsilon_1^2 + \epsilon_2^2}}{2} \tag{4.33b}$$

The first one is acceptable, because when $E \leq E_{gap}$ and $\epsilon_2 = 0$, $n^2$ equals to $\epsilon_1$, and when $E > E_{gap}$ and $\epsilon_2 > 0$, $n^2$ is a positive number. But the second one is not acceptable, because when $E \leq E_{gap}$ and $\epsilon_2 = 0$, $n^2$ equals to 0, and when $E > E_{gap}$ and $\epsilon_2 > 0$, $n^2$ is negative! So the square of the refractive index as a function of energy is given by the relation 4.33a.

### 4.6.4 Absorption coefficient

The absorption coefficient, $\alpha$, is related to the imaginary part of the dielectric function, $\epsilon_2$, via [4]

$$\alpha(\omega) = \frac{\omega\epsilon_2(\omega)}{nc} \tag{4.34a}$$

or, if we substitude $\omega$ with $E = \hbar\omega$

$$\alpha(E) = \frac{E\epsilon_2(E)}{\hbar nc} \tag{4.34b}$$

where $n$ is the refractive index of the material, defined above.

### 4.6.5 Tauc gap

Assuming a parabolic behavior [86]

$$\alpha\ E \sim (E - E_g)^2 \tag{4.35}$$

where $\alpha$ is the absorption coefficient and is related as (see eq. 4.34b)

$$\alpha \sim E\ \epsilon_2 \tag{4.36}$$

So

$$\begin{gathered}\alpha(E)\ E \sim (E - E_g)^2 \\ E\epsilon_2(E)E \sim (E - E_g)^2 \\ E^2\ \epsilon_2(E) \sim (E - E_g)^2 \\ E\sqrt{\epsilon_2(E)} \sim E - E_g\end{gathered}$$

In conclusion, the depentence between $E\sqrt{\epsilon_2}$ and $E - E_g$ is linear and if we plot them, we will get a straight line, which where it reaches the $x$-axis, it will be the energy gap, because $E\sqrt{\epsilon_2} = 0$ then $E - E_g = 0 \Leftrightarrow E = E_g$.

### 4.6.6 Urbach energy

In the energy range $E < E_g$ [4], we have the relation

$$\alpha(E) = \alpha_0 e^{(E-E_0)/E_U} \tag{4.37}$$

where $\alpha_0$, $E_0$ are constants and $E_U$ is the urbach energy.

We manipulate this expression as follows.

$$\alpha = \alpha_0 e^{(E-E_0)/E_U}$$
$$ln\alpha = ln(\alpha_0 e^{(E-E_0)/E_U})$$
$$ln\alpha = ln\alpha_0 + lne^{(E-E_0)/E_U}$$
$$ln\alpha = ln\alpha_0 + \frac{E-E_0}{E_U} lne$$
$$ln\alpha = ln\alpha_0 + \frac{E-E_0}{E_U}$$
$$ln\alpha = ln\alpha_0 + \frac{E}{E_U} - \frac{E_0}{E_U}$$
$$ln\alpha = \left(ln\alpha_0 - \frac{E_0}{E_U}\right) + \frac{E}{E_U}$$
$$ln\alpha = const + \frac{1}{E_U} E$$

Therefore $ln\alpha$ and $E$ have a linear relation, and the slope of the their line is equal to $1/E_U$.

Consequently

$$E_U = [\text{slope}(ln\alpha \text{vs} E)]^{-1} \tag{4.38}$$

# Chapter 5

# Microstructure of a-C

*Initially we study the structure and the microstructure of our networks which we derive from the two diferent tight-binding models. We check the distribution of the distances and angles between the atom bonds as well as the rings they form. We first thoroughlly confirm that our networks are reliable and in accord with what has been known and established in the literature by using different methodologies. Then in the following, we analyze the networks to extract and establish various physical trends.*

## 5.1 Structural parameters

We first begin with a description of the microstructure of a-C. This is a stringent test for the tight-binding model before its application to open questions and problems of amorphous and nanocomposite carbon. Intensive work over the years has led to a rather complete understanding of the structure of evaporated a-C (e-C) and the denser ta-C materials. Not so well understood is the structure of low-density a-C (with $\rho < 2$ gcm$^{-3}$), especially with regard to its connectivity and the presence or not of $sp^3$ bonding.

Representative examples of networks at various densities, produced by the liquid-quench method described before, are portrayed in Fig. 5.1. The structural details of these networks are tabulated in Table 5.1. Networks A – E and WWW have been constructed by using the enviroment-dependent tight-binding (EDTB) model [36]. We mostly use these samples throughout our analysis in this thesis. However, we have also made supplementary samples. These ones have been constructed by the hamiltonian of Mehl and Papaconstantopoulos (NRL model) [40, 41]. The structural details of the latter networks are tabulated in Table 5.2.

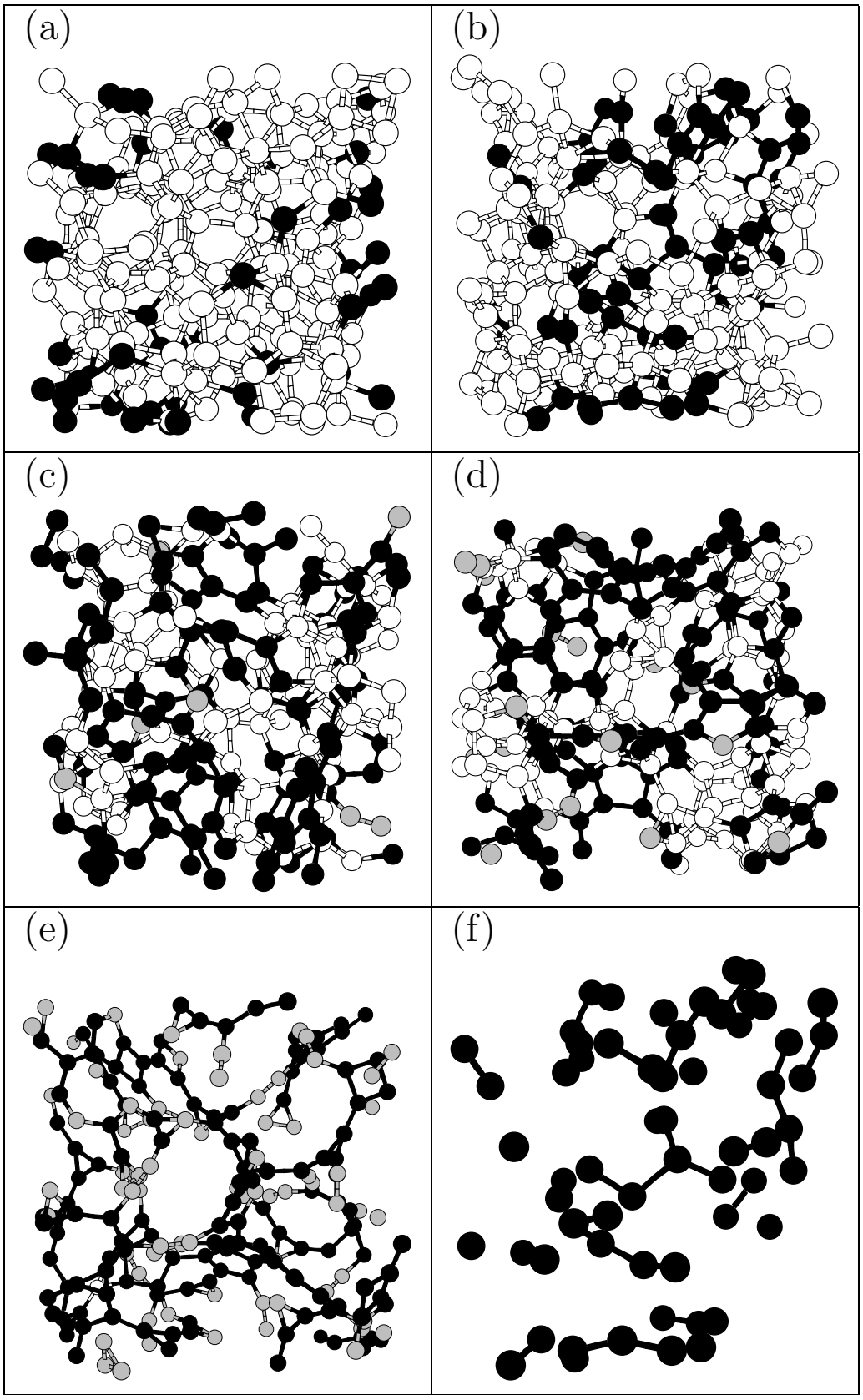


**Fig. 5.1**: Ball and stick models of the a-C structures included in Table 5.1. Panels (a)-(e) show networks A – E, respectively. Panel (f) displays the connectivity of $sp^2$ sites of network B. Open, dark, and shaded spheres denote $sp^3$, $sp^2$, and $sp^1$ sites, respectively.

**Table 5.1**: Density, coordination numbers, cutoff radius and hybrid contents of the a-C structures, whose network topologies are illustrated in Fig. 5.1. Also given for comparison are the corresponding structural parameters of diamond and of the WWW fully tetrahedral amorphous model [53]. $N_2^*$ would be the second coordination number without small rings.

| Sample | Diamond | WWW | A | B | C | D | E |
|---|---|---|---|---|---|---|---|
| $\rho$ (gr/cm$^3$) | 3.46 | 3.27 | 2.99 | 2.66 | 2.23 | 1.93 | 1.20 |
| $N_1$ | 4.00 | 4.00 | 3.80 | 3.73 | 3.43 | 3.28 | 2.65 |
| $N_2$ | 12.00 | 11.94 | 10.29 | 9.35 | 7.53 | 7.06 | 3.78 |
| $N_2^* = 6(N_1 - 2)$ | 12.00 | 12.00 | 10.80 | 10.38 | 8.58 | 7.68 | 3.90 |
| $r_c$ (Å) | 1.58 | 1.70 | 1.82 | 1.82 | 1.76 | 1.76 | 1.58 |
| $sp^3$ (%) | 100 | 100 | 79 | 72 | 45 | 36 | 1 |
| $sp^2$ (%) | 0 | 0 | 21 | 28 | 52 | 55 | 66 |
| $sp^1$ (%) | 0 | 0 | 0 | 0 | 3 | 9 | 33 |

**Table 5.2**: Density, coordination number, cutoff radius and hybrid contents of the a-C structures, using NRL model. Also given for comparison are the corresponding structural parameters of diamond and of the WWW fully tetrahedral amorphous model [53].

| Sample | Diamond | WWW | A' | B' | C' | D' |
|---|---|---|---|---|---|---|
| $\rho$ (gr/cm$^3$) | 3.65 | 3.44 | 3.05 | 2.85 | 2.51 | 1.60 |
| $N_1$ | 4.00 | 4.00 | 3.78 | 3.66 | 3.46 | 3.16 |
| $r_c$ (Å) | 1.52 | 1.88 | 1.82 | 1.78 | 1.76 | 1.72 |
| $sp^3$ (%) | 100 | 100 | 78 | 67 | 47 | 18 |
| $sp^2$ (%) | 0 | 0 | 22 | 32 | 52 | 77 |
| $sp^1$ (%) | 0 | 0 | 0 | 1 | 1 | 5 |

From the very first beginning, we 'd like to state that there is absolute similarity to the results of the two sets of networks. We observed that our results are independent of the hamiltonian. Therefore, we 'll refer to results of NRL model only when these are extremely important findings.

A close inspection of the ta-C networks in panels (a) and (b), with a clear predominance of tetrahedral bonding, reveals that the $sp^2$ sites are largely clustered, an effect well established from previous theoretical work [55, 56, 57, 58, 59]. This is clearly demonstrated in panel (f), where only the $sp^2$ sites of network B (72% $sp^3$ atoms) are shown. Clustering is present in the form of olefinic, chainlike geometries.

There are five pairs, seven three-membered chains, two four-membered chains, and three larger clusters: One seven-membered and two eight-membered chains. In the more dense network labeled A in panel (a), with 79% $sp^3$ sites, such large clusters do not exist. In agreement with the *ab initio* MD simulations of Marks *et al.* [59], the $sp^2$ chains are isolated and do not link (percolate) to a single spanning cluster.

The driving force behind the clustering effect is stress relief. Earlier simulations of Kelires, using the Tersoff, potential addressed the issue of local rigidity in ta-C [18]. Despite the shortcomings of the potential (insufficient clustering and the presence of isolated threefold sites in ta-C), the simulations were useful in pointing out that clustering contributes stress relief and rigidity to the network. This depends on the degree of clustering. The larger the cluster, the higher the stress relaxation and the contribution to rigidity in the network. Experimental work supported these conclusions [60, 61]. Panel (f) also shows that there still are some isolated threefold sites in the present TBMD computer-generated ta-C network. It is not yet clear if this is a shortcoming of the model or whether slower quenching rates will be able to eliminate the presence of these defects, which is only physical for much larger cells than the ones used here. Previous TB models which succesfully simulated the clustering effect in ta-C also suffer from this shortcoming [55, 56, 57], and only *ab initio* MD simulations [58, 59, 62] reported networks free of this type of defect.

The main characteristic of the low-density networks [panel (e)] is an open structure with long chains and large rings, and with numerous $sp^1$ sites (33%). A sizeable fraction of such sites is also present at densities typical of e-C, as in panel (d) (9%). In this density region, all three hybridizations are present in significant proportions. Although the presence of $sp^1$ hybrids in a-C has been supported by all types of computational work, it is not directly established by experiment. Instead, the latter probes the $sp^2$ or $sp^3$ hybrids. It is useful to determine the actual fraction of $sp^1$ sites in low-density a-C. Because $sp^1$ are usually mingled up with $sp^2$, this reflects on the reliable estimate of the $sp^3$ fraction.

## 5.2 Radial distribution function

The cutoff distance ($r_c$) (see Tables 5.1 & 5.2) used to define the coordinations in the networks is determined in each case from the first minimum in the pair distribution functions g(r), which are shown in Fig. 5.2. Thus, the cutoff might not be the same for every cell. As for any other similar analysis in the past, counting first nearest neighbors (NN) involves some degree of umbiguity. The choice of the cutoff distance should always take into account that first NN are those atoms forming a stable bond. So, we do not count atoms as neighbors if they are involved

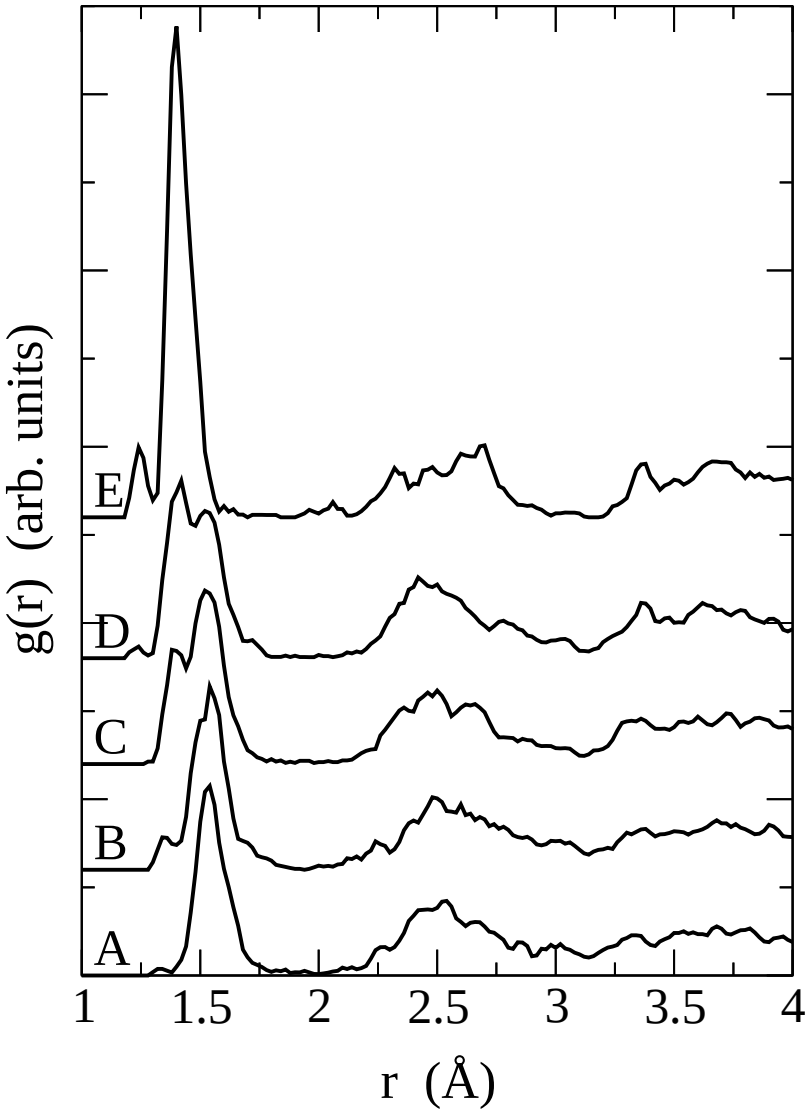


**Fig. 5.2**: The pair distribution functions, at 0 K, of networks A – E included in Table 5.1.

in extremely streched, weak, and easily breaking bonds, and the cutoff distance is determined accordingly.

The functions in Fig. 5.2 were calculated at 0 K to reveal the subtle features associated with each type of hybridization (these are usually smeared out at elevated T's.) It is interesting to analyze how these features evolve as we move from the dense ta-C structure of cell A to the open structure of cell E. Let us concentrate on the first peak in the g(r). In A, we have a single peak associated with the $sp^3$ bonds and only a slight shoulder in its left side indicates the presence of $sp^2$ atoms. This develops

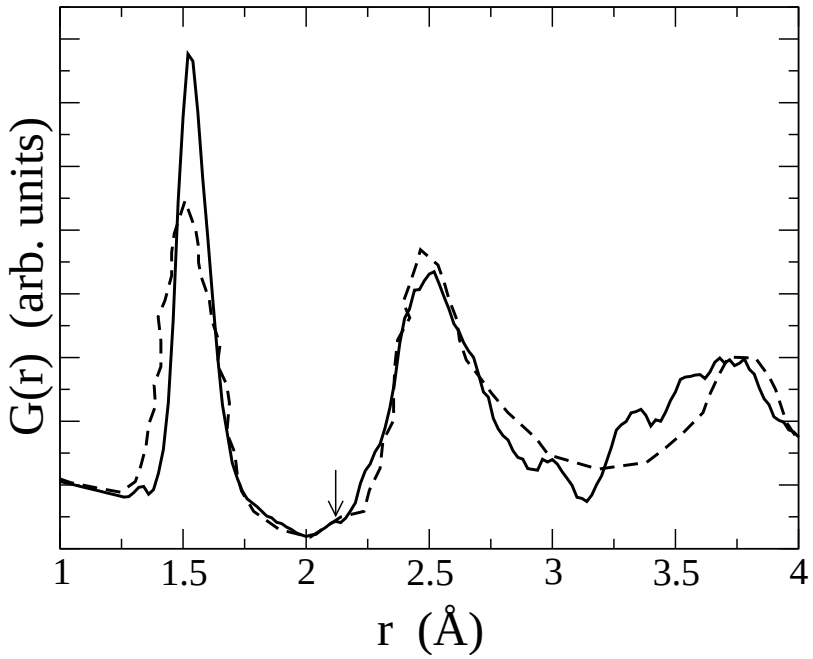


**Fig. 5.3**: The reduced radial distribution function, at 300 K, of network A (solid line), compared to the neutron-diffraction data (dashed line) of Gilkes *et al.* [63] Arrow shows the feature at 2.15 Å, indicative of four-membered rings.

into a small peak in structure B, at 1.34 Å, it grows substantially in structure C, at 1.36 Å, and becomes the main peak in D, at 1.40Å. On the other hand, the presence of $sp^1$ sites starts to show up clearly in D, at 1.22 Å, and develops into a well-defined peak in E, at 1.24 Å. Note also that the split of the first peak involves a shift of the sub-peak positions from cell to cell. For example, the $sp^2$ sub-peak position moves to larger values when going from A to D. This provides firm evidence that the $sp^2$ bonds are in a constrained environment in the dense network of ta-C, and that the length of the bond eventually requires its natural, graphitelike value in the less dense network of e-C. Similarly, the $sp^3$ bond length shifts from diamondlike values in ta-C to lower values in the intermediate mixed phase.

The simulated ta-C microstructures are in accord with experiment, as the comparison of the simulated (network A, $\rho = 3.0$ gcm$^{-3}$) and measured reduced radial distribution functions G(r) in Fig. 5.3 shows. The latter is derived from the neutron-diffraction data of Gilkes *et al.* [63] The agreement is good, especially regarding the relative height of the first two peaks, which is well reproduced. Note that the earlier Wang and Ho TB model [37], as well as the TB model of Frauenheim [55, 57], do not reproduce this correctly, since the simulated second peak of G(r) is higher than the first.

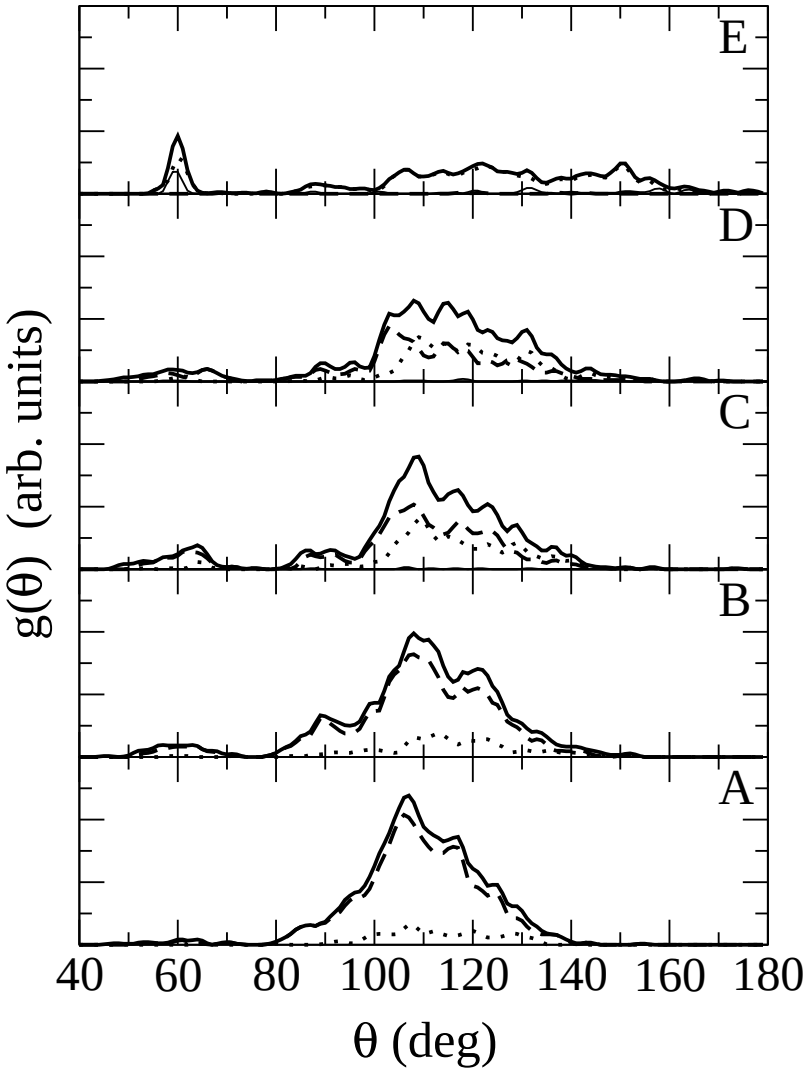


**Fig. 5.4**: Bond-angle distribution functions of networks A – E. Heavy solid, dashed, dotted, and light solid lines denote the total and $sp^3$, $sp^2$, and $sp^1$ contributions, respectively.

## 5.3 Bond-angle distribution function

The bond-angle distribution functions of the representative networks, analyzed in contributions from each hybridization, are shown in Fig. 5.4. They are quite broad, especially the $sp^2$ distributions in ta-C which are peaked at an angle of $\sim 110°$. This shows that the $sp^2$ geometries in ta-C are not planar and, consequently, are heavily stressed. Note also the peaks at 60° and 90° arising from three- and four-membered rings, respectively. It is clear that the major contribution to these peaks comes from

$sp^3$ atoms.

## 5.4 Ring statistics

An important result of the present simulations, regarding the microstructure of a-C, is the finding of three- and four-membered rings in ta-C networks. Fig. 5.5 shows related histograms for each of the representative cells discussed above, including the low-density ones. The shortest-path criterion of Franzblau [64] was used to define the ring sizes. As a reference, we also analyze and show the ring statistics for the WWW model, an idealized representative of "amorphous diamond". By construction [53], this network contains a small number of four-membered rings. It also contains five- and seven-membered rings, the former being more numerous. Of course, because the network is fully tetrahedral, six-membered rings are the most abundant.

The ta-C networks (cells A and B) contain a significant fraction of both three- and four-membered rings. Note that this is the first tight-binding model which predicts three-membered rings in ta-C. Previously, only the *ab initio* MD simulations of Marks *et al.* [59], using the Car-Parrinello method, predicted the existence of such rings. Neither the previous Wang and Ho two-center TB model [37] nor the TB model of Frauenheim [55, 57] found three-membered rings in ta-C. The relative fraction of five-, six-, and seven-membered rings is also in good agreement with the *ab initio* results, with the five-membered rings being slightly more numerous than the six-membered rings and significantly more numerous than the seven-membered ones.

Interestingly, we find small-membered rings not only in ta-C, but also in low-density networks, in cell E ($\rho = 1.2$ gcm$^{-3}$) for example. This is somewhat surprising. According to arguments of Marks *et al.* [59], small-membered rings have a high strain energy, as calculated from the heat of formation of organic elements such as cycloalkanes, but are stabilized in ta-C by its intrinsic compressive stress. Then, one should not expect such rings to exist in low-density networks which have a much lower stress. One answer to this paradox may be given by the theory of Kelires [17, 18, 19] who pointed out that stress in a-C can be *locally* quite large, even in a globally relaxed structure with average intrinsic stress zero. This will allow a locally strained cluster of atoms to form small rings.

Another explanation could be that such small rings do not necessarily have high strain energy in low-density networks, where the hybridization is not predominantly $sp^3$. (Note that the arguments about cycloalkanes are solely based on $sp^3$ geometries.) To investigate this possibility, carefull studies of local stress in a-C within TBMD are needed, but this goes beyond the scope of the present work. Still, some additional information can be extracted from a further analysis of the ring structures into

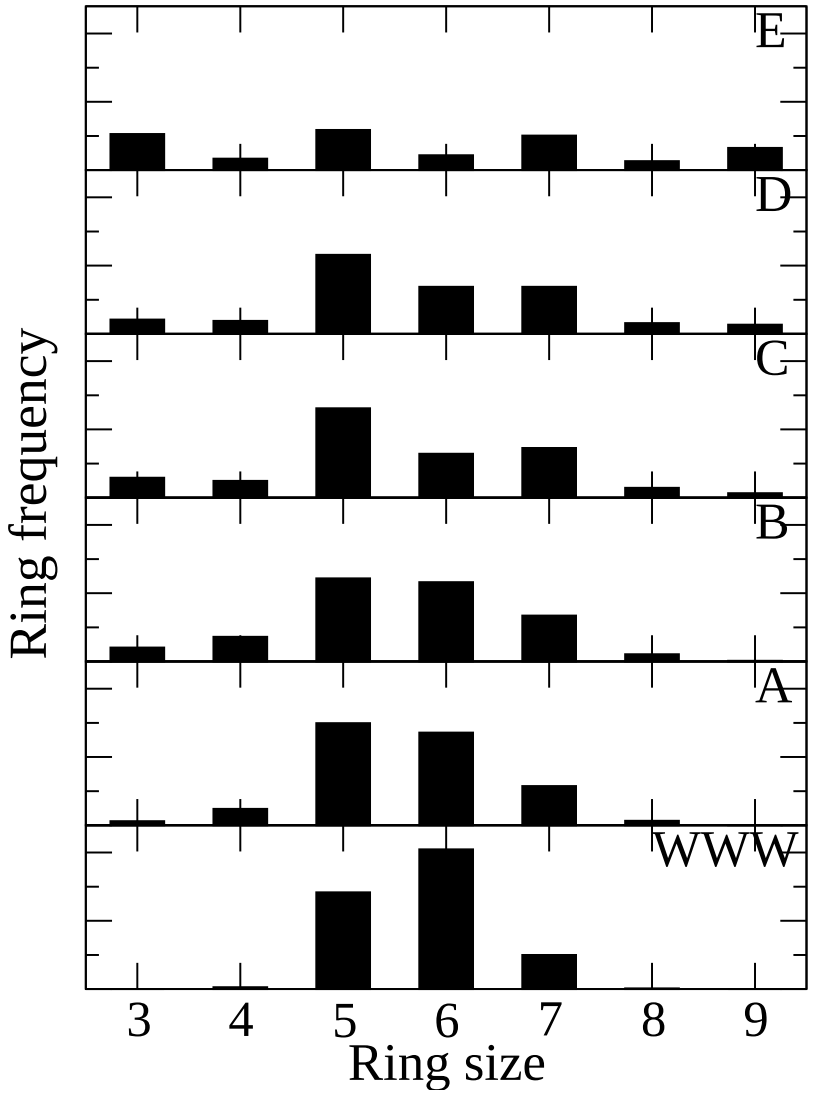


**Fig. 5.5**: Histograms showing the frequency of occurence of rings of various sizes in the WWW model, and in the structures A – E shown in Table 5.1 using EDTB model.

relative hybrid populations. This is given in Fig. 5.7. We see that indeed $sp^3$ hybrids constitute the vast majority of configurations in small rings (e.g., 100% in three- and nearly that in four-membered rings of network A). However, as the density decreases, the other hybrids also provide a sizeable contribution to the formation of small rings. This shows the complexity of the problem which differentiates it from the simple case of molecular cycloalkanes. Still, the $sp^3$ atoms overall dominate in small rings. (Except in structure E, but their total percentage is just 1%.) Another information coming out from this analysis, is that the $sp^3$ ($sp^2$) atoms have a higher

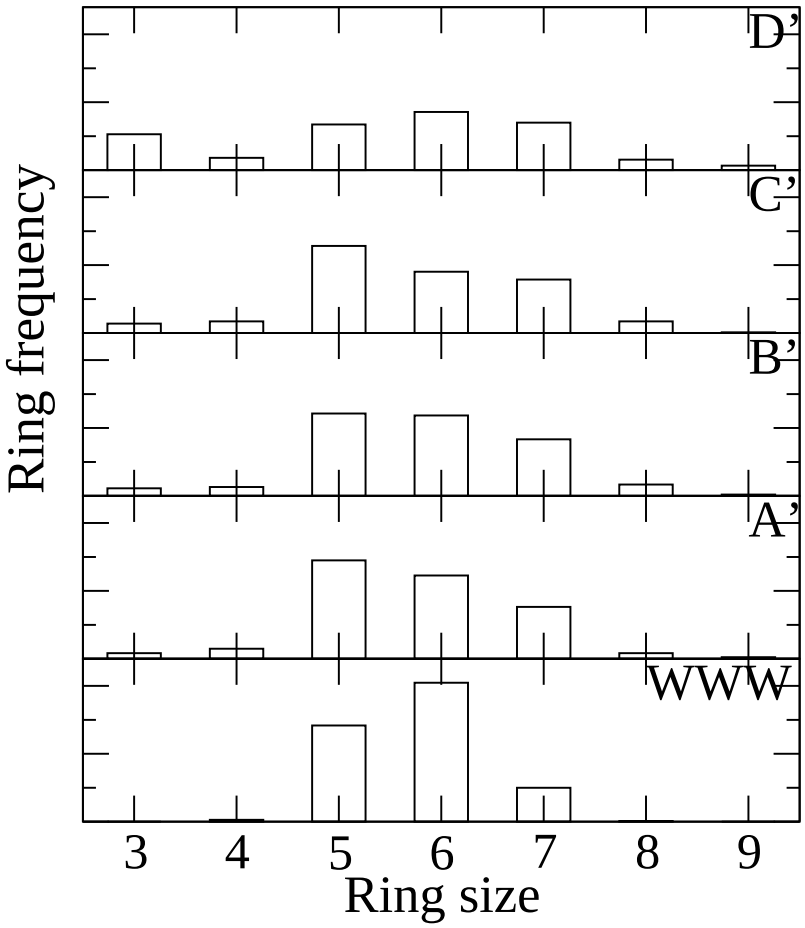


**Fig. 5.6**: Histograms showing the frequency of occurence of rings of various sizes in the WWW model, and in the structures A' – D' shown in Table 5.2 using NRL model.

relative participation in ring sizes less (larger) than six. (See for example network C having nearly equal fractions of these two hybrids.)

As pointed out by Marks *et al.* [59], the presence of four-membered rings explains the presence of a peak in the experimental [63] G(r) at 2.15 Å. Such a peak can only be generated by the diagonal distances across a quadrilateral. The simulated G(r) with the present model, shown in Fig. 5.3, clearly possesses this subtle feature, in excellent agreement with experiment and with the *ab initio* results. A related issue concerns the second-neighbor coordination number $N_2$ in ta-C, which was found by Gilkes *et al.* [63] to be less than expected. As explained by Marks *et al.* [59], the dicrepancy can be partly attributed to the presence of three- and four-membered rings, which effectively reduces $N_2$ with respect to the first NN number $N_1$. In a fully bonded network with a minimum ring size of 5, the two are related through the

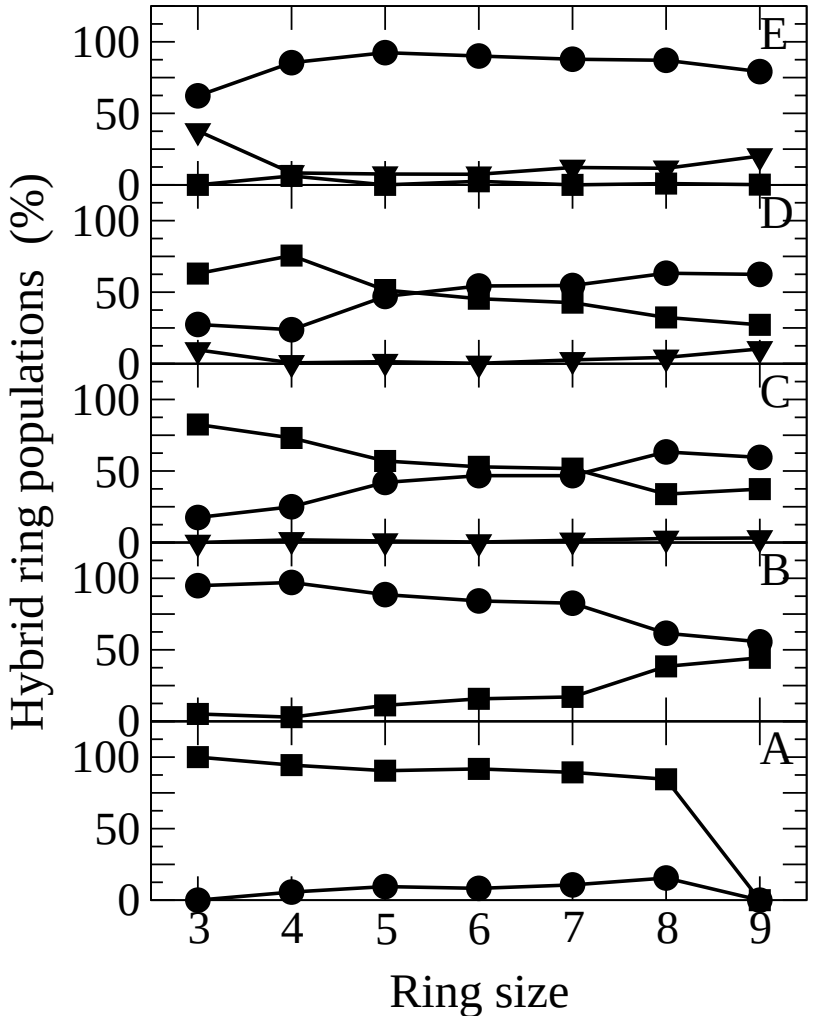


**Fig. 5.7**: Decomposition of ring populations in structures A – E into different hybridizations. Squares, circles, and triangles denote $sp^3$, $sp^2$, and $sp^1$ sites, respectively. Lines are guide to the eye.

expression $N_2 = 6(N_1 - 2)$ [59]. Our calculated coordination numbers are given in Table 5.1 [$N_2$ is extracted from a Gaussian deconvolution of the second peak of the g(r)], and clearly show the reduction of $N_2$ due to small rings.

We followed the same procedure with the NRL model too. Our results were the same as the previous ones and they are presented in the corresponding histograms in Fig. 5.6. We found three- and four-membered rings at ta-C networks (cells A' and B'). We have also noticed the existence of small-membered rings in low-density networks (cell D').

## 5.5 Conclusions

We first showed the accuracy and transferability of the model by analyzing in detail the structure of a-C networks, and comparing to experimental and first-principles results.

More than that, the most important finding of this study of amorphous carbon networks' microstructure is the existence of three- and four-membered rings. This was shown by the straight calculation of the rings, which the bonds of the atoms form. Both our models confirm the previous result, which has only been found by *ab-initio* calculations.

Beyond this proof of the small-membered rings' existence, we checked this in other ways too. The presence of four-membered rings is confirmed by a small peak at the $G(r)$. There are also further evidence on that, based on the calculation of the second neighbors. We found less of the latters than a theory predicted, which, however, hadn't taken into account small-membered rings. Finally, the peaks of $g(\theta)$ at $60^\circ$ and $90^\circ$ show along with the previous the presence of three- and four-membered rings.

# Chapter 6

# Physical Trends in a-C

*In this chapter, we trace important physical trends in amorphous carbon using the networks whose microstructure was presented in the previous chapter. We first show that between the density of the networks and their $sp^3$ fraction a linear relationship holds. Then, we derive a power-law behaviour of the the bulk modulus as a function of the coordination, and confirm that this is in accord with the well known constraint-counting theory of Philips and Thorpe. We also derive power-law relations between the bulk modulus and the homopolar gap of the material.*

## 6.1 Density Variation

Having established the reliability of the TB models in describing the microstructure of a-C, we now turn our attention to certain issues which are still unclear. One of them is the variation of $sp^3$ fraction or, equivalently, of mean coordination $\bar{z}$ $(= N_1)$, with density. The basic question underlying this issue is whether there is a linear relationship between these two quantities. Of course, if such linear variation exists, it has to be limited within *physically meaningful densities*.

We have carried an extensive investigation of this issue through the entire range of densities relevant to a-C. The physically meaningful densities are bounded from below by the density at the floppy transition and from above by the diamond density. The former signifies the transition from rigid to floppy behavior. According to the constraint counting theory of Philips [65] and Thorpe [66], the transition is located at $\bar{z}$=2.4. Below this, the network is unconstrained, i.e., there are many ways to deform the network at no cost in energy. These independent deformations are called zero-frequency modes. Above $\bar{z}$, the network is constrained and rigid. The problem

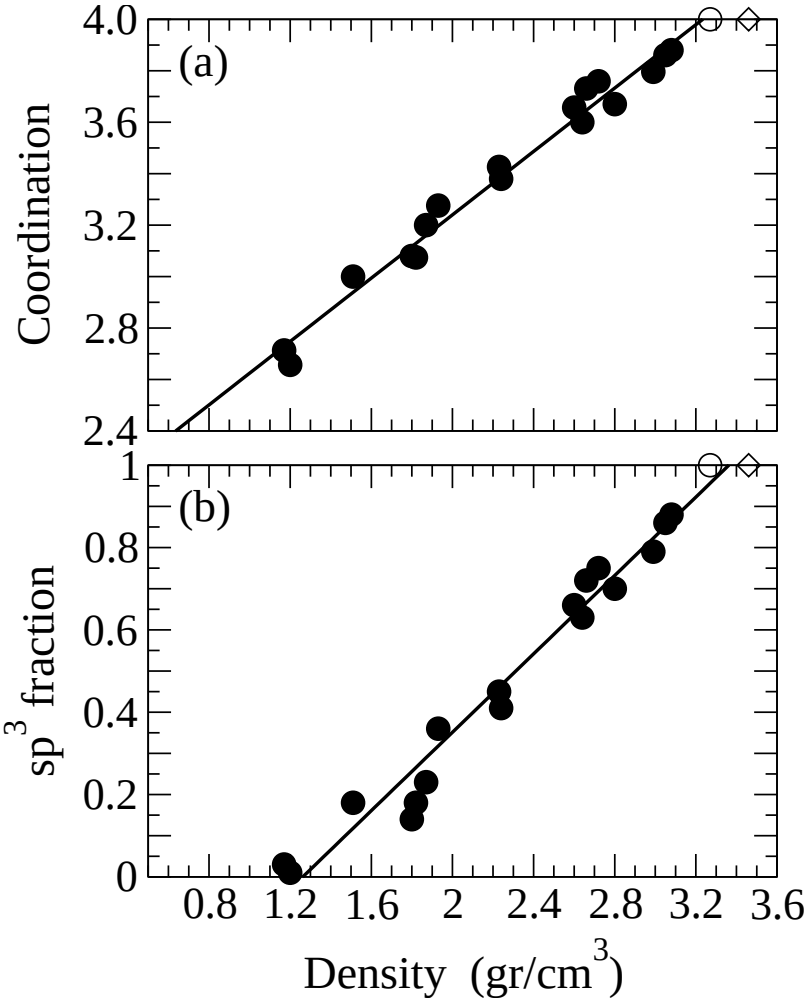


**Fig. 6.1**: The variations of (a) mean coordination and (b) $sp^3$ fraction as a function of density in a-C networks (filled circles) using EDTB model. Lines are linear fits to the points. Also given are the corresponding calculated quantities for the WWW model (open circle) and diamond (open diamond).

is that the density corresponding to the floppy transition in a-C is not actually known with any accuracy. The other end of the density spectrum, the diamond density, is of course unambiguous and fixed for experiment at 3.51 gcm$^{-3}$ but, for theory, it may vary from method to method.

Fig. 6.1 shows our results regarding the variation of $\bar{z}$ and $sp^3$ fraction as the density of the network varies. In total, we have generated seventeen networks, besides the WWW network relaxed with the present EDTB model, to have as much statistics as possible. Several interesting conclusions derive from this analysis. The foremost important one is that the variations are linear beyond any doubt, from down the

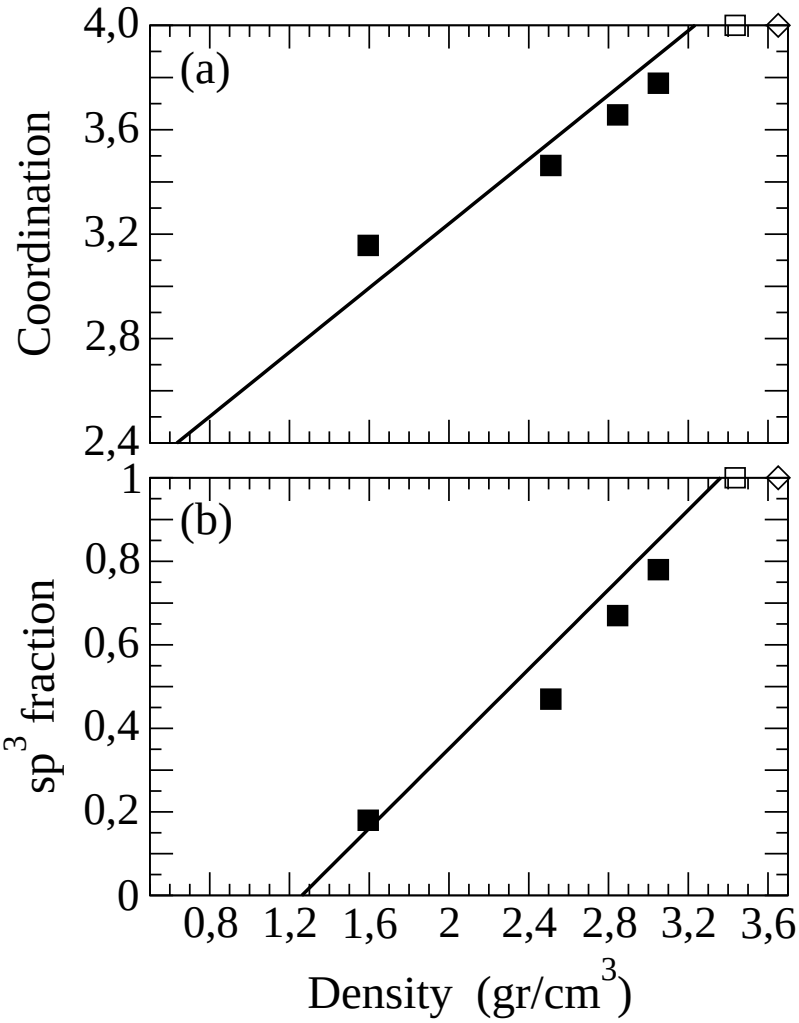


**Fig. 6.2**: The variations of (a) mean coordination and (b) $sp^3$ fraction as a function of density in a-C networks (filled squares) using NRL model. Lines are linear fits to the points of Fig. 6.1. Also given are the corresponding calculated quantities for the WWW model (open square) and diamond (open diamond).

floppy transition up to the diamond density. A linear fit of the density-versus-coordination points in panel (a) gives

$$\rho(\mathrm{g/cm^3}) = -3.29 + 1.65\ \bar{z}. \tag{6.1}$$

Equation (6.1) gives a density of $\sim 0.67$ gcm$^{-3}$ at the floppy transition ($\bar{z}$=2.4). We thus predict that for an a-C network to be rigid, its density needs to be larger than this value. At the other end, this equation predicts a density of 3.31 gcm$^{-3}$ for $\bar{z}$=4, slightly more than the calculated density of 3.27 gcm$^{-3}$ for the WWW model. We

thus impose an upper limit in the range of densities of a-C. This is the density of the hypothetical, fully tetrahedral "amorphous diamond". Note that this density is lower, as it should be, than that of diamond (3.46 gcm$^{-3}$ with the present model) by about 4%. This confirms a similar conclusion reached earlier [17, 18, 19] using the simpler Tersoff potential. The other group-IV covalent materials, Si and Ge, show this trend and there is no reason why the all-$sp^3$ C network should behave differently.

The linear fit of the density-versus-$sp^3$ fraction points in panel (b) gives

$$\rho(\mathrm{g/cm^3}) = 1.27 + 2.08\ (\mathrm{sp^3 fraction}). \tag{6.2}$$

Eq. (6.2) predicts the minimum density required to sustain $sp^3$ bonding in a-C to be $\sim$ 1.3 gcm$^{-3}$. The $sp^3$ sites are needed in such low-density networks as linking geometries between the main $sp^2$ and $sp^1$ components. For 100% $sp^3$ bonding, the corresponding density is 3.35 gcm$^{-3}$, a bit higher than the WWW density and the value obtained from the fit of Eq. (6.1), but still less than diamond's by $\sim$ 3%. Despite the slight difference between the two fits (the end points were in both not fixed), the conclusion about an upper limit in the possible densities of ta-C is firmly established. Let us point out that the highest densities for ta-C reported until now by experiment are less than 3.3 gcm$^{-3}$. It is possible that this natural limit can not be exceeded.

Fig. 6.2 shows our NRL results of the variation of $\bar{z}$ and $sp^3$ fraction as a function of density. Furthermore, in order to compare the two models, we have also drawn the straight lines of equations 6.1 and 6.2. In addition, we present the density of WWW network and diamond by using the current model. These points are very close to the previous linear fits. But the densities of WWW and diamond are slightly higher than the EDTB results. However, they are an upper limit in densities of a-C.

Comparison of our results with experimental data can be made on the basis of $sp^3$ fraction. (Experiment directly probes the $sp^3$ fraction, not $\bar{z}$. The latter follows indirectly. This is exact for dense networks, but not so for low-density ones containing $sp^1$ sites.) Fig. 6.3(a) compares our extracted linear variation, given by Eq. (6.2), to various sets of experimental data from non-hydrogenated a-C, wide as possible to cover a larger density region. A large set consists of data extracted from samples prepared by filtered cathodic vacuum arc (FCVA) deposition [67, 68]. Another large set consists of data extracted from samples prepared by magnetron sputtering (MS) [69]. Also shown is the $sp^3$ fraction of a na-C film prepared by cluster-beam deposition [13]. The density and $sp^3$ content of this film were analyzed by Ferrari *et al.* [68] and reported to be 1.4 gcm$^{-3}$ and $\sim$ 10%, respectively. X-ray reflectivity (XRR) was used for the determination of the density of the FCVA and na-C films, and electron energy-loss spectroscopy (EELS) for their $sp^3$ fraction. The

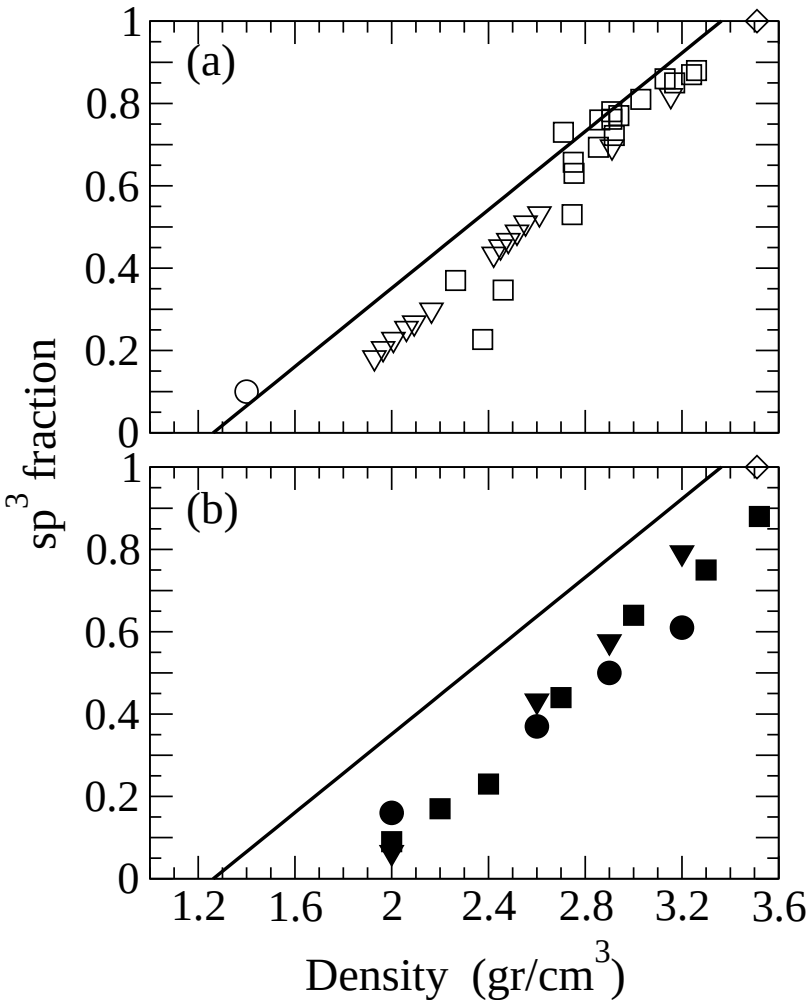


**Fig. 6.3**: Comparison of our fitted linear variation (see line of Fig. 6.1b) of $sp^3$ fraction as a function of density (solid line) with (a) experimental data and (b) other theoretical results. In (a), squares denote FCVA data [67, 68], triangles show MS data [69], and the circle denotes the $sp^3$ fraction in a na-C film [13, 68]. In (b) squares denote NOTB results,[56] triangles show CPMD results [62], and circles denote EDIP results [70]. In both (a) and (b), the experimental density of diamond (filled diamond) is given for comparison.

density of the MS films was determined by EELS and Rutherford backscattering spectroscopy (RBS), and the $sp^3$ fraction by EELS.

The comparison shows very good agreement between theory and experiment in the ta-C region. A tendency for a slight overestimation of the $sp^3$ fraction by theory is observed. In this region, all experimental data fall closely to each other. It is not so at lower densities, where the FCVA data show a rather large dispersion, and deviate from the MS data. In this region, if we exclude the single point from the cluster-

assembled film which falls very close to the theoretical line, a larger overestimation seems to exist. It is not clear at the moment if this is attributed to inaccuracies in the EDTB model. However, let us underline a fundamental principle: if a linear variation indeed exists, it has to be valid over the whole range of possible densities for a-C, and not selectively over a limited range. Consequently, a global linear fit has to be applied to the experimental points. Unfortunately, this is hard to envision if we consider them all together. If considered individually, a linear fit can be drawn over each set, but needs to be extrapolated to get the limiting values.

Actually, a linear fit over the FCVA data was carried out and reported by Ferrari *et al.* [68] to yield $\rho$ (g/cm$^3$) = 1.92 + 1.37 ($sp^3$ fraction). This gives a density of $\sim$ 3.3 gcm$^{-3}$ for 100% $sp^3$ content, in good agreement with our limiting value, but the lower limit at 1.92 gcm$^{-3}$ is considerably higher than ours. This means that if we consider the FCVA data alone, one predicts absence of $sp^3$ hybrids in a-C networks with densities less than this value. Then, a significant part of the MS data fall outside this variation and, in addition, it is hard to explain the discrepancy with the cluster-assembled amorphous carbon film. There are four possible, but contrasting to each other, explanations for this discrepancy: (a) The EELS measurement for the $sp^3$ content in this film is inaccurate. (b) A linear variation over the entire density region does not exist. (c) The cluster-assembled film can not be considered as belonging in the class of a-C materials, and so it is not necessary to satisfy a linear rule obeyed by the "more traditional" a-C films. (d) A linear fit *does exist*, but only after including in the fit all sets of experimental data, *albeit* with a large dispersion of points in the low-density regime.

The fact that our simulational data for both $\bar{z}$ and $sp^3$ content vary quite linearly with density over the entire regime, renders point (b) not so possible. Regarding point (c), it is clear from the work of Barborini *et al.* [13] that the cluster-assembled film *is amorphous*. It was produced by the deposition of small clusters which leads, according to these authors, to a disordered amorphous structure with a clear majority of $sp^2$ atoms and a sizeable $sp^1$ component. Its network should be similar to our simulated network shown in Fig. 5.1(e). Therefore, the most conceivable scenario is a combination of points (a) and (d), i.e., the $sp^3$ content of the cluster-assembled film could be probably overestimated, and one has to take into account all sets of data. In fact, if we consider together the MS data and the FCVA data of the ta-C region, a linear fit can be easily drawn. Extrapolation gives an upper limit of $\sim$ 3.4 gcm$^{-3}$ at 100% $sp^3$ content, and a lower limit of $\sim$ 1.6 gcm$^{-3}$ for 0% $sp^3$ fraction. This is closer but still higher than our prediction and excludes the cluster-assembled film. Obviously, more experimental work to characterize low-density films with a sizeable carbyne nature is needed.

Of course, one might argue that it is not possible to have a global fit of all experimental data, because they are produced by different deposition methods and thus different conditions and driving forces. This implies, accepting that the characterization tools for density and $sp^3$ fraction are reliable, that we could have films deposited with different methods having *the same density but not* $sp^3$ *fraction*. This is something difficult to envision because the density is solely determined by the fraction and type of hybrids involved and how they are linked. Thus, similar microstructures should yield similar densities and *vice versa*. It is more possible that any differences in the experimental data arise from uncertainties in the characterization analyses.

An independent confirmation of our $sp^3$ fractions is provided by the calculations of Haerle *et al.,* [38] who prepared a-C networks in the density range 1.8 - 3.0 gcm$^{-3}$ using the present EDTB model, and further relaxed them with a first-principles molecular-dynamics scheme within the pseudopotential plane-wave approach. Although they used smaller cells (64- and 128-atom networks), their $sp^3$ contents are quite close to our values. However, these authors did not consider lower densities and did not address the issues studied here, such as the variations with density and the conclusions resulting from them. They, instead, focused on the carbon 1$s$ core-level shifts. It is interesting that their EDTB cells proved to be quite stable under the first-principles relaxation, and only minor readjustments of atomic positions and changes of coordination were reported.

Comparison of our predicted variation of $sp^3$ fraction, Eq. (6.2), to previous theoretical results is done in Fig. 6.3(b). The latter are limited to the density region over 2.0 gcm$^{-3}$. Included in this figure, are data from the non-orthogonal tight-binding (NOTB) MD simulations of Stephan *et al.* [56], the Car-Parrinello MD (CPMD) simulations of McCulloch *et al.* [62], and the classical MD simulations of Marks [70], who extended the environment-dependent interatomic potential (EDIP) of Bazant and Kaxiras [71] to carbon. The common characteristic of these results is a consistently lower $sp^3$ fraction compared to our global fit, and also compared to the experimental data in panel(a).

For the purposes of the present analysis, the most important issue is to examine whether these theoretical data provide also a solid confirmation for a linear behavior, and if the variation is limited within physically meaningful densities. Regarding the first point, note that none of these works attempted to fit the reported points, but from the visual inspection it seems that such a linear variation can be drawn. A linear fit to the CPMD data, considered to be the most accurate set, gives at 100% $sp^3$ content, which would correspond to an "amorphous diamond" network, a limiting value of $\sim$ 3.55 gcm$^{-3}$. NOTB gives 3.74 gcm$^{-3}$, and EDIP gives 4.24 gcm$^{-3}$. Unfortunately, none of these works reported the *relaxed density of crystalline*

*diamond* within the respective methodology, in order to judge whether these values are or not *physically meaningful*. For similar technical details in the CPMD method (pseudopotentials and kinetic energy cutoffs), Galli *et al.* [72] calculated the density of diamond to be $\sim$ 3.3 - 3.35 gcm$^{-3}$. Thus, the McCulloch data seem to suggest, assuming they can be fitted linearly, that the "amorphous diamond" network would have a density higher than diamond. That would be incorrect. Similarly, NOTB and especially EDIP seem to predict that the amorphous analog is denser than the crystal. It could be that EDIP gives an equilibrium diamond density larger than 4.24 gcm$^{-3}$. This is already 20% higher than the experimental value, quite erroneous for an empirical model introduced to describe correctly $\pi$ interactions in a-C.

## 6.2 Bulk Modulus

### 6.2.1 Bulk modulus versus Coordination

We now address another interesting physical trend in a-C, namely the variation of elastic moduli as a function of mean coordination. The aim is to develop simple formulas able to predict the hardness and related properties for any given network, over the entire range of densities. There is practical interest in this, since it overcomes the need to perform tedious first-principles calculations for a wide class of configurations, and it can guide and interpret relevant experiments, as well.

There is fundamental interest too. As mentioned above, Philips [65] and Thorpe [66] suggested, using a constraint-counting model, that within mean-field theory the elastic properties of random covalent networks depend primarily on a single variable, $\bar{z}$, the mean atomic coordination. Constraint-counting predicts a transition from rigid to floppy behavior at a critical coordination $\bar{z}_f = 2.4$. Furthermore, He and Thorpe [73] found, using the Keating potential, [52] that the elastic moduli of bond-depleted crystalline diamond lattices follow a power-law behavior $c \sim (\bar{z} - \bar{z}_f)^\nu$ within the range $\bar{z}_f < \bar{z} < 3.2$, with the exponent taking the value $1.5 \pm 0.2$. Franzblau and Tersoff [74] proposed, based on bond depleted crystalline diamond lattices and the Keating model, that this law is valid for the bulk modulus over the whole range $\bar{z}_f < \bar{z} < 4$. Bond-depleted "amorphous diamond" networks (WWW model) also showed the same behavior when simulated with the Keating model [75].

Model a-C networks can not just be generated by bond depletion of the WWW model without extensive reconstruction and rebonding. It is crucial to examine whether more realistic a-C networks can be described by the constraint-counting model, and if their moduli exhibit a power-law behavior, using a more sophisticated potential than Keating. Previous attemps [20] using the Tersoff potential found that

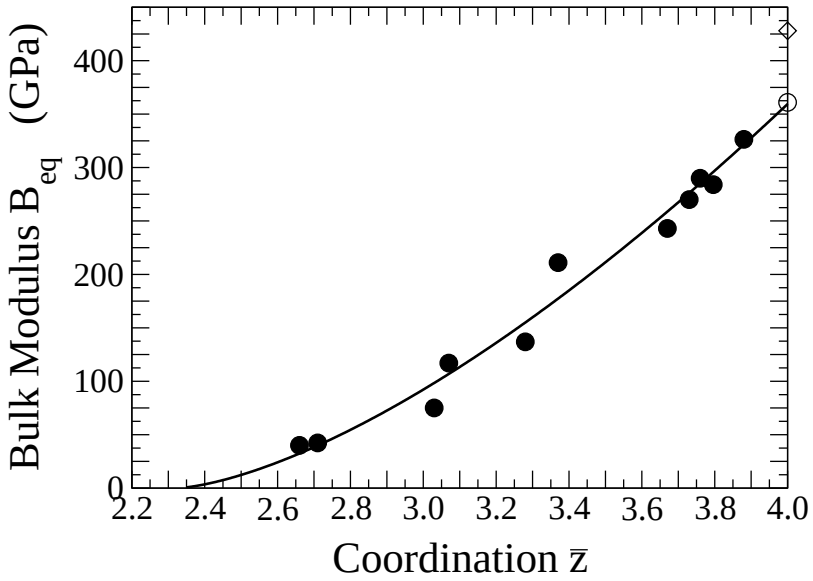


**Fig. 6.4**: The variation of computed bulk moduli (filled circles) of a-C networks as a function of the mean coordination $\bar{z}$. The open symbols, circle and diamond, are for the WWW model and diamond, respectively.

the bulk modulus indeed vanishes at $\bar{z}_f = 2.4$, and that the power-law is obeyed in the range $\bar{z}_f < \bar{z} < 2.8$, but strong deviations occur for higher coordinations. It is now clear that this is due to the too compact networks with excessive moduli produced by the Tersoff potential in this range. We thus reexamine here the issue using the accurate EDTB model.

We carried out extensive investigations using as a representative quantity the equilibrium bulk modulus $B_{eq}$. Our results for $B_{eq}$ for several networks as a function of $\bar{z}$ are given in Fig. 6.4. We also included in this figure the computed $B_{eq}$ for diamond (428 GPa) and for the WWW model (361 GPa). The latter value coincides with that calculated previously with the Tersoff potential for WWW [17, 18, 20]. This is neither surprising nor accidental because the Tersoff potential treats highly tetrahedral networks well. To extract the physical trend and get the details, we fit the computed data to the power-law relation

$$B_{eq} = B_0 \left( \frac{\bar{z} - \bar{z}_f}{\bar{z}_0 - \bar{z}_f} \right)^{\nu}, \tag{6.3}$$

where $B_0$ is the bulk modulus of the fully tetrahedral network, for which $\bar{z}_0 = 4.0$. This is not crystalline diamond but its amorphous counterpart. Letting all fitting parameters in Eq. (6.3) free, we obtain $B_0 = 361$ GPa, which is exactly the computed value for WWW, $\bar{z}_f = 2.25$, and $\nu = 1.6$. If we fix $\nu$ to be 1.5, we get 2.33 for $\bar{z}_f$, and

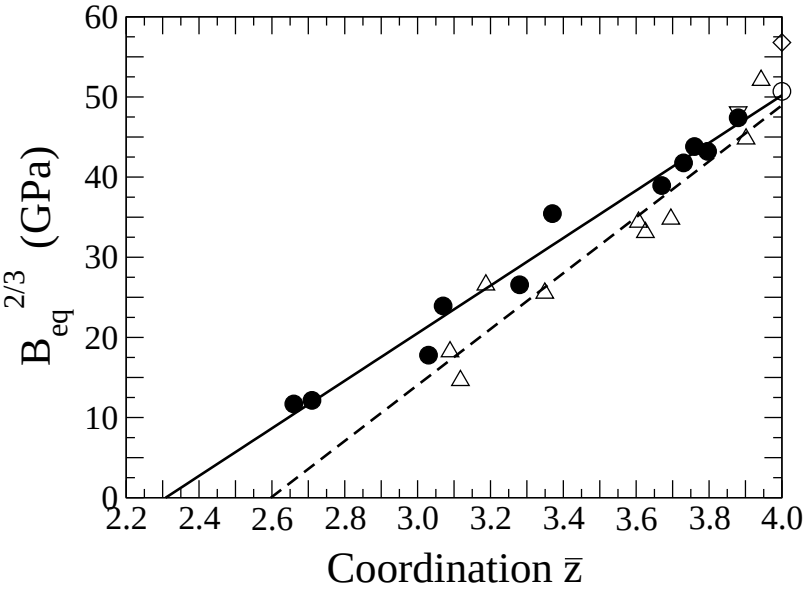


**Fig. 6.5**: Comparison of our computed bulk moduli with experimental data derived from surface acoustic waves [76] (open triangles) and surface Brillouin scattering [77] (open inverted triangle). Also shown are the bulk moduli of the WWW model and diamond (open circle and diamond, respectively).

if we fix $\bar{z}_f$ to be 2.4, we get 1.4 for $\nu$. We thus conclude that the variation confirms the constraint-counting theory of Philips and Thorpe, with a critical coordination close to 2.4, and it has a power-law behavior with a scaling exponent $\nu = 1.5 \pm 0.1$. In the following, for consistency, we shall be using $\nu = 1.5$, so the modulus obeys the relation

$$B_{eq} = 167.3\ (\bar{z} - 2.33)^{1.5}. \tag{6.4}$$

Our theory also predicts that "amorphous diamond" has a modulus less than diamond's by $\sim 10\%$ (softening effect.)

Comparison of our variation, as fitted with Eq. (6.4), to experimental moduli derived from surface acoustic waves [76] (SAW) and surface Brillouin scattering [77] (SBS) measurements is shown in Fig. 6.5. The agreement is very good, especially in the ta-C region. The computed modulus for $\bar{z} \simeq 3.9$ nearly coincides with the SBS data. The fit to the experimental data extrapolates to a modulus very close to that of the WWW model at $\bar{z} = 4$. A deviation seems to exist at lower coordinations. The theoretical fit is closer to the constraint-counting model than the experimental fit, which extrapolates to $\bar{z}_f = 2.6$. More experimental data at the low-$\bar{z}$ region are needed.

### 6.2.2 Bulk modulus and Homopolar gap

The calculated bulk moduli can also be linked with another interesting trend in a-C. This trend is closely related to a model proposed in 1985 by Cohen [78] for the bulk moduli of diamond and zinc-blende crystalline solids, and which was later modified to allow for deviations from tetrahedral coordination [79]. The essence of this model is embodied in a simple expression which defines a power-law dependence of $B_{eq}$ on the first NN separation $d$. It has the form

$$B_{eq} = A\ d^{-3.5}, \tag{6.5}$$

$A$ being a numerical constant. For non-tetrahedral crystals the expression takes the form

$$B_{eq} = C\ \frac{\bar{z}}{4}\ d^{-3.5}, \tag{6.6}$$

$\bar{z}$ being the average atomic coordination. The physical considerations behind this approach is that $B_{eq}$ depends predominantly on the covalent character of the bond, which is exemplified by a *homopolar gap* $E_h$, and only weakly on ionicity, and that $E_h$ scales logarithmically against lattice constants between different rows of the periodic table, as suggested by Philips [80].

In 1997, Kelires [81] proposed that a similar power-law behavior, with the same scaling exponent, also holds for the whole composition range of complex semiconductor alloys, such as $Si_{1-x}C_x$. The power law has the form

$$B_{eq} = A\ d(x)^n, \tag{6.7}$$

with $n$ = –3.5. This is a generalization of Cohen's theory where $B_{eq}$ scales with $d$ between different rows of the periodic table. In Kelires's model, $B_{eq}$ scales with $d(x)$ which is a function of composition $x$ within a single alloy series, and denotes an average bond length in the alloy. It is obvious that such simple expressions are very useful in extracting elastic data for any alloy composition, without the need to perform costly calculations.

It is quite interesting to examine whether such a power-law behavior is not restricted to only crystalline elements, compounds and alloys, but it could hold for amorphous materials as well. Amorphous carbon is ideally suited for this, because it displays a continuous sequence of microstructures with different density and coordination, contrary to a-Si and a-Ge having a unique tetrahedral network. In this respect, we seek to find trends in the spirit of Kelires's model, i.e., treating a-C as an "alloy", where the concept of composition is replaced by the concept of density. Since the latter is the fundamental quantity on which all trends discussed in this paper are based, it is proper to consider an average NN separation $\bar{d}$ which reflects the density and the topology of the network.

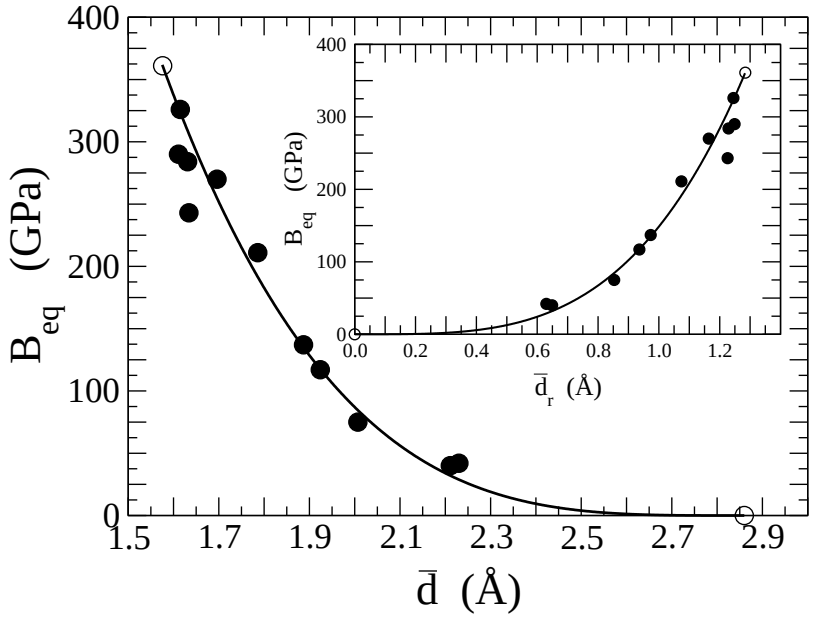


**Fig. 6.6**: Variation of bulk moduli with the average effective distance $\bar{d}$ (main figure), and the relative distance $\bar{d}_r$ (inset). For definitions see text. Open circles denote the extrapolated end points, for the fully tetrahedral amorphous network and the network at the floppy transition (by definition equals zero).

This is achieved by deriving an effective $\bar{d}$ directly from the volume and the "lattice constant" $a_0$ of the network. We are dealing with cubic cells, so a convenient choice is $\bar{d} = a_0\ \sqrt{3}/4$. As $\bar{d}$ shrinks, the network becomes stiff and dense. As it expands, the network becomes soft and dilute. Thus, small $\bar{d}$'s denote constrained ta-C networks, while large $\bar{d}$'s reflect the open, polymericlike structure of low-density networks, which can be subjected to excessive deformations. Note that choosing as $\bar{d}$ the average bond length derived from the g(r) is improper: As we move from $sp^3$- to $sp^2$- and eventually to $sp^1$-rich networks, the actual average bond length *shrinks* because the shorter $sp^2$ and $sp^1$ bonds dominate. On the other hand, the volume of the network increases (structures with more open space) and its stiffness decreases. This is opposite to the trend in tetrahedral semiconductors, where $B_{eq}$ scales inversely proportional to $d$ between rows of the periodic table. In other words, the choice to get $\bar{d}$ from the g(r) neglects the "volume effect" in a-C.

The dependence of $B_{eq}$ on the effective $\bar{d}$ is shown in Fig. 6.6. $B_{eq}$ decreases as $\bar{d}$ increases. In searching for a power-law behavior in this trend, we must take into account that the variation is bounded both from below at the floppy transition and from above at the density of the amorphous tetrahedral network. So, included in the plot is the point ($B_{eq} = 0$, $\bar{d}_f = 2.86$ Å) corresponding to the density at $\bar{z}_f =$

2.33 [Eq. (6.1) yields $\rho_f = 0.55$ gcm$^{-3}$, from which $\bar{d}_f$ is calculated], and the point corresponding to the density at $\bar{z}_0$. It is obvious that a fit using simple expressions of the type in Eqs. (6.5-6.7) is not possible, because neither $\bar{d}$ can be infinitely large nor $\bar{z}$ can be zero to yield a vanishing $B_{eq}$. Of course, the variation can be described with such power-law expressions by adding a constant, but unfortunately this obscurs the identification of a scaling exponent.

Therefore, we develop a model which can describe in a simple way the variation, making the power-law behavior transparent, and which can also be linked to the power-law model of Thorpe. This is obtained by fitting the variation to the expression

$$B_{eq} = A\ (\bar{d}_f - \bar{d})^n, \tag{6.8}$$

in analogy with Eq. (6.4). This ensures that $B_{eq}$ vanishes at $\bar{d}_f$ (= 2.86 Å), as the fit to the points clearly shows. Remarkably, the scaling exponent comes out to be $n = 3.5 \pm 0.05$, same in magnitude as in Cohen's and Kelires's models for the crystalline semiconductor compounds. The positive sign results because $B_{eq}$ scales proportional to the always positive relative distance $\bar{d}_r = \bar{d}_f - \bar{d}$. (The corresponding variation is shown in the inset of Fig. 6.6.) The constant $A$ in Eq. (6.8) equals 150.5 when $n = 3.5$, so in the following we shall be using the relation

$$B_{eq} = 150.5\ (2.86 - \bar{d})^{3.5}, \tag{6.9}$$

where $B_{eq}$ is measured in GPa and $\bar{d}$ in Å.

The observation of this accurate power-law behavior is quite notable for several reasons: (a) The magnitude of the scaling exponent is the same with the one derived for the crystalline tetrahedral case, indicating that the physical origins of the material's stiffness remain the same (see below), despite the change in the network topology (disorder due to amorphicity and non-tetrahedral configurations.) (b) The model is completely analogous to Kelires's model for crystalline semiconductor alloys, i.e., the power-law behavior holds for the whole density range of these complex a-C networks. $B_{eq}$ scales with $\bar{d}$, which is a function of density, within a series of networks composed of the same element. This is different from Cohen's model where $B_{eq}$ scales with $d$ from element to element. (c) The model provides the opportunity for an easy derivation of $B_{eq}$ for any arbitrary density, even in the case where $\bar{z}$ is not known, without the need to perform costly calculations. This is quite helpful in experimental cases where $B_{eq}$ can be extracted from the density alone.

Another important outcome of this analysis is the direct association of the present approach, which is an extension of Cohen's and Kelires's models for crystalline semiconductors to the amorphous state, with Thorpe's power-law variation for amorphous materials and glasses. Actually, it can be easily shown that the two models are equivalent to each other. Let us compare the equations (6.4) and (6.9). For the scaling

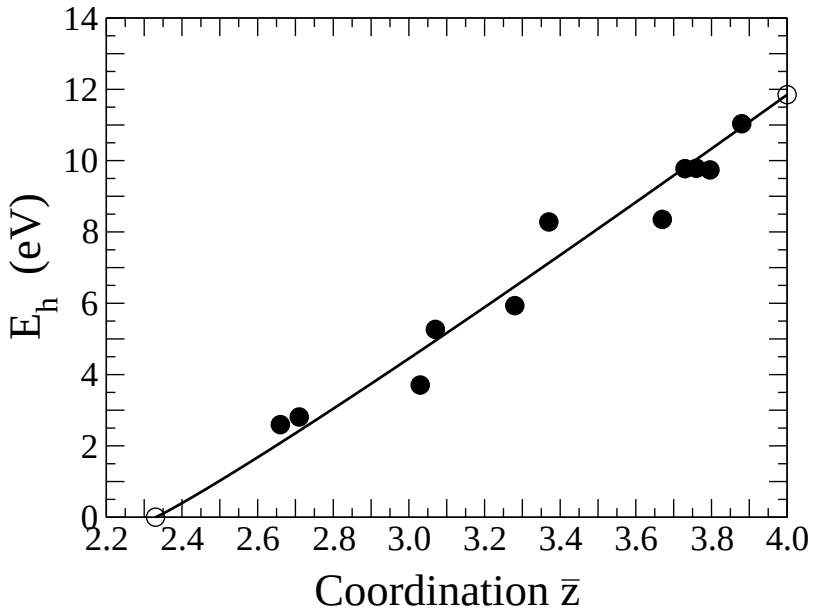


**Fig. 6.7**: Variation of homopolar gap as a function of the mean coordination $\bar{z}$. Open circles denote the extrapolated end points.

exponents $\nu$ (= 1.5) and $n$ (= 3.5) to be consistent to each other, the relative coordination number $\bar{z}_r = \bar{z} - \bar{z}_f$ should scale with $\bar{d}_r$ to the power of $\simeq 2.33$ (the multiplicative constants are about equal.) Indeed, a direct fit of our data to the relation $\bar{z}_r = A\ (\bar{d}_r)^\mu$ yields $A \simeq 1$ and $\mu = 2.3$, confirming the equivalence of the two power laws.

Perhaps, the most interesting aspect of the power-law dependence of $B_{eq}$ on $\bar{d}_r$ is the immediate implication for a definite trend in the variation of the *homopolar gap* $E_h$ in a-C. We propose here that one can have a very good estimate of $E_h$ for any a-C network, just from structural and elastic parameters and only a reference energy scale, without the need to carry out calculations of the electronic structure. $E_h$ plays the role of an average optical gap (the average bonding-antibonding splitting), like the energy gap parameter $E_G$ in the isotropic band model of Penn [82]. It is an important quantity, since it is associated with the complex dielectric function $\epsilon(E)$ and the plasmon energy $E_P$, which determines the density and the $sp^3$ content. Ferrari *et al.* [68] have pointed out the importance of considering $E_h$ in EELS theory for a-C, in order to remedy the approximation of a free-electron metal and account for the finite gap.

In order to calculate $E_h$ for any given a-C structure, we adopt the approach of Kelires for c-$Si_{1-x}C_x$ alloys. This is based on fundamental arguments given by Philips [80] and Cohen [78]. According to Philips, tetrahedral compounds sharing

eight valence electrons per atom pair are characterized by a covalent or homopolar gap $E_h$ and an ionic gap $C$. Examining a series of solids of increasing ionicity (group IV→III-V→II-VI) Cohen observed that the lattice constant, or $d$, is nearly independent of $C$ and one should expect that $B$ depends predominantly on the covalent character of the bond. He thus chose $E_h$ as the energy variable for covalent systems in analogy with the Fermi energy $E_f$ for the free-electron gas ($B = \frac{2}{3} n E_f$; $n$ is the electron concentration.) For group IV elements, the purest covalent materials with no ionic bonding, $B$ depends solely on $E_h$. Since $B$ scales inversely proportional to the covalent-bond volume ($\sim d$; bond charge densities have roughly cylindrical shape), Cohen suggested that

$$B_{eq} = D \; E_h \; d^{-1}, \tag{6.10}$$

where $D$ is a numerical constant. Kelires [81] generalized this argument to hold within a single alloy (c-$Si_{1-x}C_x$) series. Then taking as a reference the $E_h$ of either Si or C, he used Eq. (6.10) to extract $E_h$ as a function of composition from the calculated $B$'s and $d$'s.

In a similar manner, we propose that the analogous expression for a-C is

$$B_{eq} = D \; E_h \; \bar{d}_r, \tag{6.11}$$

since $B_{eq}$ scales proportional to $\bar{d}_r$. We furthermore need a reference energy scale. For this we use the homopolar gap of diamond (13.8 eV) [80]. Then, Eq. (6.11) yields the variation of $E_h$ with $\bar{z}$ in this series of a-C networks:

$$E_h(\bar{z}) \;=\; E_h(D) \left[ \frac{B_{eq}(\bar{z})}{B_{eq}(D)} \frac{\bar{d}_r(D)}{\bar{d}_r(\bar{z})} \right]. \tag{6.12}$$

The EDTB method gives $B_{eq}$(D) = 428 GPa and $\bar{d}$(D) = 1.55 Å (so $\bar{d}_r$(D) = 1.31 Å.) For the input data (the $B_{eq}$'s and $\bar{d}_r$'s) we use the calculated values.

The results are plotted in Fig. 6.7. We find the homopolar gap of the WWW model, or of the extrapolated amorphous tetrahedral network (they coincide), to be 11.9 eV compared to 13.8 eV for diamond. This is reasonable. An alternative rough estimate of $E_h$(WWW) can be reached by making the approximation that the ratio of homopolar and direct gaps of the WWW model and diamond are equal

$$\frac{E_h(WWW)}{E_h(D)} = \frac{E_g(WWW)}{E_g(D)}. \tag{6.13}$$

The $E_g$(WWW), as extracted from the electronic density of states using the EDTB method (not shown), equals 4.4 eV, and $E_g$(D) = 5.45 eV, so this approximation gives 11.1 eV for $E_h$(WWW), in reasonable agreement with the direct value. At the

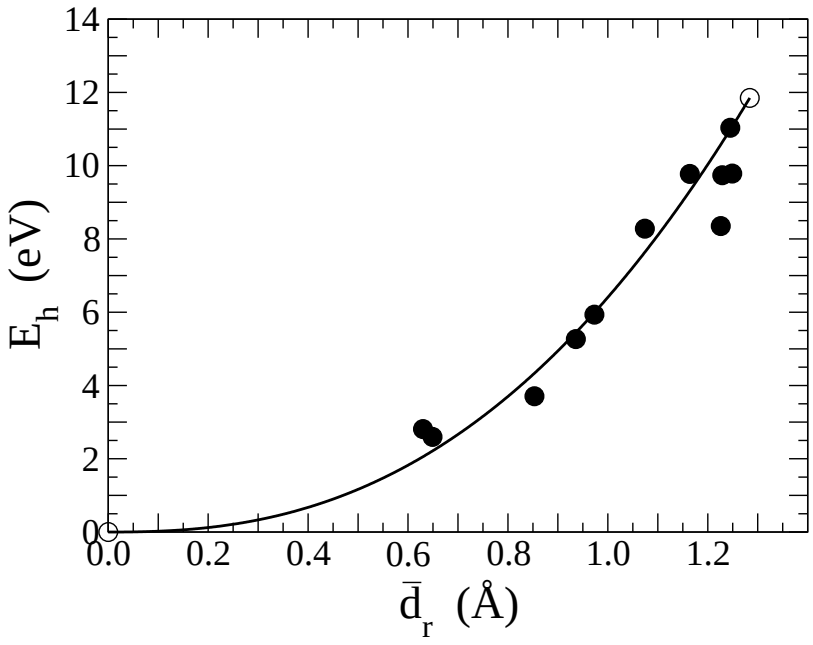


**Fig. 6.8**: Variation of homopolar gap as a function of the relative distance $\bar{d}_r$. Open circles denote the extrapolated end points.

other end, i.e., the floppy transition, the homopolar gap closes, as required by Eq. (6.12).

The best fit to the points of Fig. 6.7 is obtained using an expression similar to the power law in Eq. (6.4)

$$E_h(\bar{z}) = A\ (\bar{z} - \bar{z}_f)^{\nu}. \tag{6.14}$$

The fit gives $A = 6.8$ and $\nu = 1.07$. We can check the consistency of this scaling exponent by recalling that the relations $B_{eq} \sim (\bar{z}_r)^{1.5}$ and $B_{eq} \sim E_h(\bar{d}_r)^{1.0}$ are equivalent. Also, since $\bar{z}_r \sim (\bar{d}_r)^{2.33}$, we have that $\bar{d}_r \sim (\bar{z}_r)^{0.43}$. Therefore, $E_h \sim B_{eq}/\bar{d}_r \sim (\bar{z}_r)^{1.5}/(\bar{z}_r)^{0.43} \sim (\bar{z}_r)^{1.07}$.

Thus, the variation of $E_h$ with $\bar{z}$ or $sp^3$ content is close to be but not exactly linear. This implies also a slightly non-linear dependence of the gap on the plasmon energy $E_P$. Associated with $E_P$ is the interband effective electron mass $m^*$, which differentiates from the free-electron case and accounts for the finite energy gap. By comparing XRR and EELS densities, Ferrari *et al.* [68] made a linear fit over the experimental data and derived a constant $m^* = 0.87m$ for carbon systems, $m$ being the free-electron mass. They arrived at a linear relation between $E_h$ and $E_P$, namely

$$E_P = E_h \left(1 - \frac{m^*}{m}\right)^{-1/2}. \tag{6.15}$$

This is reasonable since our analysis shows only a small deviation from linearity. Eq. (6.15) together with our Eq. (6.14) can be used to predict the plasmon energy for an arbitrary a-C structure. For the WWW model, $E_P$ comes out to be $\sim 31$ eV.

Finally, the above results provide us with the dependence of $E_h$ on $\bar{d}_r$. A simple dimensional analysis reveals that $E_h$ scales as $(\bar{d}_r)^{2.5}$: $B_{eq} \sim (\bar{d}_r)^{3.5}$ and $B_{eq} \sim E_h(\bar{d}_r)^{1.0}$, thus $E_h \sim (\bar{d}_r)^{2.5}$. This is confirmed by plotting the computed values of $E_h$ as a function of $\bar{d}_r$, as shown in Fig. 6.8. A fit to the points leads to $E_h = 6.3\ (\bar{d}_r)^{2.5\pm0.05}$. We thus conclude that the scaling of $E_h$ in a-C networks follows the same form, except for the sign, like the scaling in crystalline tetrahedral compounds, as suggested by Philips [80]. This is not accidental, but it shows that these ideas are more general, extend beyond the simple tetrahedral case, and have applications in complex non-tetrahedral covalent compounds, even in the amorphous state. Note, that Philips's argument was the fundamental assumption on which the $d^{-3.5}$ scaling of $B_{eq}$, proposed by Cohen, is based. Here, we followed the reverse procedure. We first extracted the $(\bar{d}_r)^{3.5}$ scaling of $B_{eq}$, directly from calculations without any assumption, and then the scaling of $E_h$ naturally follows.

## 6.3 Conclusions

The complexity and rich variance of a-C networks, dinstictly marked from each other by their density and hybridization, offer the unique possibility to unravel fundamental physical trends, pertained to bonding, rigidity, and related properties. In this chapter, we have presented an in-depth investigation of such trends, mainly focusing on structural and mechanical properties. We based our analysis on TBMD simulations, using the reliable EDTB model and supplementary the NRL scheme.

We first extracted the variation of $sp^3$ fraction, or mean coordination, with density over the whole possible range, bounded from below by the density at the floppy transition and from above by the density of the fully tetrahedral amorphous network. The variation is linear and agrees well with experiment in the region above 1.8 gcm$^{-3}$, where experimental data are mostly abundant. We estimated the $sp^3$ content in low-density networks, as well as the density at the floppy transition. The density of "amorphous diamond" at the upper end of the spectrum is lower than diamond's.

The bulk moduli of a-C networks were shown to satisfy the constraint-counting model of Philips and Thorpe, with a critical coordination near 2.4, and to closely have a power-law behavior as a function of mean coordination with a scaling exponent equal to 1.5. Furthermore, we showed that the bulk moduli, as a function of an average effective distance, also follow a simple power law, which was previously proposed for crystalline semiconductor compounds and alloys. We showed the equiv-

alence of the two power laws. Finally, from these simple physical laws, based on only structural and elastic data, we extracted the variation of the homopolar gap in a-C networks.

Although demonstrated for the single series of a-C networks, the method and the accompanying analysis may be applied to other covalent amorphous systems as well, in order to unravel interesting physical trends.

# Chapter 7

# Electronic and Optical Properties of a-C

*The optoelectronic properties of amorphous carbon are less well understood than the structural and mechanical properties of amorphous carbon. This dissertaion aims at an elucidation and clarification of these issues. We first study the electronic structure and extract the density of states. We then obtain the dielectric function and the optical gaps and examine their variations as a function of the $sp^3$ fraction. Finally, we are able to associate the disorder in a-C networks with the Urbach energy, which shows a non-monotonic variation as a function of $sp^3$ fraction and density.*

## 7.1 Electronic density of states

The amorphous carbon networks used in this work have been constructed previously and presented in the chapter before. Here, we analyze three typical a-C cells with 86%, 75%, 45% $sp^3$ content. In addition, we use a WWW network, which has 100% $sp^3$ bonded atoms.

The first step of our study is to calculate the electronic density of states (EDOS) of the various networks. This is defined for every energy $E$ by the eigenvalues $\epsilon_i$ of our system

$$\rho(E) = \sum_{i=1}^{N} \delta(E - \epsilon_i) \tag{7.1}$$

where $N$ is the total number of the eigenstates. Fig. 7.1 shows the EDOS of the three quenched networks. We present the total contribution of all atoms, as well as the individual contributions of fourfold and threefold atoms separately. In the case

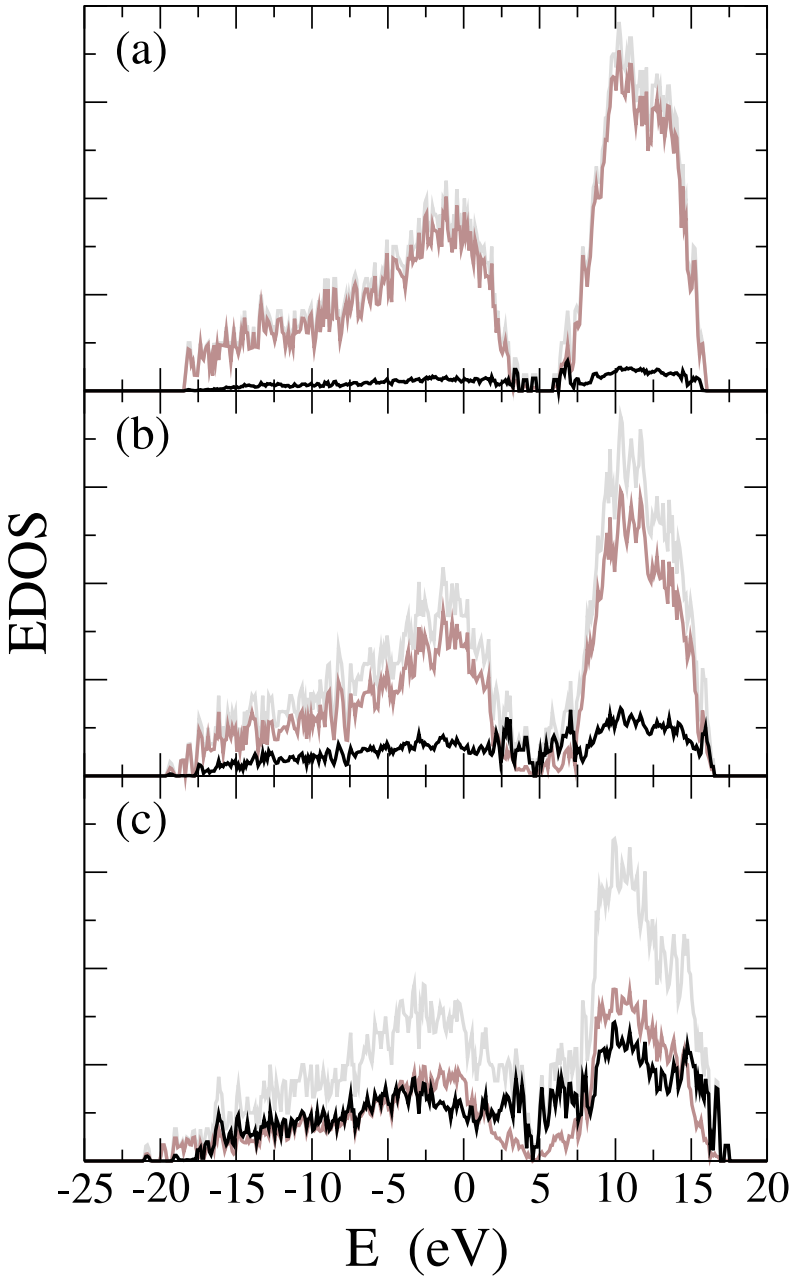


**Fig. 7.1**: The electronic density of states for a-C structures with different $sp^3$ content: (a) 86%, (b) 75% and (c) 45% $sp^3$ fraction. The light grey, grey and black lines correspond to the total, fourfold, threefold electronic density of states, respectively.

of the mostly $sp^3$-bonded network (86% $sp^3$, Fig. 7.1a), the EDOS consists of the $\sigma$ (occupied) and $\sigma^*$ (unoccupied) with a distinct band separation (gap). The $\pi$ and $\pi^*$ states are hardly identified. As the content of $sp^2$ increases (Fig. 7.1b and c), we

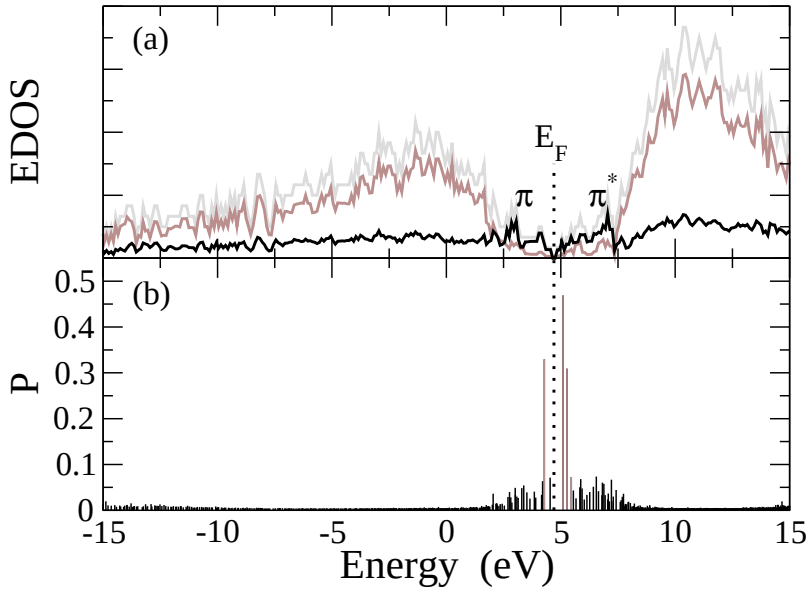


**Fig. 7.2**: (a) Electronic density of states (EDOS) of a *ta*-C network with 75% $sp^3$ atoms. The light grey, grey and black lines refer to the total, $sp^3$ and $sp^2$ projected contributions, respectively. (b) Inverse participation ratio $P$. Grey lines denote defects states.

observe that around the gap, the contribution of fourfold atoms vanishes while the EDOS of threefold atoms becomes the primary behavior, and the $\pi$ and $\pi^*$ peaks become evident. The optical gap is controlled by the low-energy transitions, which correspond to the $\pi$ - $\pi^*$ transitions of the $sp^2$-bonded atoms.

## 7.2 Defect states

We also demonstrate the highly localized nature of the $\pi$ states in our networks. Fig. 7.2(a) shows the EDOS of a ta-C network with 75% $sp^3$ content. The inverse participation ratio (IPR) $P$ near the gap region is shown in panel (b) of the previous figure. The IPR is defined as

$$P = \sum_i c_i^4 \tag{7.2}$$

where $c_i$ are the coefficients in the expansion of the eigenstates in terms of the local orbitals, and it is a measure of the localization of the electronic states. The $\pi$ and $\pi^*$ bands within the $\sigma - \sigma^*$ gap are clearly identified. Their IPR signifies that they are strongly localized, in agreement with previous calculations [83]. Some defect states at midgap near $E_F$ (grey lines in Fig7.2b) are also shown to be very localized. These are mainly due to isolated (unpaired) $sp^2$ sites. Note also the non-negligible

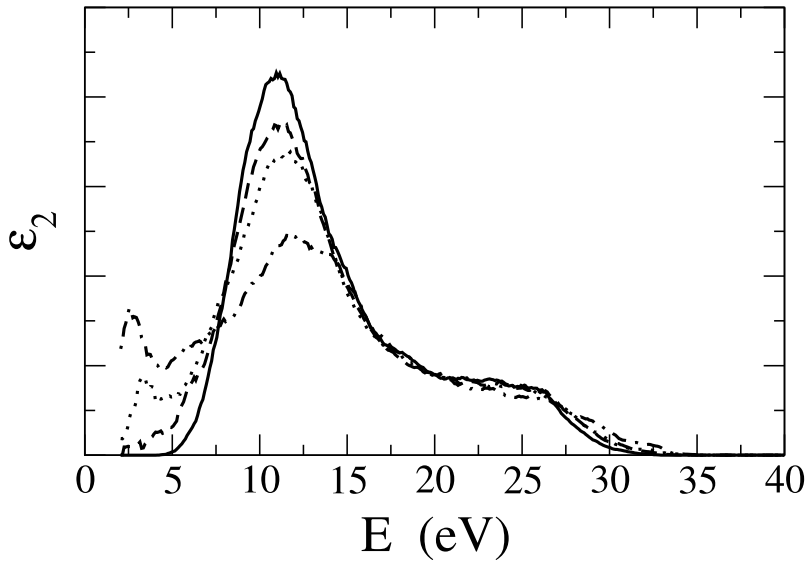


**Fig. 7.3**: The imaginary part of the dielectric function for the quenched a-C structures. The solid, dashed, dotted and dash-dotted lines show networks with 100%, 86%, 75% and 45% $sp^3$ fraction, respectively.

contribution to the EDOS in the gap region from fourfold-coordinated atoms. This originates from distorted $sp^3$ hybrids, and it is relevant to the discussion below.

## 7.3 Dielectric function

The electronic structure of the material is directly correlated with the complex dielectric function through its imaginary part, which is directly proportional to the joined density of states (JDOS) for interband electronic transitions. The main benefit of the calculated dielectric functions is the direct comparison of the theoretical results with the experimental data. The real and imaginary parts of the dielectric function of an amorphous semiconductor are related to each other through the general Kramers - Kronig dispersion relations

$$\epsilon_1(E) \sim 1 + \frac{2}{\pi} \int_0^\infty \frac{z}{z^2 - E^2} \epsilon_2(z) dz \tag{7.3}$$

$$E^2 \epsilon_2(E) \sim \sum |\langle f|\mathbf{P}|i\rangle|^2 \delta(E_f - E_i - E) \tag{7.4}$$

where $\mathbf{P}$ is the momentum operator, $E_f$, $E_i$ are the energy eigenvalues of the initial (valence) and final (conduction) states, and the sum is over all initial $i$ and final $f$

eigenstates. However, the wave functions for tight-binding models are not known, and the momentum matrix elements $\langle f|\mathbf{P}|i\rangle$ can not be calculated directly. In this case, we can use the approximation [85]

$$\hbar\langle f|\mathbf{P}|i\rangle = im(E_f - E_i)\langle f|\mathbf{r}|i\rangle \tag{7.5}$$

For further details, see the discussion in Chapter 4. The proof of the this approximation and the calculation of the momentum matrix elements, which is based on the latter, are presented there.

Following this procedure, we determined the imaginary part of the dielectric function ($\epsilon_2$) of various a-C networks. We calculated the optical matrix elements combining Eqs. 7.4 and 7.5; Fig. 7.3 shows the calculated $\epsilon_2$ for various a-C networks including the WWW cell. The dielectric function of the cells with significant $sp^2$ content exhibits two distinctive peaks at about 3 and 11 eV. On the other hand, the tetrahedrally bonded networks show only one welldefined peak at high energy. The first peak, when present, indicates the $\pi$ - $\pi^*$ transitions, and the second higher peak comes from the $\sigma$ - $\sigma^*$ transitions. A particularly interesting observation is that the high-energy peak of the $\sigma$ - $\sigma^*$ transitions moves to greater mean energies with increasing $sp^2$ content, which may be due to enhanced $\sigma$ - $\sigma^*$ transitions from the local graphite-like component of the films (the $\sigma$ - $\sigma^*$ peak in graphite is located at about 14 eV).

## 7.4 Optical gaps

In a crystal, a photon of energy $h\nu$ can induce a transition from a filled state of energy $E$ to an empty state of energy $E + h\nu$ only if the initial and final states have the same wave vector $\mathbf{k}$ and satisfy certain selection rules. Thus, among all the pairs of electron states separated by energy $h\nu$, only a few contribute to optical absorption.

But in a glass, no such restrictions apply. Assuming that we are dealing with extended states, all such pairs of states - filled, at energy $E$, and empty, at energy $E + h\nu$ - can contibute to optical processes.

An interesting and important electronic property of a-C to be used in optics and optoelectronics is the value of the fundamental gap $E_g$ . The optical band gap $E_g$ of a-C can be defined as the minimum gap between the occupied and unoccupied states (due to the amorphous character of the material) and can be based on the observation [86] that the upper portion of an amorphous solid's absorption edge is often well described by a parabolic relation

$$\alpha(E)E \sim (E - E_g)^2 \tag{7.6}$$

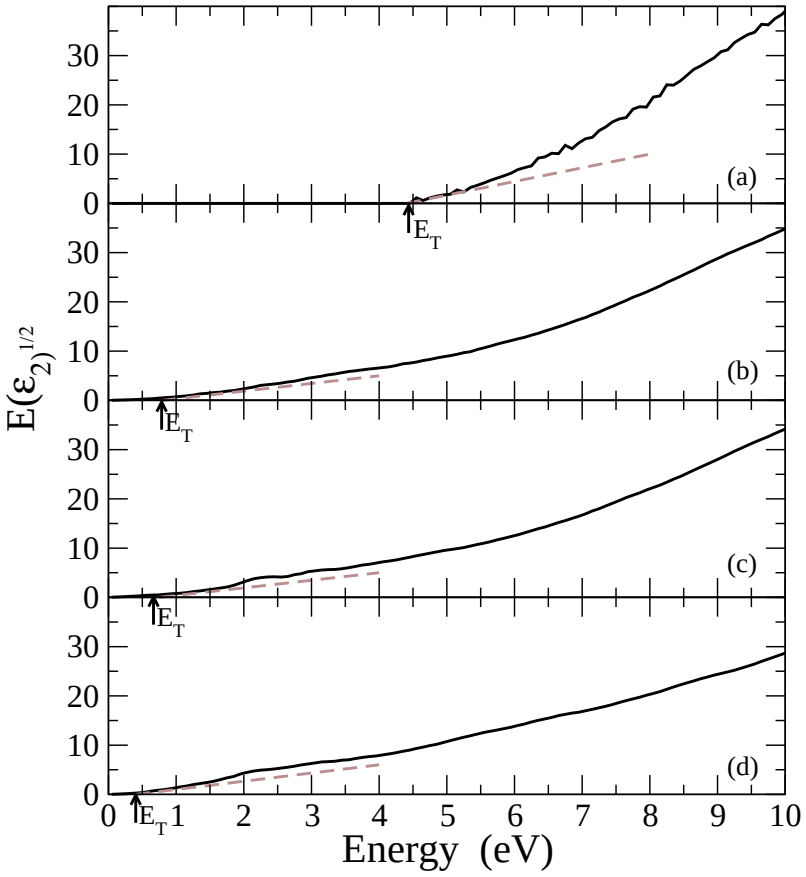


**Fig. 7.4**: Extraction of the Tauc gap from the imaginary part of the dielectric function. Panels (a), (b), (c) and (d) shows the data for 100%, 75%, 66% and 45% $sp^3$ atoms, respectively. The dashed lines demonstrate the fits. See text for details.

where $\alpha(E)$ is the absorption coefficient or equivalent

$$E\sqrt{\epsilon_2(E)} \sim E - E_g \tag{7.7}$$

In short we have minimized the calculations, which are shown in 'Methodology'.

This so-called 'Tauc gap', which is defined by Eq. 7.7, is determined by the plots of the quantity $E\sqrt{\epsilon_2}$ versus photon energy $E$ by extrapolating the linear plots to the energy axis. This is demonstrated in Fig. 7.4 for various cases.

Another definition of the optical gap is the energy value where the absorption coefficient

$$\alpha(E) = \frac{E\epsilon_2(E)}{\hbar nc} \tag{7.8}$$

reaches the value $10^4$ cm$^{-1}$. This gap is usually called $E_{04}$ [3, 87]. The calculation of $E_{04}$ requires knowledge of the refractive index $n$ of the studied material. We extract

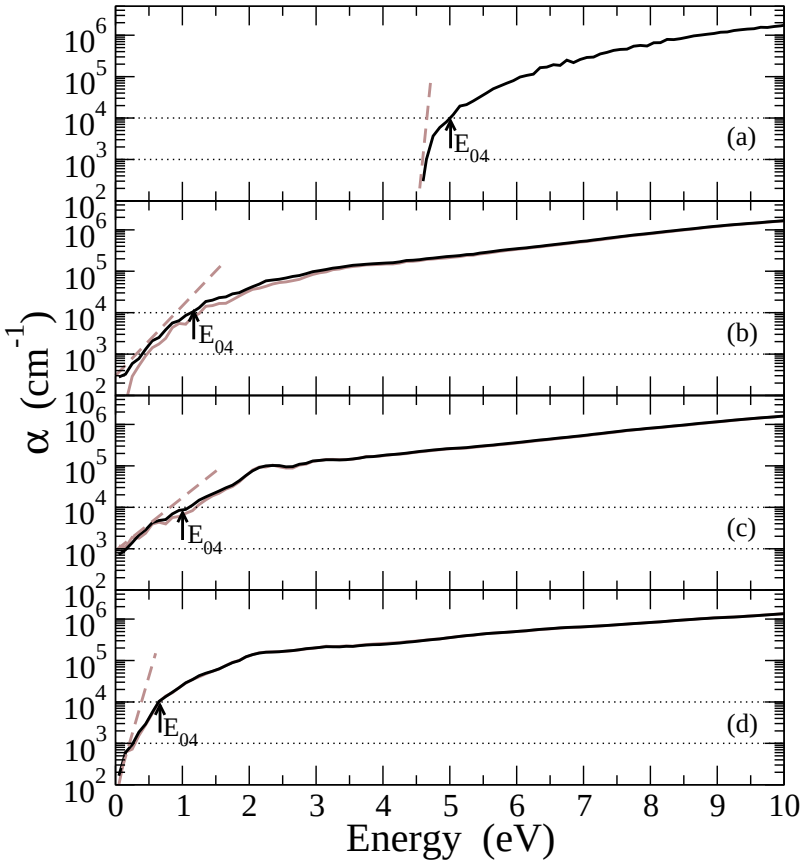


**Fig. 7.5**: Extraction of the $E_{04}$ gap and the Urbach energy $E_U$ from the absorption coefficient. Panels (a), (b), (c) and (d) shows the data for 100%, 75%, 66% and 45% $sp^3$ atoms, respectively. Grey solid lines show the absorption edge without defects. The dotted lines demonstrate the fits. See text for details.

$n$ by solving the system of equations $\epsilon_1 = n^2 - k^2$ and $\epsilon_2 = 2nk$. ($\epsilon_1$ is calculated from $\epsilon_2$ through the Kramers – Kronig dispersion relation, and the extinction coefficient $k$ is eliminated.) You can find every detail for the calculation of $n$ in a previous chapter. Fig. 7.5 demonstrates the estimation of $E_{04}$ from $\alpha(E)$ for different cells.

The variation of the calculated optical gaps as a function of $sp^3$ fraction is shown in Fig. 7.6. There is a rapid increase of the gap in the *ta*-C region, especially above 75% $sp^3$, signifying the dominant role of transitions between localized $\pi$ states. The gap is $\sim$ 2.5 eV for 86% $sp^3$ and reaches 5 eV for hypothetical *a*-D. (The gap for diamond is 5.5 eV with the present EDTB model.) The results of NRL model are presented in Fig. 7.6 too. The accuracy between the two models is stunning, concerning either the Tauc gap or the $E_{04}$ gap.

In order to compare our theoretical results, we asked for some "experimental

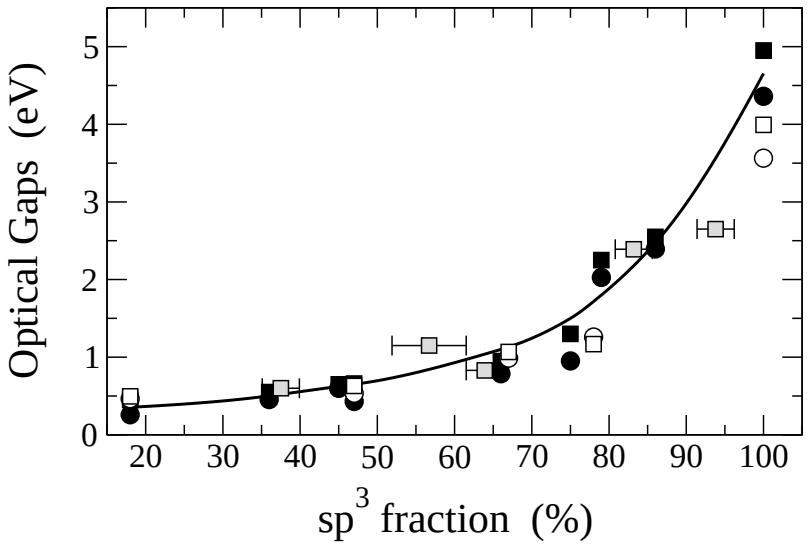


**Fig. 7.6**: Variation of the optical gaps as a function of the $sp^3$ fraction. Filled and open symbols are for the calculated values using EDTB and NRL model, respectively. Shaded symbols are for the experimental measurements. Squares and circles show the $E_{04}$ gap and the Tauc gap, respectively. Error bars for experimental $E_{04}$ gap and for calculated quantities are smaller than the symbols. Line is fit to the EDTB points.

assistance". The experimental work was carried out by Patsalas [25]. A number of *ta*-C samples were grown by Pulsed Laser Deposition (PLD) in a high-vacuum chamber ($P_b < 5 \times 10^5$ Pa) from a pure (99.999%) solid graphite target using the third harmonic ($\lambda = 255$ nm) of a Nd:YaG laser source. The laser fluence was fixed at 80 J/cm$^2$. The density of the films varied by applying an external electric field during growth, and has been determined by X-Ray Reflectivity (XRR) [25]. The $sp^3$ content was extracted from the density values using the eq. 6.2 from the previous chapter. Dielectric function spectra have been acquired in the spectral range 1.5-6.5 eV by an *ex situ* phase-modulated ellipsometer. The spectra were analyzed using two Tauc-Lorentz oscillators for the $\pi - \pi^*$ and $\sigma - \sigma^*$ transitions, respectively, as described in Refs. [25, 88]. The optical gap and $E_U$ were extracted from the real spectra of the films, excluding the substrate contribution.

The experimentally mesured $E_{04}$ gaps for the PLD samples are also shown in Fig. 7.6. They are in very good agreement with the theoretical variation. In addition, our calculated gaps agree well with previously reported experimental gaps in films prepared by filtered cathodic vacuum arc deposition [89]. The value for 100% $sp^3$ is also in accord with estimates by Ferrari and Robertson [90].

Both experimental and theoretical results show that the increase of $sp^2$ content

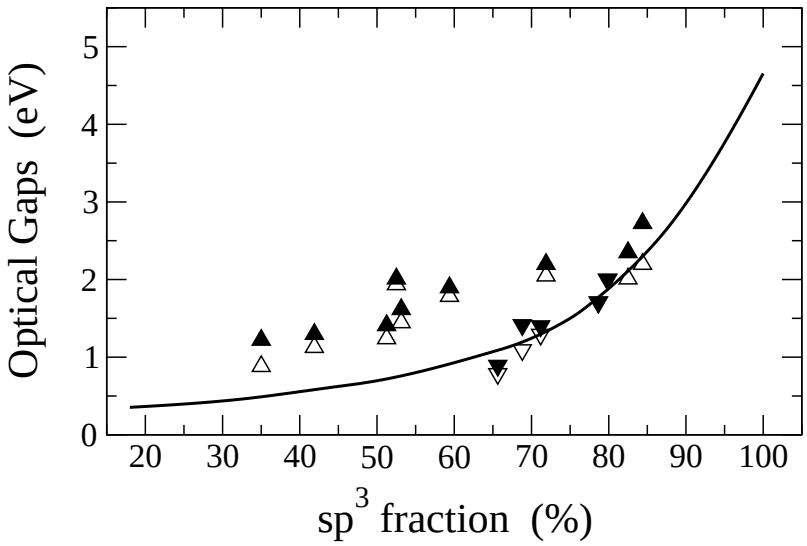


**Fig. 7.7**: Comparison of our fitted line (see Fig. 7.6 of optical gaps as a function of $sp^3$ fraction with experimental data. Filled symbols are for the $E_{04}$ gap, open symbols are for the Tauc gap. Up and down triangles show data from [91] and [89], respectively.

reduces considerably the Tauc Gap due to the increasing contribution of the $\pi$ - $\pi^*$ transition and the evolution of the $\pi$ and $\pi^*$ peaks at the high-energy edge of the valence band and the low-energy edge of the conduction band (see also Fig. 7.1), respectively. This clearly shows that the value of $E_g$ is mainly determined by the energy separation of the $\pi$ and $\pi^*$ bands.

Finally, we want to compare all our results with other experimental ones. We took data from Chhowalla [91] and Waidmann [89] which are presented in Fig 7.7 along with the line of Fig. 7.6, which derives from the fit of our points. We can observe that there is an agreement in the ta-C region but we have a difference as the $sp^3$ fraction drops. Furthermore, these two experimental data show a linear behaviour as opposed to ours, which behave in a clearly non-linear variation.

## 7.5 Urbach energy - Disorder

We now concentrate on the issue of linking disorder and optical parameters. For this purpose, we extract the Urbach energies $E_U$ and relate them to the $sp^3$ content and optical gap of our networks. $E_U$ is customarily defined as the inverse of the local slope of $\ln[\alpha(E)]$ at the $E_{03}$ photon energy [3, 92, 93], so that it captures quantitatively the variations of $\alpha(E)$ deep within the gap. These variations are, in

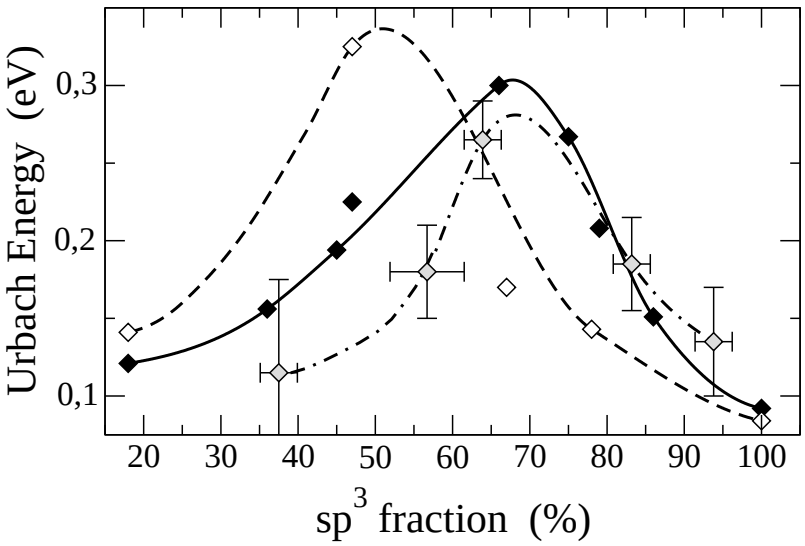


**Fig. 7.8**: Variation of the Urbach energy as a function of the $sp^3$ fraction. Filled and open symbols are for the calculated values using EDTB and NRL model, respectively. Shaded symbols are for the experimental measurements. The error bars are for experimental $sp^3$ and $E_U$. Lines are fits to the points.

general, associated to disorder-induced changes and to defects. Fig. 7.5 demonstrates the extraction of $E_U$ from $\alpha(E)$. The variation of $E_U$ with $sp^3$ fraction and optical gap is shown in Fig. 7.8.

The striking finding of this analysis is that $E_U$ does not increase monotonically with $sp^3$ fraction and gap, as observed in $a$-C:H, where the largest values of $E_U$ correspond to the highest gaps (in polymer-like films). Instead, the variation exhibits a maximum at around 65% $sp^3$, and then sharply declines dropping to $\sim$ 90 meV for $a$-D. This means that disorder becomes maximum at the lower side of the $ta$-C region, but then declines as $sp^2$ content is minimized and the gap widens.

We also present the results of NRL model in Fig. 7.8. We might not have accuracy in quantity between the results of the two models but they follow exactly the same non-monotonic trend.

This non-monotonic variation can be explained as follows: If we exclude for the moment the contribution from defects (mainly unpaired $sp^2$ sites), and the inherent distortions of the amorphous network, disorder in $a$-C builds up upon embedding "minority" configurations into a host phase. These can either be chains of $sp^2$ sites embedded in the high-density, $sp^3$-rich phase or $sp^3$ clusters embedded in the low-density, $sp^2$-rich phase. In both cases, the incompatibility due to the substantially different geometries, effective atomic volumes, and local electronic structure of $sp^3$

and $sp^2$ hybrids produces disorder, which increases along with the relative fraction of the minority component, giving rise to a maximum in the variation. However, more disorder is produced in *ta*-C (steeper rise of $E_U$) than in low-density *a*-C because of the rigid character of the network. The latter is easier to deform and adjust to the embedding. Confirmation of the theoretical trend in the *ta*-C region is provided by our experimental measurements of $E_U$ in the PLD samples. The extracted $E_U$ values are depicted in Fig. 7.8. They compare favorably with theory and confirm that the higher the $sp^3$ fraction and the optical gap the lower the disorder in *ta*-C. Ongoing work aims at extending the investigation to samples with lower density. We also have preliminary experimental results [88] for hydrogenated samples which confirm that, in this case, $E_U$ increases monotonically with optical gap, as found previously [3, 92, 94, 95]. This shows the reliability of the experimental analysis for the pure films in the *ta*-C region.

Note that for 100% $sp^3$ $E_U$ *is not zero*, which means that in this case $E_U$ measures the *inherent* structural disorder of the fully tetrahedral network (no $sp^2$ sites, no defects.) As the $sp^2$ fraction increases, $E_U$ rises. The question is whether this rise reflects to the additional structural disorder induced by the embedding, or/and to any topological disorder. To answer this question, we analyzed the $sp^2$ cluster distributions and bond-angle and length distortions in our networks. Fig. 7.9 shows a histogram of cluster (chain) distributions in the *ta*-C cells. It is evident that more numerous and larger chain sizes progressively appear with increasing $sp^2$ fraction. It is striking that for $\sim 30\%$ $sp^2$ sites, at which the maximum of $E_U$ occurs, long chains, grouped into larger clusters, dominate. Their distribution is inhomogeneous. Thus, the association between increasing topological disorder and $E_U$ seems likely.

As a measure of bond-angle distortions we consider the relative angle fluctuations $\Delta\theta = \sigma_\theta/\bar{\theta}$, where $\sigma_\theta$ are the standard deviations and $\bar{\theta}$ the mean values, extracted from the bond-angle distribution functions (not shown). We refer these quantities to the respective value for *a*-D, $\Delta\theta_r = (\Delta\theta - \Delta\theta_0)/\Delta\theta_0$, to show the excess structural disorder due to $sp^2$ embedding. The same is done for bond-length distortions (the pair distribution functions are used.) The results for the *ta*-C cells are shown in the inset of Fig. 7.9. While excess bond-length distortions are minimal, excess angle distortions are significant. At the maximum of $E_U$, they become $\sim 60\%$ higher than the inherent tetrahedral disorder. Therefore, the association between increasing structural disorder and $E_U$ also seems likely.

There is no straightforward way to separate the two contributions to $E_U$ and estimate their relative importance. The clustering of $sp^2$ sites alters the local electronic structure and affects the optical transitions, depending on the size and spatial distribution of chains, but in addition unavoidably produces structural disorder both

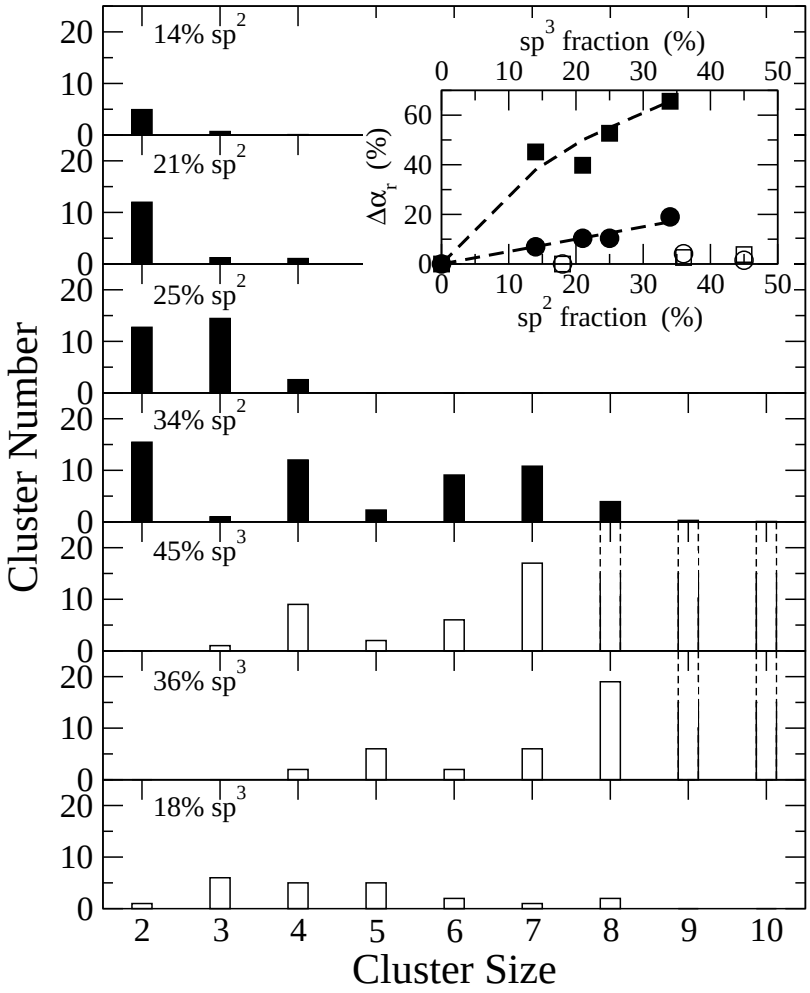


**Fig. 7.9**: Histograms of $sp^2$ chain and $sp^3$ cluster distributions in a number of *ta*-C and low-density *a*-C cells with increasing $sp^2$ and $sp^3$ content, respectively. The inset shows the respective relative bond-angle (squares) and bond-length (circles) fluctuations. Full symbols are for *ta*-C (referred to the ideal *a*-D case), while empty ones are for *a*-C (referred to the 18% $sp^3$ case). See text for definitions.

around the embedding in the $sp^3$ skeleton, and within the cluster itself. Thus, the two types of disorder are interlinked.

For $sp^2$-rich cells, on the other hand, we find that distortions vary slowly with increasing $sp^3$ content, as shown in Fig. 7.9, which can be attributed to the flexible nature of the network. Thus, the rise of $E_U$ in this case is predominantly associated with topological disorder due to the embedding of $sp^3$ clusters, as is evident from the cluster analysis in Fig. 7.9.

Another issue concerns the relative contributions to $E_U$ from hybrid states. Since

$E_U$ in $a$-C describes transitions between localized states, one expects that $\pi - \pi^*$ transitions are the major contributors. Surprisingly, we find that contributions from transitions involving localized $\sigma$ states also are considerable. This can be explained by referring to the EDOS in Fig. 7.2 which shows that such states, due to distorted $sp^3$ hybrids, are found localized at energies where the $\pi$ and $\pi^*$ peaks are located, well inside the $\sigma - \sigma^*$ gap, and thus lie at the Urbach edge. The distorted $sp^3$ hybrids are mainly found in the neighborhood of the embedded $sp^2$ chains, which in turn also get distorted. Thus, we have in $ta$-C topological $E_U$ due to $\pi$ states, and structural $E_U$ due to both $\pi$ and $\sigma$ states.

Finally, we examined the effect of unpaired $sp^2$ sites on the optical transitions. For this, we calculated the absorption coefficient by excluding the contribution of states localized on such defects. The result is plotted in Fig. 7.5. The comparison to the full absorption edge shows that the effect on both the $E_{04}$ and $E_U$ (slope of curve) is small, indicating that transitions between states localized on unpaired $sp^2$ sites, or between such states and neighboring $\pi$ and $\sigma$ states, are negligible. This is in contrast to $a$-Si:H, where the spin density due to dangling bonds is a major factor in shaping up the Urbach edge.

## 7.6 Conclusions

We have studied computationally the electronic properties of a-C networks with various $sp^3/sp^2$ content, using tight-binding molecular dynamics with the EDTB and NRL models. We calculated the electronic density of states (EDOS), the dielectric function and the fundamental gap of various networks. All networks show semiconducting behavior. We have also found that the EDOS is dominated by the $\sigma$ and $\pi$ occupied states and the $\sigma^*$ and $\pi^*$ unoccupied states, resulting to two distinct peaks in the dielectric function spectra, which correspond to $\sigma$ - $\sigma^*$ and $\pi$ - $\pi^*$ transitions. The energy positions of the $\sigma$ - $\sigma^*$ transition move to higher energy with increasing $sp^2$ content in agreement with the experimental observations. The fundamental gap is mainly determined by the energy separation of the $\pi$ and $\pi^*$ bands and varies between 0.3 and 2.7 eVs. The computational results are consistent with experimental studies of the optical properties of a-C using SE in the energy range 0.1 - 10 eV.

In conclusion, we presented in this chapter results of TB calculations, which offered insight into the link between disorder and optical properties in $a$-C films. We showed that the Urbach edge is associated to both topological and structural disorder, and that $E_U$ behaves non-monotonically with $sp^3$ fraction and optical gap. The theoretical results are backed by experimental measurements in the $ta$-C region.

Further work aims at extending the theoretical investigations to $a$-C:H, in order

to provide a direct understanding of the link between disorder and optical data, which until now has only been attempted through phenomenological modeling [92].

# Chapter 8

# Optical Properties of nanodiamond carbon

*We study the electronic and optical properties of diamond nanocrystals embedded in amorphous carbon using tight-binding molecular dymamics simulations. We calculate the electronic density of states, the dielectric function, the optical band gap, and the Urbach energy . By separating the nanodiamond contributions from those of the amorphous matrix, we show that the last one follows the trends of pure amorphous Carbon. The optical gap and Urbach energy for diamond inclusions retain constant values.*

## 8.1 Constructing nanodiamond carbon

Mechanical and electronic properties of nanostructured amorphous carbon (na-C) attract a lot of interest lately. This is due to the fact that this mixed phase offers the possibility to intermingle the properties of carbon nanostructures [5, 6] with those of pure amorphous carbon (a-C) [3, 4]. For instance, it is possible to tailor electronic properties by controlling the type and size of the nanostructures embedded in a-C, which may be insulating or metallic. One form of na-C observed are diamond nanocrystals embedded in an a-C [96, 97], which are predicted to have excellent mechanical properties [98]. In order to understand the electronic structure of this "nanodiamond" (nD) carbon we perform tight-binding molecular dynamics (TBMD) simulations.

We have already used TBMD in pure and nanostructured a-C networks [99, 100, 101, 102]. In chapters 5 and 6, we have studied the structural and mechanical properties of these a-C phases [99, 102]. Furthermore, in chap. 7 we have calculated

**Table 8.1**: Structural data of five representative nanostructured amorphous carbon networks.

| Sample | nD Volume fraction (%) | $\bar{z}_{\mathrm{AM}}$ | $sp^3_{\mathrm{AM}}$ (%) |
|---|---|---|---|
| A | 48.78 | 3.88 | 88 |
| B | 20.78 | 3.81 | 81 |
| C | 8.68 | 3.71 | 71 |
| D | 3.78 | 3.66 | 65 |
| E | 1.57 | 3.40 | 44 |

the electronic properties of pure a-C [100] and have recently presented a detailed study on optical properties of pure a-C [101]. We now apply the methodology of our recent works in the case of nD carbon.

The TBMD simulations are carried out in the canonical (N,V,T) ensemble. Temperature is controlled via a stochastic temperature control algorithm. The embedded nanostructures are formed by melting initially crystalline structures and subsequently quenching at constant volume, while keeping a certain number of atoms in the central portion of the cells frozen in their ideal crystal positions. Periodic boundary conditions are applied to the cells. We use cubic computational cells of a total of 512 atoms, while the number of atoms in the nanocrystals ranges from 50 to 250. After quenching, which produces amorphization of the surrounding matrix, the cells are thoroughly relaxed with respect to atom positions and density. Relaxations are particularly important at the interface region, where the crystallites mainly adjust to the host environment. Cells with varying coordination (density) of the amorphous matrix can be formed by changing the initial density (volume) of the crystal structures. The size (radius) of the nanocrystals is controlled by the choice of the number of the shells kept frozen during quenching.

## 8.2 Results and discussion

The nanostructured amorphous carbon networks used in this work have been constructed previously [102] and the samples produced have been studied in detail with respect to their structure and stability [102]. Here, we show the optoelectronic properties of five representative cells (among a significant number used in our calculations). Data for these five cells are presented in Table 8.1.

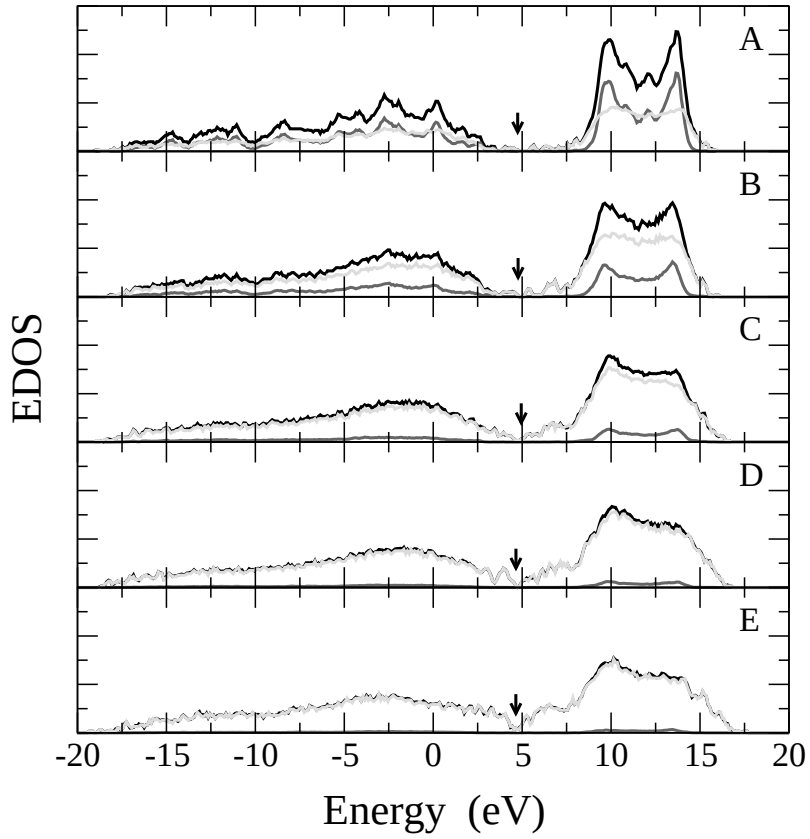


**Fig. 8.1**: The EDOS of the nanostructured a-C networks A - E included in Table 8.1. The black, grey and light grey lines correspond to the total, nD and AM contribution, respectively. Arrow indicates the Fermi level.

Fig. 8.1 shows the EDOS of those nanostructured networks. We present the total contribution of all atoms, as well as the partial EDOS of the nD and AM atoms separately. In the case of the sample with the greatest nD size (Fig. 8.1 - sample A), the crystalline behavior is dominant and it is characterized by the large gap and the presence of $\sigma$ (occupied) and $\sigma^*$ (unoccupied) states. The amorphous part also consists of mainly $\sigma$ and $\sigma^*$ peaks with a distinct band separation, since it has a great number of $sp^3$ amorphous atoms and the $\pi$, $\pi^*$ states are hardly identified.

As the number of diamond atoms decreases, so does the number of $sp^3$ atoms in the amorphous phase, and the amorphous matrix becomes less dense with increasing $sp^2$ atoms, the $\pi$ and $\pi^*$ peaks become evident. This happens due to supremacy of the $sp^2$ atoms' behavior.

If we study nD and AM separately, we observe that the crystalline atoms preserve their qualitative characteristics at all networks, even when they decrease in quantity.

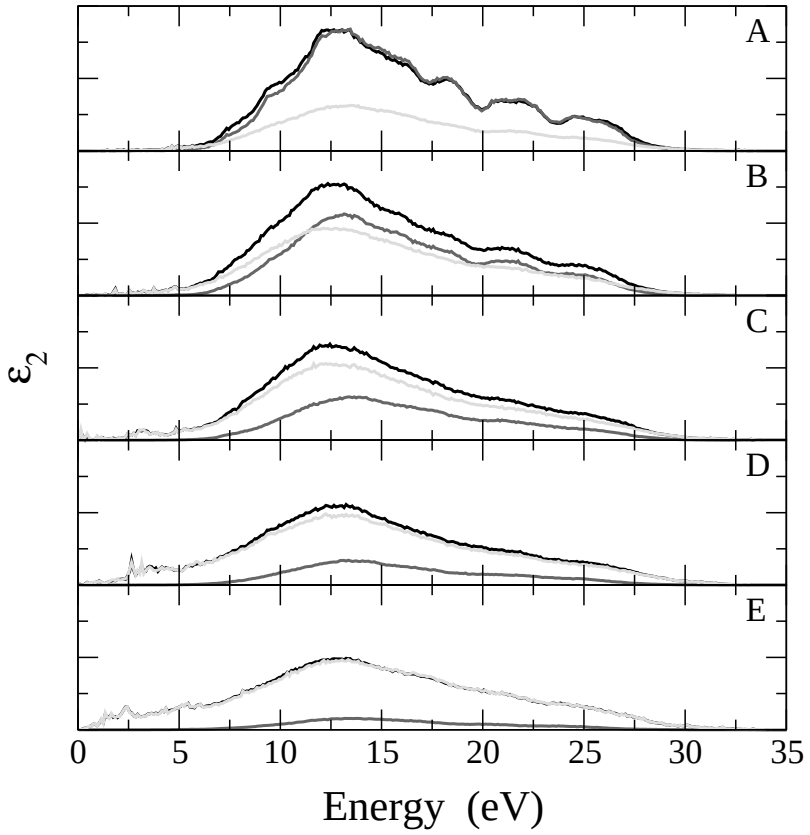


**Fig. 8.2**: The imaginary part of dielectric function of the nanostructured a-C networks A - E included in Table 8.1. The black, grey and light grey lines correspond to the total, nD and AM contribution, respectively.

Furthermore, the amorphous atoms of the nanocomposite behave as the amorphous atoms of pure a-C network. This can be verified with a comparison between our current nD carbon data with pure a-C data from a previous chapter [100]. We find similar results for the dielectric function. In Fig. 8.2 we present the imaginary part of the dielectric function, which provides very useful information about optical processes. When the $sp^3$ fraction is high and nD is large, only a primary peak exists which is due to $\sigma$ - $\sigma^*$ transitions. As the $sp^3$ ratio drops, a secondary peak also appears at lower energies due to $\pi$ - $\pi^*$ transitions. Individual study of nD and AM does not seem to introduce any additional knowledge other than what is already known for diamond and a-C, except for the fact that we do not clearly notice the shift of the major peak of AM to greater energies as the $sp^3$ atoms fraction decreases, like in pure a-C samples [100].

The optical band gap has also been calculated for all samples following the pro-

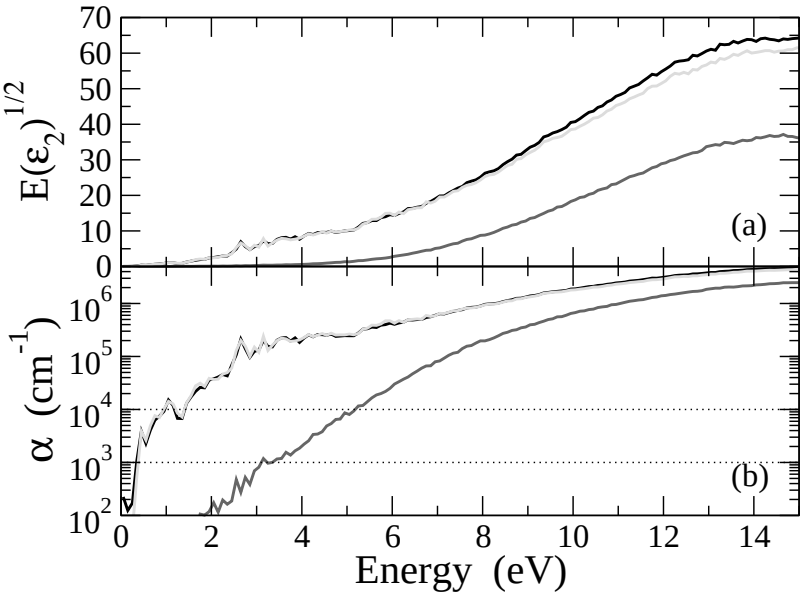


**Fig. 8.3**: Extraction of (a) the Tauc gap from the imaginary part of the dielectric function, and (b) the $E_{04}$ gap and the Urbach energy $E_U$ from the absorption coefficient, for the total (black line), nD (dark grey line) and AM (light grey line) contribution, respectively, for network D.

cedure described in chap. 4 and illustrated in Fig. 8.3. The Tauc gap is estimated by fitting a line at the $E\sqrt{\epsilon_2}$ versus $E$ curve (Fig. 8.3a). Estimation of $E_{04}$ gap and Urbach energy ($E_U$) is also shown (Fig. 8.3b). By investigating not only the total gap but also the partial contributions of nD and AM, we observe that for the amorphous part $E\sqrt{\epsilon_2}$ gets nonzero values at lower energies and dominates in the optical gap calculation.

This becomes clear in Fig. 8.4, where the optical gap of nD and AM is plotted separately, as a function of the $sp^3$ fraction. For comparison, we show data for pure a-C (see chap. 7) [101] and diamond using the EDTB model. We observe that AM atoms behave exactly as the pure a-C atoms do. The non-linear variation between gap and $sp^3$ ratio is preserved. Furthermore, nD atoms have an approximately constant value of band separation, which is close to diamond's optical gap.

Finally, in Fig. 8.5 we present the dependence of Urbach energy as a function of $sp^3$ fraction. Data for $E_U$ of pure a-C are given for comparison. AM contribution follows the trend of pure a-C. It exhibits a non-monotonic behavior with a maximum near to the one of pure a-C data. This result is expected from our previous observations that nD and AM behave like pure diamond and a-C, respectively.

A noteable difference between nD and bulk diamond is Urbach energy. Although

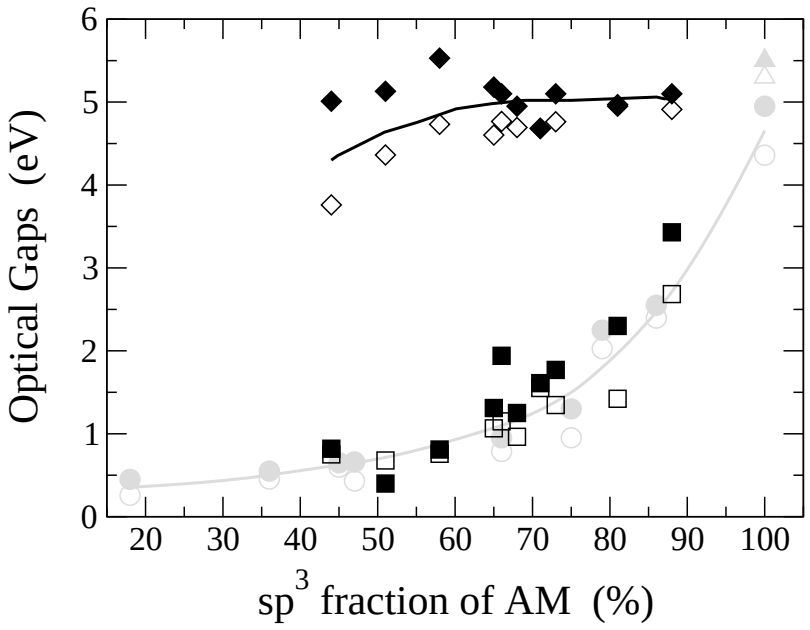


**Fig. 8.4**: Variation of the optical gaps as a function of $sp^3$ fraction. Diamonds and squares (black symbols) indicate the nD and AM contribution, respectively. For comparison triangles and circles (grey symbols) show the values of pure diamond and a-C [101], respectively. Filled symbols are for the $E_{04}$ gap and open symbols for the Tauc gap. Lines are trends for the average gaps' value of nD (black) and pure a-C [101] (grey).

non-existent in diamond, $E_U$ for nD atoms in our nanocomposites has a high value. This could be due to the disorder at the interface between crystalline and amorphous phase.

## 8.3 Conclusions

We studied the electronic and optical properties of nanostructured a-C consisting of nanodiamond inclusions in a-C. We applied the same methodology we had developed and used already in pure a-C, for the case of this nanocomposite a-C. We calculated the EDOS and the dielectric function by using TBMD simulations with the EDTB model. From the latter, we extracted the optical band gaps and the Urbach energies. We separated the partial contributions from the nanocrystals and a-C and found that the results for the amorphous matrix follow our previous findings about pure a-C, such as nonlinear gap behavior and non-monotonic relation between $E_U$ and $sp^3$ fraction. The atoms of nD have an approximately constant value of optical gap and $E_U$. This value of nD band separation reaches the value of the gap

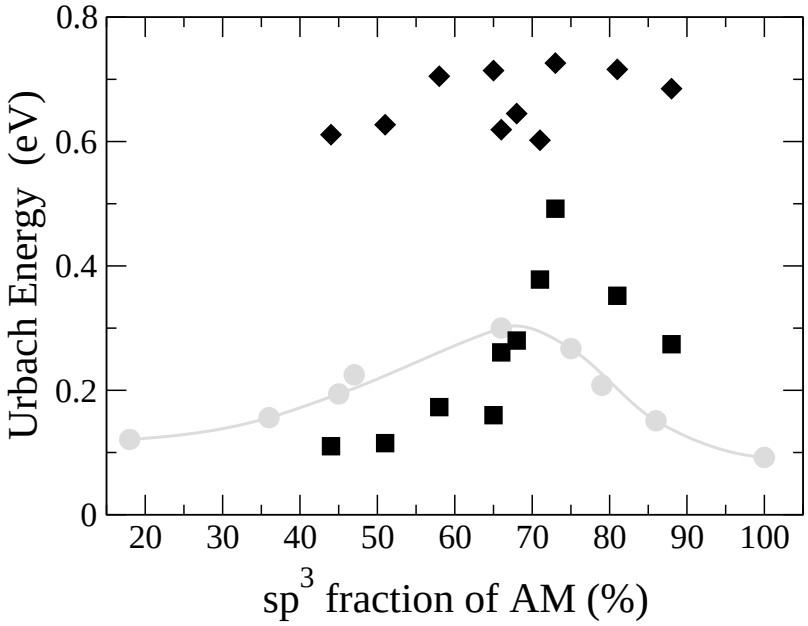


**Fig. 8.5**: Variation of the Urbach energy as a function of $sp^3$ fraction. Diamonds and squares (black symbols) indicate the nD and AM contribution, respectively. For comparison circles (grey symbols) show the values of pure a-C [101].

of diamond. However, the $E_U$ of the core nD atoms is oddly high and we explain this due to disorder at the interface of nD and AM atoms.

# List of Figures

# List of Tables

# Publications

Related to the thesis:

- *'Disorder and optical properties of amorphous carbon'*,
  C. Mathioudakis, G. Kopidakis, P. Patsalas, and P. C. Kelires,
  Diamond and Related Materials **16**, 1788 (2007).

- *'Structure, elastic properties and strength of amorphous and nanocomposite carbon'*,
  I. N. Remediakis, M. G. Fyta, C. Mathioudakis, G. Kopidakis, and P. C. Kelires,
  Diamond and Related Materials **16**, 1835 (2007).

- *'Electronic and optical properties of a-C from tight-binding molecular dynamics simulations'*,
  C. Mathioudakis, G. Kopidakis, P. C. Kelires, P. Patsalas, M. Gioti, and S. Logothetidis,
  Thin Solid Films **482**, 151 (2005).

- *'Structure, stability and stress properties of amorphous and nanostructured carbon films'*,
  M. G. Fyta, C. Mathioudakis, G. Kopidakis, and P. C. Kelires,
  Thin Solid Films **482**, 56 (2005).

- *'Physical trends in amorphous carbon: a tight-binding molecular dynamics study'*,
  C. Mathioudakis, G. Kopidakis, P. C. Kelires, C. Z. Wang, and K. M. Ho,
  Physical Review B **70**, 125202 (2004).

Other publications:

- *'Nanomechanical properties of multilayered amorphous carbon structures'*, C. Mathioudakis, P. C. Kelires, Y. Panagiotatos, P.Patsalas, C. Charitidis, and S. Logothetidis, Physical Review B **65**, 205203 (2002).
- *'Softening of elastic moduli of amorphous semiconductors'*, C. Mathioudakis, and P. C. Kelires, Journal of Non-Crystalline Solids **266-269**, 161 (2000).

# Bibliography


[1] R. Zallen *The Physics of Amorphous Solids*, J. Wiley & Sons, Toronto (1983).

[2] H. O. Pierson, *Handbook of Carbon, Graphite, Diamond and Fullerenes*, Noyes Publications, New Jersey (1993).

[3] J. Robertson, *Diamond-like amorphous carbon*, Mater. Sci. Eng. R **37**, 129 (2002).

[4] S. R. P. Silva, *Amorphous carbon thin films*, in *Handbook of Thin Film Materials*, edited by H.S. Nalwa, Vol. **4**, p. 403, Academic Press, New York (2002).

[5] S. Subramoney, *Novel nanocarbons - Structure, properties, and potential applications*, Adv. Mater. **10**, 1157 (1998).

[6] F. Banhart, *Irradiation effects in carbon nanostructures*, Rep. Prog. Phys. **62**, 1181 (1999).

[7] V. V. Brazhkin, A. G. Lyapin, S. V. Popova, S. C. Bayliss, T.D. Varfolomeeva, R. N. Voloshin, A. G. Gavrilyuk, M. V Kondrin, V. V. Mukhamadyarov, I. A. Troyan, S. V. Demishev, A. A. Pronin, and N. E. Sluchanko, *Interplay between the structure and properties of new metastable carbon phases obtained under high pressures from fullerite $C_{60}$ and carbyne*, JETP Lett. **76**, 681 (2002).

[8] M. G. Fyta, I. N. Remediakis, and P. C. Kelires, *Energetics and stability of nanostructured amorphous carbon*, Phys. Rev. B **67**, 035423 (2003).

[9] Y. Lifshitz, *Pitfalls in amorphous carbon studies*, Diam. Relat. Mater. **12**, 130 (2003).

[10] D. Vanderbilt and J. Tersoff, *Negative-curvature fullerene analog of $C_{60}$*, Phys. Rev. Lett. **68**, 511 (1992).

[11] M. Keeffe, G. B. Adams, and O. F. Sankey, *Predicted new low energy forms of carbon*, Phys. Rev. Lett. **68**, 2325 (1992).

[12] D. Donadio, L. Colombo, P. Milani, and G. Benedek, *Growth of Nanostructured Carbon Films by Cluster Assembly*, Phys. Rev. Lett. **83**, 776 (1999).

[13] E. Barborini, P. Piseri, A. Li Bassi, A. C. Ferrari, C. E. Bottani, and P. Milani, *Synthesis of carbon films with controlled nanostructure by separation of neutral clusters in supersonic beams*, Chem Phys. Lett. **300**, 633 (1999).

[14] L. Ravagnan, F. Siviero, C. Lenardi, P. Piseri, E. Barborini, P. Milani, C. S. Casari, A. Li Bassi, and C. E. Bottani, *Cluster-Beam Deposition and in situ Characterization of Carbyne-Rich Carbon Films*, Phys. Rev. Lett. **89**, 285506 (2002).

[15] D. M. Gruen, Ann. Rev. Mater. Sci. **29**, 211 (1999).

[16] P. C. Kelires, *Energetics and stability of diamondlike amorphous carbon*, Phys. Rev. Lett. **68**, 1854 (1992); *Structural properties and energetics of amorphous forms of carbon*, Phys. Rev. B **47**, 1829 (1993).

[17] P. C. Kelires, *Elastic Properties of Amorphous Carbon Networks*, Phys. Rev. Lett. **73**, 2460 (1994).

[18] P. C. Kelires, *Intrinsic stress and local rigidity in tetrahedral amorphous carbon*, Phys. Rev. B **62**, 15686 (2000).

[19] P. C. Kelires, *Stress properties of diamond-like amorphous carbon*, Physica B **296**, 156 (2001).

[20] P. C. Kelires, *Intrinsic stress and stiffness variations in amorphous carbon*, Diam. Relat. Mater. **10**, 139 (2001).

[21] C. Mathioudakis, P. C. Kelires, C. Charitidis, P. Patsalas, and S. Logothetidis, *Nanomechanical properties of multilayered amorphous carbon structures*, Phys. Rev. B **65**, 205203 (2002).

[22] M. Gioti, S. Logothetidis, C. Charitidis, Y. Panayiotatos, and I. Varsano, *On the properties and functionality of ultra-thin diamond related protective coatings used in optical systems* , Sens. Actuators **A99**, 35 (2002).

[23] M. Gioti, and S. Logothetidis, *Dielectric function, electronic properties and optical constants of amorphous carbon and carbon nitride films*, Diamond Relat. Mater. **12**, 957 (2003).

[24] S. Logotehidis, *Optical and electronic properties of amorphous carbon materials*, Diamond Relat. Mater. **12** 141 (2003).

[25] P. Patsalas, S. Logothetidis, and P.C. Kelires, *Surface and interface morphology and structure of amorphous carbon thin and multilayer films*, Diamond Relat. Mater. **14**, 1241 (2005).

[26] For recent reviews of interesting carbon nanostructures, see S. Subramoney, *Novel Nanocarbons - Structure, Properties, and Potential Applications*, Adv. Mater. **10**, 1157 (1998); F. Banhart, *Irradiation effects in carbon nanostructures*, Rep. Prog. Phys. **62**, 1181 (1999).

[27] UCFMG and Group, *Diamond Growth and Films*, Elsevier, London/New York (1989).

[28] A. G. Whittaker, *Carbon: A New View of Its High-Temperature Behavior*, Science **200**, 763 (1978).

[29] H. Kroto, *Space, Stars, $C_{60}$, and Soot*, Science **242**, 1139 (1988).

[30] W. Kratschmer, D. L. Lowell, K. Fostiropoulos, and D. R. Huffman, *Solid $C_{60}$: a new form of carbon*, Nature **347**, 354 (1990).

[31] P. R. Surjan, *$sp^3$ hybridized carbons on buckminsterfullerene*, J. Molecular Structure **338**, 215 (1995).

[32] H.W. Kroto, J.R. Health, S.C. O' Brien, R.F. Curl, and R.E. Smalley, *C60: Buckminsterfullerene*, Nature **318**, 162 (1985).

[33] S. Iijima, *Helical microtubules of graphitic carbon*, Nature **354**, 56 (1991).

[34] D. A. Papaconstantopoulos, *Handbook of the band structure of elements solids*, Plenum Press, London (1986).

[35] W. A. Harrison, *Electronic structure and the properties of solids*, W. H. Freeman, San Francisco (1980); Dover, New York (1989).

[36] M. S. Tang, C. Z. Wang, C. T. Chan, and K. M. Ho, *Enviroment-dependent tight-binding potential model*, Phys. Rev. B **53**, 979 (1996).

[37] C. H. Xu, C. Z. Wang, C. T. Chan, and K. M. Ho, *A transferable tight-binding potential for carbon*, J. Phys: Condens. Matter **4**, 6047 (1992).

[38] R. Haerle, E. Riedo, A. Pasquarello, and A. Baldereschi, *$sp^2/sp^3$ hybridization ratio in amorphous carbon from C 1s core-level shifts: X-ray photoelectron spectroscopy and first-principles calculation*, Phys. Rev. B **65**, 045101 (2001).

[39] J. Y. Raty, G. Galli, C. Bostedt, T.W. van Buuren, and L.J. Terminello, *Quantum Confinement and Fullerenelike Surface Reconstructions in Nanodiamonds*, Phys. Rev. Lett. **90**, 037401 (2003).

[40] R. E. Cohen, M. J. Mehl, and D. A. Papaconstantopoulos, *Tight-binding total-energy method for transition and noble metals*, Phys. Rev. B **50**, 14694 (1994).

[41] M. J. Mehl, and D. A. Papaconstantopoulos, *Applications of a tight-binding total-energy method for transition and noble metals: Elastic constants, vacancies, and surfaces of monoatomic metals*, Phys. Rev. B **54**, 4519 (1996).

[42] P. Hohenberg, and W. Kohn, *Inhomogeneous Electron Gas*, Phys. Rev. **136**, B864 (1964).

[43] D. A. Papaconstantopoulos, M. J. Mehl, S. C. Erwin, and M. R. Pederson, *Tight-binding hamiltonians for carbon and silicon*, in *Tight-Binding Approach to Computational Materials Science*, edited by P. E. A. Turchi, A. Gonis, and L. Colombo, MRS Proceedings Vol. **491**, Materials Research Society, Warrendale (1998).

[44] H. C. Andersen, *Molecular dynamics simulations at constant pressure and/or temperature*, J. Chem. Phys. **72**, 2384 (1980).

[45] W. G. Hoover, A. J. C. Ladd, and B. Moran, *High-Strain-Rate Plastic Flow Studied via Nonequilibrium Molecular Dynamics*, Phys. Rev. Lett. **48**, 1818 (1982).

[46] S. Nosé, *A molecular dynamics method for simulations in the canonical ensemble*, Molec. Phys. **52**, 255 (1984); Molec. Phys. **100**, 191 (2002).

[47] S. Nosé, *A unified formulation of the constant temperature molecular dynamics methods*, J. Chem. Phys. **81**, 511 (1984).

[48] W. G. Hoover, *Canonical dynamics: Equilibrium phase-space distributions*, Phys. Rev. A **31**, 1695 (1985).

[49] F. Wooten, K. Winer, and D. Weaire, *Computer Generation of Structural Models of Amorphous Si and Ge*, Phys. Rev. Lett. **54**, 1392 (1985).

[50] F. Wooten, and D. Weaire, *Modeling tetrahedrally bonded random networks by computer*, Solid State Phys. **40**, 1 (1987).

[51] R. M. Martin, *Elastic Properties of ZnS Structure Semiconductors*, Phys. Rev. B **1**, 4005 (1970).

[52] P. N. Keating, *Effect of Invariance Requirements on the Elastic Strain Energy of Crystals with Application to the Diamond Structure*, Phys. Rev. **145**, 637 (1966).

[53] B. R. Djordjević, M. F. Thorpe, and F. Wooten, *Computer model of tetrahedral amorphous diamond*, Phys. Rev. B **52**, 5685 (1995).

[54] F.D. Murnaghan, *The Compressibility of Media under Extreme Pressures*, Proc. Natl. Acad. Sci. U.S.A. **30**, 244 (1944).

[55] T. Frauenheim, P. Blaudeck, U. Stephan, and G. Jungnickel, *Atomic structure and physical properties of amorphous carbon and its hydrogenated analogs*, Phys. Rev. B **48**, 4823 (1993).

[56] U. Stephan, T. Frauenheim, P. Blaudeck, and G. Jungnickel, *$\pi$ bonding versus electronic-defect generation: An examination of band-gap properties in amorphous carbon*, Phys. Rev. B **50**, 1489 (1994).

[57] T. Frauenheim, G. Jungnickel, U. Stephan, P. Blaudeck, S. Deutchmann, M. Weiler, S. Sattel, K. Jung, and H. Ehrhardt, *Atomic-scale structure and electronic properties of highly tetrahedral hydrogenated amorphous carbon*, Phys. Rev. B **50**, 7940 (1994).

[58] D. A. Drabold, P. A. Fedders, and P. Stumm, *Theory of diamondlike amorphous carbon*, Phys. Rev. B **49**, 16415 (1994).

[59] N. A. Marks, D. R. McKenzie, B. A. Pailthorpe, M. Bernasconi, and M. Parrinello, *Microscopic Structure of Tetrahedral Amorphous Carbon*, Phys. Rev. Lett. **76**, 768 (1996); *Ab initio simulations of tetrahedral amorphous carbon*, Phys. Rev. B **54**, 9703 (1996).

[60] M. P. Siegal, D. R. Tallant, P. N. Provencio, D. L. Overmyer, R. L. Simpson, and L. J. Martinez-Miranda, *Ultrahard carbon nanocomposite films*, Appl. Phys. Lett. **76**, 3052 (2000).

[61] M. P. Siegal, D. R. Tallant, L. J. Martinez-Miranda, J.C. Barbour, R.L. Simpson, and D.L. Overmyer, *Nanostructural characterization of amorphous diamondlike carbon films*, Phys. Rev. B **61**, 10 451 (2000).

[62] D. G. McCulloch, D. R. McKenzie, and C. M. Goringe, *Ab initio simulations of the structure of amorphous carbon*, Phys. Rev. B **61**, 2349 (2000).

[63] K. W. R. Gilkes, P. H. Gaskell, and J. Robertson, *Comparison of neutron-scattering data for tetrahedral amorphous carbon with structural models*, Phys. Rev. B **51**, 12303 (1991).

[64] D. S. Franzblau, *Computation of ring statistics for network models of solids*, Phys. Rev. B **44**, 4925 (1991).

[65] J. C. Philips, *Topology of covalent non-crystalline solids I: Short-range order in chalcogenide alloys*, J. Non-Cryst. Solids **34**, 153 (1979).

[66] M. F. Thorpe, *Continuous deformations in random networks*, J. Non-Cryst. Solids **57**, 355 (1983).

[67] P. J. Fallon, V. S. Veerasamy, C. A. Davis, J. Robertson, G. A. J. Amaratunga, W. I. Milne, and J. Koskinen, *Properties of filtered-ion-beam-deposited diamondlike carbon as a function of ion energy*, Phys. Rev. B **48**, 4777 (1993).

[68] A. C. Ferrari, A. Libassi, B. K. Tanner, V. Stolojan, J. Yuan, L. M. Brown, S. E. Rodil, B. Kleinsorge, and J. Robertson, *Density, $sp^3$ fraction, and cross-sectional structure of amorphous carbon films determined by x-ray reflectivity and electron energy-loss spectroscopy*, Phys. Rev. B **62**, 11089 (2000).

[69] J. Schwan, S. Ulrich, T. Theel, H. Roth, H. Ehrhardt, P. Becker, and S. R. P. Silva, *Stress-induced formation of high-density amorphous carbon thin films*, J. Appl. Phys. **82**, 6024 (1997).

[70] N. A. Marks, *Generalizing the environment-dependent interaction potential for carbon*, Phys. Rev. B **63**, 035401 (2000).

[71] M. Bazant and E. Kaxiras, *Modeling of Covalent Bonding in Solids by Inversion of Cohesive Energy Curves*, Phys. Rev. Lett. **77**, 4370 (1996); M. Bazant, E. Kaxiras, and J. F. Justo, *Environment-dependent interatomic potential for bulk silicon*, Phys. Rev. B **56**, 8542 (1997).

[72] G. Galli, R. Martin, R. Car, and M. Parrinello, *Ab initio calculation of properties of carbon in the amorphous and liquid states*, Phys. Rev. B **42**, 7470 (1990).

[73] H. He and M. F. Thorpe, *Elastic Properties of Glasses*, Phys. Rev. Lett. **54**, 2107 (1985).

[74] D. S. Franzblau and J. Tersoff, *Elastic properties of a network model of glasses*, Phys. Rev. Lett. **68**, 2172 (1992).

[75] B. R. Djordjević and M.F. Thorpe, *The bulk modulus of covalent random networks*, J. Phys.: Condens. Matter **9**, 1983 (1997).

[76] B. Schultrich, H. J. Scheibe, D. Drescher, and H. Ziegele, *Deposition of superhard amorphous carbon films by pulsed vacuum arc deposition*, Surf. Coatings Technol. **98**, 1097 (1998).

[77] A. C. Ferrari, J. Robertson, M. G. Beghi, C. E. Bottani, F. Ferulano, and R. Pastorelli, *Elastic constants of tetrahedral amorphous carbon films by surface Brillouin scattering*, Appl. Phys. Lett. **75**, 1893 (1999).

[78] M. L. Cohen, *Calculation of bulk moduli of diamond and zinc-blende solids*, Phys. Rev. B **32**, 7988 (1985).

[79] A. Y. Liu, M. Cohen, K. C. Hass, and M. A. Tamor, *Structural properties of a three-dimensional all-$sp^2$ phase of carbon*, Phys. Rev. B **43**, 6742 (1991).

[80] J. C. Philips, *Bonds and bands in semiconductors*, Academic, New York (1973).

[81] P. C. Kelires, *Short-range order, bulk moduli, and physical trends in c-$Si_{1-x}C_x$ alloys*, Phys. Rev. B **55**, 8784 (1997).

[82] D. R. Penn, *Wave-Number-Dependent Dielectric Function of Semiconductors*, Phys. Rev. **128**, 2093 (1962).

[83] C.W. Chen and J. Robertson, *Nature of disorder and localization in amorphous carbon*, J. Non-Cryst. Solids **227**, 602 (1998).

[84] F. Wooten, *Optical Properties of Solids*, Academic Press, New York, (1972).

[85] W.A. Harrison, *Elementary Electronic Structure*, p. 219, World Scientific, Singapore, (1999).

[86] J. Tauc, R. Grigorovici, A. Vancu, *Optical Properties and Electronic Structure of Amorphous Germanium*, Phys. Status Solidi **15**, 627 (1966).

[87] C. Godet, S. Kumar, V. Chu, *Field-enhanced electrical transport mechanisms in amorphous carbon films*, Philos. Mag. **83**, 3351 (2003).

[88] P. Patsalas, D. Papadimitriou, K. Kosmidis, P.C. Kelires, S. Logothetidis, and G. Evangelakis, unpublished.

[89] S. Waidmann, M. Knupfer, J. Fink, B. Kleinsorge, and J. Robertson, *Electronic structure studies of undoped and nitrogen-doped tetrahedral amorphous carbon using high-resolution electron energy-loss spectroscopy*, J. Appl. Phys. **89**, 3783 (2001).

[90] A.C. Ferrari and J. Robertson, *Interpretation of Raman spectra of disordered and amorphous carbon*, Phys. Rev. B **61**, 14095 (2000).

[91] Chhowalla, J. Robertson, C. W. Chen, S. R. P. Silva, C. A. Davis, G. A. J. Amaratunga, and W. I. Milne, *Influence of ion energy and substrate temperature on the optical and electronic properties of tetrahedral amorphous carbon (ta-C) films*, J. Appl. Phys. **81**, 139 (1997).

[92] G. Fanchini and A. Tagliaferro, *Disorder and Urbach energy in hydrogenated amorphous carbon: A phenomenological model*, Appl. Phys. Lett. **85**, 730 (2004).

[93] R.A. Street, *Hydrogenated Amorphous Silicon* Cambridge University Press, New York, (1991).

[94] J.D. Carey and S.R.P. Silva, *Disorder, clustering, and localization effects in amorphous carbon*, Phys. Rev. B **70**, 235417 (2004).

[95] C. Casiraghi, A.C. Ferrari, and J. Robertson, *Raman spectroscopy of hydrogenated amorphous carbons*, Phys. Rev. B **72**, 085401 (2005).

[96] Y.Lifshitz, Th. Kohler, Th. Frauenheim, I. Gouzman, A. Hoffman, R.Q. Zhang, X.T. Zhou, and S.T. Lee, *The mechanism of diamond nucleation from energetic species*, Science **297**, 1531 (2002).

[97] S. Welz, Y. Gogotsi, and M.J. McNallan, *Nucleation, growth, and graphitization of diamond nanocrystals during chlorination of carbides*, J. Appl. Phys. **93**, 4207 (2003).

[98] M.G. Fyta, I.N. Remediakis, P.C. Kelires, and D.A. Papaconstantopoulos, *Insights into the fracture mechanisms and strength of amorphous and nanocomposite carbon*, Phys. Rev. Lett. **96**, 185503 (2006).

[99] C. Mathioudakis, G. Kopidakis, P. C. Kelires, C. Z. Wang, and K. M. Ho, *Physical trends in amorphous carbon: A tight-binding molecular-dynamics study*, Phys. Rev. B **70**, 125202 (2004).

[100] C. Mathioudakis, G. Kopidakis, P. C. Kelires, P. Patsalas, M. Gioti, and S. Logothetidis, *Electronic and optical properties of a-C from tight-binding molecular dynamics simulations*, Thin Solid Films **482**, 151 (2005).

[101] C. Mathioudakis, G. Kopidakis, P. Patsalas, and P. C. Kelires, *Disorder and optical properties of amorphous carbon*, Diam. Relat. Mater. **XX**, XXX (2007).

[102] M. G. Fyta, C. Mathioudakis, G. Kopidakis, and P. C. Kelires, *Structure, stability, and stress properties of amorphous and nanostructured carbon films*, Thin Solid Films **482**, 56 (2005).